Aus dem Institut für Klinische Radiologie
der Ludwig-Maximilians-Universität München

Direktor: Prof. Dr. med. Dr. h.c. Maximilian F. Reiser, FACR, FRCR

QUANTIFICATION OF CEREBRAL HEMODYNAMICS WITH DYNAMIC CONTRAST-ENHANCED MRI

Dissertation
zum Erwerb des Doktorgrades der Naturwissenschaften
an der Medizinischen Fakultät
der Ludwig-Maximilians-Universität München

vorgelegt von
Michael Stefan Ingrisch
aus Neustadt a.d. Aisch

2011

Gedruckt mit Genehmigung der Medizinischen Fakultät
der Ludwig-Maximilians-Universität München

BETREUER

Priv.-Doz. Dr. rer. nat. Olaf Dietrich

ZWEITGUTACHTER

Priv.-Doz. Dr. Dr. Manfred Uhr

DEKAN:

Prof. Dr. med. Dr. h.c. Maximilian F. Reiser, FACR, FRCR

TAG DER MÜNDLICHEN PRÜFUNG:

24.10.2012

Meiner Familie.

PUBLICATIONS

During the course of this thesis, the following papers have been published:

Ingrisch M, Sourbron S, Morhard D, Ertl-Wagner B, Kümpfel T, Hohlfeld R, Reiser MF, Glaser C. Quantification of Perfusion and Permeability in Multiple Sclerosis: Dynamic Contrast-Enhanced MRI in 3D at 3T. *Invest Radiol*, accepted 10/06/2011

Cyran CC, Paprottka PM, Schwarz B, Sourbron S, **Ingrisch M**, von Einem JC, Pietsch H, Dietrich O, Hinkel R, Bruns CJ, Reiser MF, Wintersperger BJ, Nikolaou K. Dynamic Contrast-Enhanced (DCE-) MRI with Gadobutrol for Monitoring of Sorafenib Effect on Experimental Prostate Carcinomas with Immunohistochemical Correlations. *Am J Roentgenol*, accepted 07/07/2011

Cyran CC, Rist C, Paprottka PM, **Ingrisch M**, Clevert DA, Haug A, Reiser MF, Nikolaou K. Funktionelle und Molekulare Bildgebung – Aktueller Stand. *Wiener Klin Magazin*, 14(5):16-21, Oct 2011

Cyran CC, von Einem JC, Paprottka PM, Schwarz B, **Ingrisch M**, Dietrich O, Hinkel R, Bruns CJ, Clevert DA, Eschbach R, Reiser MF, Wintersperger BJ, Nikolaou K. Dynamic Contrast-Enhanced Computed Tomography Imaging Biomarkers Correlated With Immunohistochemistry for Monitoring the Effects of Sorafenib on Experimental Prostate Carcinomas. *Invest Radiol*, 47(1):49-57, Jan 2012

Paprottka PM, Zengel P, **Ingrisch M**, Cyran CC, Eichhorn M, Reiser MF, Nikolaou K, Clevert DA. Contrast-enhanced ultrasound in animal models. *Radiologe*, 51(6):506-513, Jun 2011.

Sommer WH, Sourbron S, Huppertz A, **Ingrisch M**, Reiser MF and Zech CJ. Contrast agents as a biological marker in magnetic resonance imaging of the liver: conventional and new approaches. *Abdom Imaging*, Apr 2011.

Biffar A, Sourbron S, Schmidt G, **Ingrisch M**, Dietrich O, Reiser MF and Baur-Melnyk A. Measurement of perfusion and permeability from dynamic contrast-enhanced MRI in normal and pathological vertebral bone marrow. *Magn Reson Med*, 64(1):115–124, Jul 2010.

Biffar A, Sourbron S, Dietrich O, Schmidt G, **Ingrisch M**, Reiser MF and Baur-Melnyk A. Combined diffusion-weighted and

dynamic contrast-enhanced imaging of patients with acute osteoporotic vertebral fractures. *Eur J Radiol*, Jun 2010.

Scherr MK, Seitz M, Müller-Lisse UG, **Ingrisch M**, Reiser MF and Müller-Lisse UL. MR-perfusion (MRP) and diffusion-weighted imaging (DWI) in prostate cancer: Quantitative and model-based gadobenate dimeglumine MRP parameters in detection of prostate cancer. *Eur J Radiol*, May 2010.

Dietrich O, Attenberger UI, **Ingrisch M**, Maxien D, Peller M, Nikolaou K and Reiser MF. Analysis of signal dynamics in oxygen-enhanced magnetic resonance imaging. *Invest Radiol*, 45(4):165–173, Apr 2010.

Ingrisch M, Dietrich O, Attenberger UI, Nikolaou K, Sourbron S, Reiser MF and Fink C. Quantitative pulmonary perfusion magnetic resonance imaging: influence of temporal resolution and signal-to-noise ratio. *Invest Radiol*, 45(1):7–14, Jan 2010.

Ingrisch M, Sourbron S, Reiser MF and Peller M. Model Selection in Dynamic Contrast Enhanced MRI: The Akaike Information Criterion. In R Magjarevic, O Dössel and WC Schlegel, editors, *World Congress on Medical Physics and Biomedical Engineering*, volume 25/4 of *IFMBE Proceedings*, pp. 356–358. Springer Berlin Heidelberg, 2010. ISBN 978-3-642-03882-2.

Attenberger UI[†], **Ingrisch M**[†], Dietrich O, Herrmann K, Nikolaou K, Reiser MF, Schönberg SO and Fink C. Time-resolved 3D pulmonary perfusion MRI: comparison of different k-space acquisition strategies at 1.5 and 3 T. *Invest Radiol*, 44(9):525–531, Sep 2009. [†]**UIA and MI contributed equally**

Attenberger UI, **Ingrisch M**, Büsing K, Reiser MF, Schoenberg SO and Fink C. Magnetic resonance imaging of pulmonary perfusion. Technical requirements and diagnostic impact. *Radiologe*, 49(8):739–747, Aug 2009.

Sourbron S, **Ingrisch M**, Siefert A, Reiser M and Herrmann K. Quantification of cerebral blood flow, cerebral blood volume, and blood-brain-barrier leakage with DCE-MRI. *Magn Reson Med*, 62(1):205–217, Jul 2009.

Dietrich O, Raya JG, Reeder SB, **Ingrisch M**, Reiser MF and Schoenberg SO. Influence of multichannel combination, parallel imaging and other reconstruction techniques on MRI noise characteristics. *Magn Reson Imaging*, 26(6):754–762, Jul 2008.

CONTENTS

LIST OF FIGURES

LIST OF TABLES

Part I

INTRODUCTION AND OVERVIEW

1 INTRODUCTION

Magnetic resonance imaging (MRI) is a non-invasive imaging modality with growing importance in the field of diagnostic radiology. MRI employs the effect of nuclear magnetic resonance to measure the distribution of nuclei with a non-vanishing spin in the body. An advantage of MRI is that, unlike other imaging methods such as computed tomography (CT) or positron-emission tomography (PET), MRI does not expose the patient to ionizing radiation. Moreover, MRI provides a wide range of different soft-tissue contrasts, with the possibility of fine-tuning image contrast by manipulating a variety of acquisition parameters. MRI also offers the possibility of imaging beyond morphology and allows insights into various aspects of tissue function, such as diffusion of water molecules in the body or the perfusion of tissue and organs.

Perfusion is defined as the delivery of arterial blood to the capillary bed. As such, perfusion is responsible for maintaining the metabolism by supplying tissue and cells with nutrients and removing metabolic waste products. Perfusion or blood flow[1] is thereby one of a variety of parameters that describe and characterize the hemodynamic state of the microvasculature. Other parameters include the relative blood volume, i. e. the fraction of space that is occupied by blood vessels, the mean transit time or the permeability of the vessel walls.

The assessment of the hemodynamic state of brain tissue is of interest in a range of pathologies such as stroke, brain tumors or inflammatory diseases such as multiple sclerosis. An important class of methods for this purpose is formed by *bolus-tracking* measurements. Here, a contrast agent is injected rapidly in a vein, carried through the vasculature by circulation and eventually arrives at the tissue of interest. If the concentration of contrast agent is measured with an appropriate means in a time-resolved manner in the tissue and in arterial blood, a range of hemodynamic parameters can be derived from the form and relation of these two curves using the theory of tracer kinetics.

Bolus-tracking perfusion measurements using MRI date back to the late 1980's [1] – since then, qualitative and, increasingly, quantitative perfusion measurements have been carried out in virtually all body organs, e.g. the lungs [2–4], the kidneys [5], the prostate [6–8], the heart [9] and the liver [10]. In most organs

1 Since perfusion is largely dominated by the flow of arterial blood, the terms *perfusion* and *blood flow* are often used interchangeably in MRI literature.

apart from the brain, the preferred method for dynamic MRI measurements uses a T_1-weighted acquisition, which detects the changes in the longitudinal relaxation time T_1 that are induced by presence of the contrast agent. The contrast agent shortens the T_1 time of water protons, which leads to an increase of signal intensity in T_1-weighted acquisitions. Hence, this approach is commonly referred to as *dynamic contrast-enhanced* (DCE) MRI.

Due to the special physiology of brain tissue, however, the predominant approach for dynamic MRI measurements is a different one. Brain tissue is characterized by a low blood volume (CBV, cerebral blood volume) in the range of 2-4%, and by a distinct feature that is absent in other organs, the *blood-brain barrier* (BBB). The BBB restricts the passage of a wide range of substances, including most contrast agents, from the intravascular into the extravascular space and vice versa. Thus, the total amount of contrast agent in healthy brain tissue is small, leading to only small signal changes and a low contrast-to-noise ratio in T_1-weighted acquisitions. Since a contrast agent that is confined to the intravascular space leads to strong T_2^* effects [11, 12], the common approach for dynamic MRI in the brain uses a T_2- or T_2^*-weighted acquisition and is referred to as *dynamic susceptibility-weighted contrast* (DSC) MRI.

For the purpose of quantification, however, DSC MRI poses several difficulties that are not present when DCE MRI is used: The T_2^* relaxivity of contrast agent depends on the micro- and mesoscopic structure of the tissue and, in particular, is different between blood and tissue [13]. The ratio of these two relaxivities enters directly into the quantification as a scaling error. An additional problem arises when the BBB is disturbed and the contrast agent can leak into the interstitial volume. Extravasation of the contrast agent decreases the compartmentalization of the tracer and thereby reduces the T_2^* relaxation of the tracer. Furthermore, the tracer accumulates in the interstitial space, leading to a shortening of the T_1 relaxation time. These two effects mimic the loss of tracer and thereby complicate the quantification of perfusion parameters. Although a range of correction algorithms has been proposed (e. g. [14–17]), the quantification of the tracer concentration in presence of BBB leakage still remains an issue in DSC MRI [18].

Since these effects play a less significant role if a T_1-weighted acquisition is used, the aim of this thesis is to investigate the feasibility of DCE MRI for the quantification of cerebral hemodynamics, both in healthy brain tissue and in pathological situations with BBB leakage. For this purpose, this thesis is organized as follows:

Chapter 2 is a brief overview of basic anatomy and the physiology of the brain. The purpose of this chapter is to provide a

physicist with those aspects of physiology that are necessary for an understanding of tracer kinetic modeling.

Chapter 3 provides a high-level overview of the fundamentals of magnetic resonance imaging, Ch. 4 discusses the time-resolved measurement of contrast agent concentrations by means of DCE MRI in more detail. For the purpose of deriving concentrations from the measured signal intensities, a brief overview of MR signal analysis is given, and several aspects of the DCE MRI acquisition are discussed.

Several techniques to derive various quantitative hemodynamic parameters from measured time-resolved tracer concentrations by means of tracer-kinetic theory are described in Ch. 5. In particular, a set of two-compartment models is introduced; with these models, most hemodynamic situations that occur in tissue can be described mathematically.

After these introductory chapters, Chs. 6 – 8 present the original research that constitutes this thesis. Ch. 6 presents methodological improvements that were developed during the course of this thesis. In particular, this chapter comprises a simulation study that investigates a method for automatic model selection with the aim of further refining quantification using a set of several tracer kinetic models. These developments were used in the two patients studies that constitute the two following chapters. In an initial study, presented in Ch. 7, the feasibility of quantification of cerebral hemodynamics with a 2D DCE MRI sequence in patients with brain tumors is investigated, and limitations are identified, in particular the insufficient spatial coverage of the 2D acquisition and the need for higher contrast-to-noise ratio.

Finally, Ch. 8 presents a study which was conducted in a collective of patients with multiple sclerosis (MS); the aim of this study was the quantitative assessment of cerebral hemodynamics both in normal-appearing white matter and in MS lesions. The limitations that were identified in the previous study were addressed with a dynamic 3D acquisition to achieve complete spatial coverage of the brain and an optimized post-processing approach, based on the results of the model selection study in Ch. 6.

2

CEREBRAL HEMODYNAMICS: ANATOMY AND PHYSIOLOGY

The objective of this chapter is to introduce those aspects of anatomy and physiology that are necessary for an understanding of tracer kinetic modeling, which is a central part of this thesis.

2.1 ANATOMY AND PHYSIOLOGY OF THE BRAIN

2.1.1 *Macrostructure*

The brain can be divided into four different sections: the *cerebrum*, the *cerebellum*, the *diencephalon* and the *brainstem*, the spatial relation of these sections is shown in Fig. 1.

CEREBRUM The cerebrum forms the most notable part of the human brain. It is composed of two symmetric hemispheres which are connected by a bundle of nerve fibers, the *corpus callosum*. The surface of the hemispheres has a convoluted surface, the convolutions (*gyri*, singular *gyrus*) are separated by shallow grooves called *sulci* (singular *sulcus*) and deep grooves called *fissures*. These fissures allow to subdivide each hemisphere into five smaller structures called *lobes* (cf. Fig. 2): the frontal lobe, the parietal lobe, the temporal lobe, the occipital lobe and, hidden from the surface, the insula. Through these convolutions, the outer surface of the hemispheres is greatly enlarged.

Cross-sections of the brain (Fig. 3) show a clear distinction of the surface layer, the *cerebral cortex*, and the underlying *white matter*. The cerebral cortex has a thickness of several millimeters and is composed mainly of *gray matter* (see below). It is responsible for receiving and processing stimuli from the senses, for the voluntary control of skeletal muscles, and for conscious activities. In general, each hemisphere is responsible for the interaction with the contralateral side of the body.

Beneath the cerebral cortex is the cerebral white matter, composed mainly of myelinated axons that form connections between different parts of the brain, e. g. between different regions within the same hemisphere (*association fibers*) or between hemispheres (*commissural fibers*). The corpus callosum is composed mainly of commissural fibers, connecting the two hemispheres.

DIENCEPHALON AND BRAINSTEM The diencephalon forms the connection of the cerebrum to the brain stem and includes

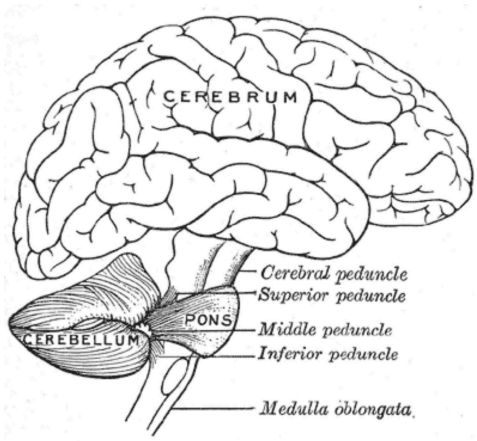

Figure 1: The spatial relation between cerebrum, cerebellum and brain stem (from *Gray's anatomy[19]*)

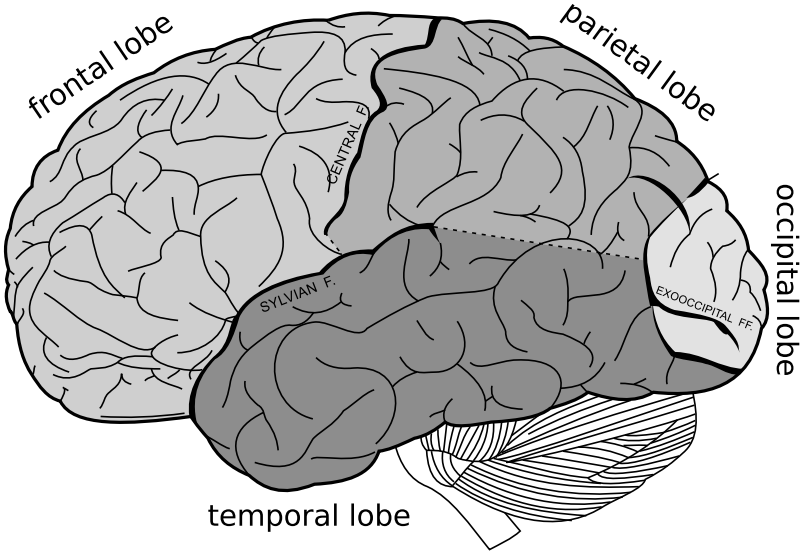

Figure 2: Lobes of the cerebral cortex (from *Gray's anatomy*)

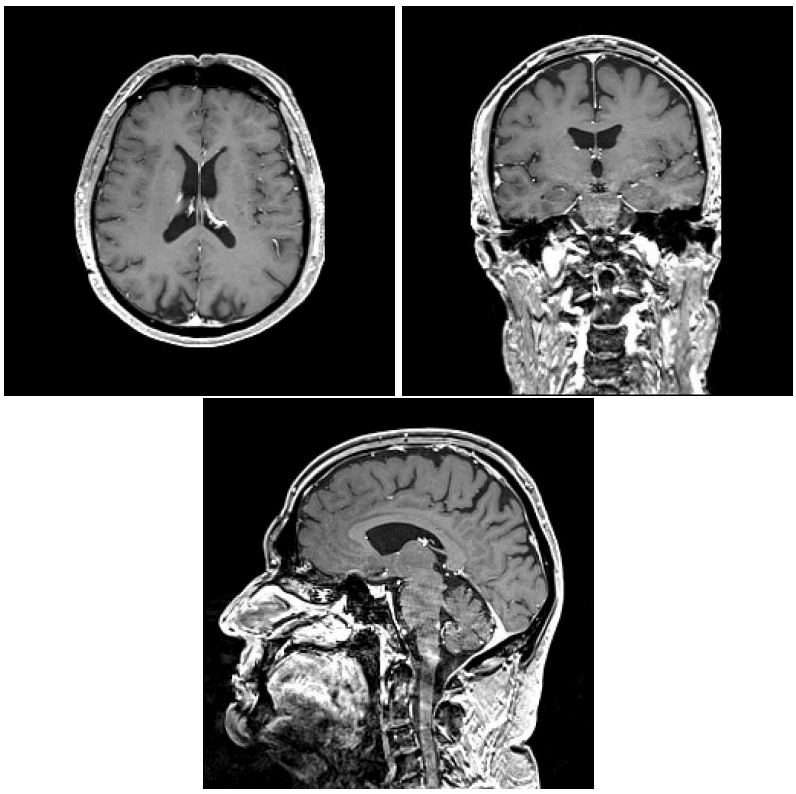

Figure 3: Axial, coronal and sagittal sections of the brain, obtained with a T_1-weighted MRI sequence.

important structures like the thalamus, the hypothalamus and the pineal gland. The thalamus acts as a relay that forwards sensory signals to the corresponding cortical areas. Moreover, it has an important function in the regulation of sleep and wakefulness. The hypothalamus provides the link between the central nervous system and the endocrine system; for this purpose, it does not have a blood-brain barrier like other parts of the brain. It is also the responsibility of the hypothalamus to control a range of functions of the autonomic nervous system, thus regulating hunger, thirst, sleep and fatigue, as well as body temperature.

The brainstem forms the connection of both the cerebellum and the cerebrum with the spinal cord. Thus, its main role is to relay information from the body to the cerebellum and cerebrum, and vice versa. It is composed of the midbrain, providing the link to the diencephalon, the *pons*, a bulging structure that links to the cerebellum, and the *medulla oblongata*, which forms the connection to the spinal cord.

CEREBELLUM The cerebellum is a separate structure of the brain, it is located below the cerebrum and behind the *pons*, a part of the brainstem (Fig. 1). It is composed of three parts: two cerebellar hemispheres and a central region called *vermis*. The cerebellum is separated from the cerebrum via a layer of *dura mater*, all its functional connections to the rest of the brain are routed through the pons. The cerebellum is mainly responsible for the fine control of movement and contributes to precision, coordination and timing by comparing and correcting actual, performed movement with the intended movement.

2.1.2 *Microstructure*

The tissue of the central nervous system (CNS) contains nerve cells called neurons, glial cells and capillaries. Neurons form a neural network, for this purpose, they have two kinds of processes, dendrites and axons. Axons transmit information by the conduction of electrical impulses and are connected to other neurons via synapses. For this purpose, they are ensheathed with a fatty substance called myelin that provides electrical insulation and facilitates saltatory conduction of action potentials.

Glial cells are generally considered to play a supportive role in the central nervous system and include microglia, oligodendrocytes and astrocytes. Microglia are the macrophages of the CNS and form the main form of immune defense in the CNS. Oligodendrocytes are responsible for producing the myelin sheath around the axons, consequently, damage to the oligodendrocytes results in demyelination of axons. Astrocytes are the most numerous of the glial cells, they play a role in the formation and maintenance

of the blood-brain barrier and are thought to influence blood flow by regulating vasodilation.

In the brain, zones of white and gray matter can easily be distinguished. Gray matter is found mainly in the cerebral cortex, in the cerebellum and in the basal ganglia. It is composed mainly of neurons, unmyelinated axons, glial cells and capillaries. Due to the high metabolic demand of neurons, both blood flow and blood volume are higher in gray matter than in white matter. White matter, on the other hand, is found underneath the gray matter in the cerebral cortex. In contrast to gray matter, it consists mainly of myelinated axons that connect different areas of gray matter; moreover, it contains glial cells and capillaries, the latter to a lesser extent than gray matter. The most prominent white matter structure is the corpus callosum which connects the two cerebral hemispheres, but white matter is also found in the brain stem and in the spinal cord. The main purpose of white matter is to pass messages between different areas of gray matter within the brain.

2.1.3 *Cerebral vascular system*

Blood supply of the brain is accomplished by a range of cerebral arteries; essentially, each hemisphere is supplied by

- the *anterior cerebral artery* (ACA),
- the *middle cerebral artery* (MCA) and
- the *posterior cerebral artery* (PCA).

The anterior and middle cerebral arteries are branches of the respective *internal carotid artery* (ICA), the two posterior cerebral arteries are branches of the *basilar artery*, which in turn is formed by the two joined *vertebral arteries*.

The six cerebral arteries are joined at the base of the brain by a ring of anastomosis termed the *circle of Willis* (see Fig. 4). In the circle of Willis, the two anterior cerebral arteries are connected by the *anterior communicating artery*, the two MCAs are connected to the posterior cerebral arteries via the *posterior communicating artery*.

The terminal branches of the cerebral arteries form the *cortical arterial system*, from here, arteries and arterioles enter the brain perpendicularly; the long or medullary arteries pass through the gray matter and penetrate the white matter, the short vessels supply the cortical gray matter.

CEREBRAL VEINS Blood is drained from the brain by the cerebral veins, which empty into large channels, the *sinuses* (see Fig. 5). The sinuses have a large diameter, compared to the arteries,

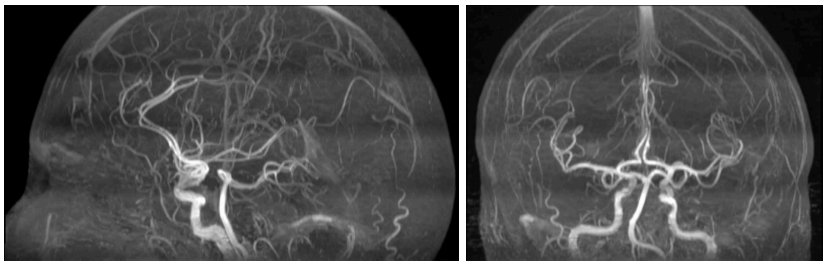

(a) sagittal and coronal MIP

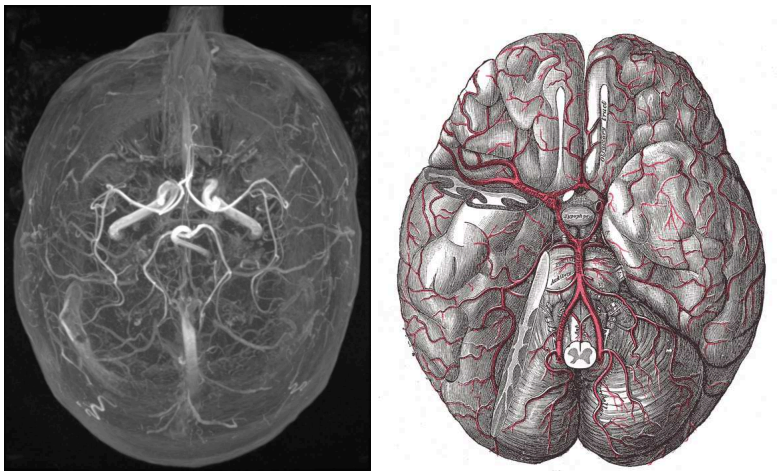

(b) axial MIP and illustration

Figure 4: Main arteries of the brain. Top row: Sagittal and coronal maximum intensity projections (MIP) from a 3D time-of-flight angiography, bottom row: transverse MIP from the same dataset and a corresponding illustration from *Gray's anatomy*

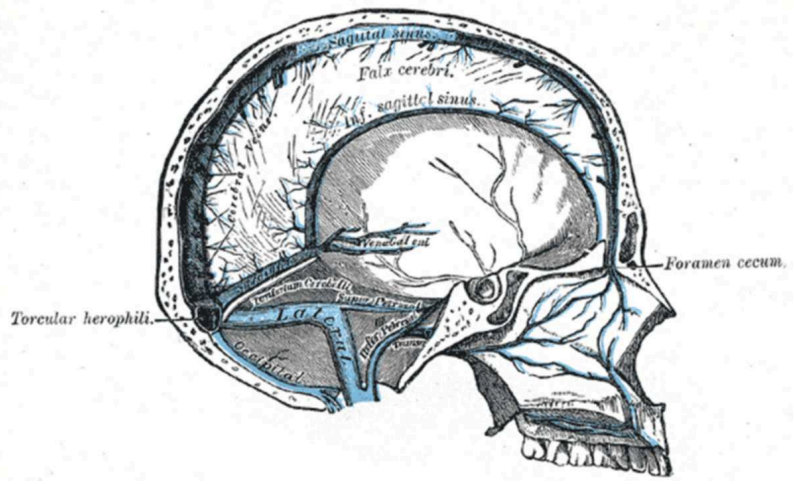

Figure 5: The sinuses that drain blood from the brain into the jugular veins

and do not possess any valves. The superior sagittal sinus is probably the most prominent of these vessels, it runs from anterior to posterior, increasing its diameter and is continued by one of the transverse sinuses. The other transverse sinus forms the continuation of the straight sinus, both transverse sinuses run to the base of the skull and are continued as the jugular veins.

2.1.4 *Cerebral microcirculation and the blood-brain barrier*

The term *microcirculation* describes the flow of blood through the smallest of vessels, arterioles, metarterioles, capillaries and venules. The primary function of the microcirculation is to facilitate the exchange of a wide range of substances between blood and tissue. Important prerequisites for such an exchange to take place are long contact times of the blood and the capillary wall and a large surface area of the capillary wall. These prerequisites are fulfilled by the structure of the microcirculation, depicted in Fig. 6.

Capillaries are the smallest of blood vessels and connect the arterial side of the microcirculation, i. e. the arterioles, with the venous, blood collecting side of the microcirculation, represented by venules. The diameter of capillaries is in the range from 5 to 10 μm, consequently, erythrocytes (sized approximately 6 to 8 μm need to travel through them in single file and need to deform themselves, thereby increasing their contact surface. Blood flow through the capillaries is controlled by small, muscular rings called *precapillary sphincters* at the arterial end of the capillary. Depending on the tissue type, a variable amount of capillaries is closed at any given time point. If the metabolic demand of the

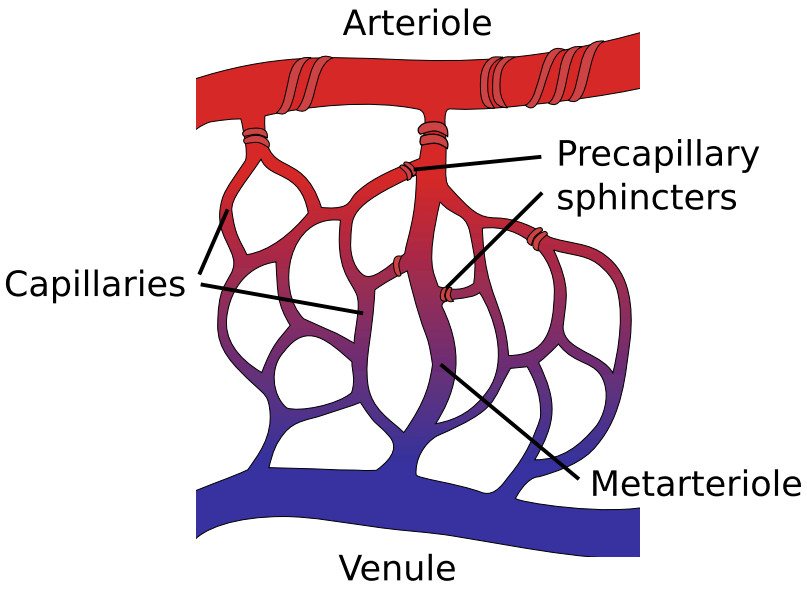

Figure 6: Structure of the microcirculation: Blood is delivered to the microcirculation via the arterioles. Precapillary sphincters at the arterial end of the capillaries control and regulate the amount of blood that is delivered to the capillaries; after passage through the capillary bed, the now venous blood is collected by venules.

tissue rises, more capillaries are opened and the relative blood volume and blood flow through the tissue increase.

THE CAPILLARY WALL The capillary wall is composed of an unicellular layer of endothelial cells with a total thickness of approximately 0.5–1 µm (see Fig. 7), surrounded by a *basement membrane*. The endothelial cells are connected via *tight junctions*, gaps between adjacent cells that are not connected form the *intercellular clefts*. In peripheral capillaries, *fenestrations*, pores in the endothelial cells, allow the passage of small molecules and some proteins across the capillary wall.

There are three important pathways for the transport of particles through the capillary wall [20]:

- Lipid-soluble substances can pass the capillary wall by transcellular diffusion across the cell membranes, due to the large surface of the cell membranes, the transport rate of these substances is limited only by the blood flow through the capillary.
- Small hydrophilic molecules such as water, sugars and amino acids, are relatively free to cross the capillary wall by

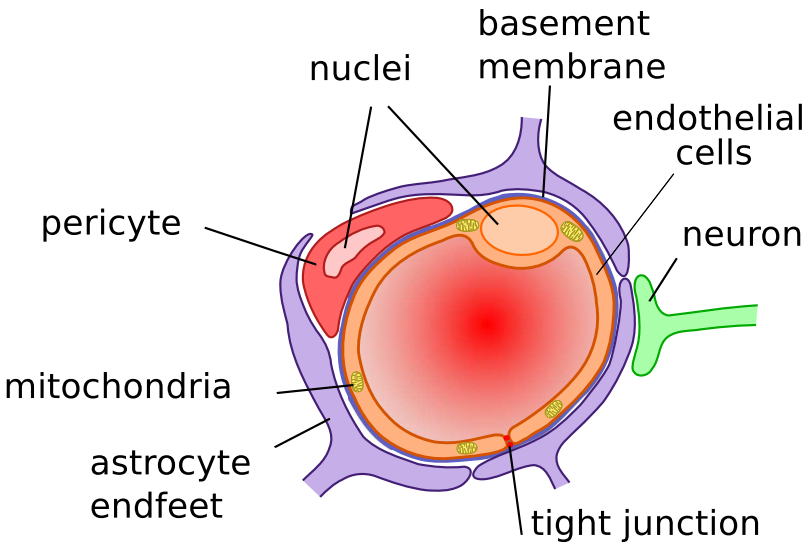

Figure 7: Structure of the capillary wall of cerebral capillaries. In contrast to peripheral capillaries, cerebral capillaries have no intercellular clefts, and endothelial cells are connected with tight junctions. Endothelial cells of cerebral capillaries are covered by the endfeet of astrocytes.

passing through gaps between the endothelial cells called *intercellular clefts*, and through the fenestrations.

- Larger molecules such as most proteins cannot pass through the gaps between endothelial cells and thus rely on active transport across the cell membrane. Depending on the size and the lipid solubility of the substance, a range of mechanisms exists to facilitate transport across the cell membranes; these mechanisms in general require the expenditure of energy.

The flow of fluid across the capillary wall is controlled by a delicate balance between the hydrostatic intravascular pressure and the osmotic pressure arising through differences in the concentration of soluted salts and plasma proteins between blood plasma and interstitial fluid. As blood enters a capillary from an arteriole, the hydrostatic pressure in the capillary exceeds the osmotic pressure, resulting in a net flow from the vessel into the interstitium. In the middle of the capillary, the hydrostatic and osmotic pressures are equal, leading to a zero net flow; the main exchange of substances takes place in this zone of the capillary. On the venous end of the capillary, the blood pressure falls below the osmotic pressure, so that excess fluid is removed from the interstitium.

THE BLOOD-BRAIN BARRIER In contrast to peripheral capillaries, capillaries in the brain have no fenestrations and no

intercellular clefts; the endothelial cells are connected with *tight junctions*, so that the passage of soluted substances across the capillary wall is effectively inhibited. Cerebral capillaries are surrounded and covered by the end-feet of astrocytes (see Fig. 7), providing physical support of the capillaries; astrocytes are also assumed to play a role in the formation of the tight junctions.

Small and lipid-soluble substances such as oxygen, carbon dioxide, small alcohols and also anaesthetics can pass the capillary wall by diffusion through the endothelial cells; due to the special structure of the cerebral capillary walls, the permeability for electrolytes and and larger molecules such as plasma proteins is orders of magnitude smaller. This strict separation of intravascular and interstitial space forms the *blood-brain barrier* (BBB).

It is the purpose of the blood-brain barrier to protect the sensible brain tissue from potentially harmful substances, as well as to restrict access of viruses and bacteria. The blood-brain barrier is essential to maintain brain homeostasis and to insulate the brain from the endocrine system. Moreover, the BBB restricts the passage of neurotransmitters into the circulation.

2.2 PATHOLOGIC CONDITIONS

The hemodynamic status of brain parenchyma is altered or disturbed in a range of pathologies and diseases. Probably the most notably disturbance is BBB leakage, which is easily demonstrated as hyperintense areas on contrast-enhanced T_1-weighted images. BBB leakage can occur as a consequence of inflammation, as a result of radiation, in areas of necrosis and in primary or secondary brain tumors. Changes in blood flow and blood volume are more difficult to demonstrate and usually require a dynamic measurement. The most prominent example is stroke, where the occlusion of an artery results in decreased blood flow in the area that is supplied by that artery.

2.2.1 *Multiple sclerosis*

Multiple sclerosis (MS) is a chronic, inflammatory, immune-mediated demyelinating disease of the central nervous system. During the disease, the myelin ensheathing the axons is destroyed in focal areas, which results in multiple sclerotic lesions [21]. These lesions are a characteristic feature of MS; the location of these lesions determines the symptoms and neurological deficits that occur during the course of the disease. Consequently, a wide range of symptoms can occur in MS, including cognitive impairment, bladder and bowel dysfunctions, optic neuritis, speech

impairment, and fatigue. Depending on the further evolution of such a lesion, the neurological deficits may revert or persist.

For the definitive diagnosis of MS, according to the McDonald criteria [22, 23], it is necessary to demonstrate both dissemination in space and in time. Dissemination in space and time means here that individuals must have a minimum of two attacks and these attacks must affect two different sites. In the revised criteria, the second attack need not have a clinical manifestation, but can e. g. be confirmed by a new lesion visible in MRI.

LESION EVOLUTION Immune engagement is considered to be an early step in the formation of a new lesion [21]. Autoreactive lymphocytes cross the BBB and initiate an inflammatory response. This inflammmatory response sustains the initial breakdown of the BBB, and leads to increased blood flow and blood volume. The resulting BBB leakage can readily be demonstrated by contrast agent extravasation in MRI. Oligodendrocytes, the cells that are responsible for creating and maintaining the myelin sheath around the axons, are attacked and destroyed, resulting in a loss of the myelin sheath around the axons. Since myelin occurs mainly in white matter, MS lesions concentrate in white matter in the brain as well as in the spinal cord. After recovery from the acute inflammatory phase, the axons may become remyelinated, or the demyelination and the corresponding neurologic deficits may persist.

MRI IN MS MRI has become an important tool in the diagnosis and in the clinical workup of MS. Dissemination in space and time, which is required for the diagnosis of MS, can be demonstrated with MRI even if the patient has only a clinically isolated syndrome suggestive of MS [24]. Most MS lesions appear as hyperintense areas on T_2-weighted or fluid-attenuated inversion recovery (FLAIR) images. This hyperintensity can be caused by different processes during lesion evolution, so that the specificity is low. Active lesions in an acute inflammatory phase can be distinguished from inactive lesions by uptake of contrast agent, leading to hyperintensity of T_1-weighted imaging. Moreover, T_1-weighted imaging allows for the detection of "black holes", lesions that are associated with severe tissue damage and appear hypointense both on pre- and postcontrast images. For detailed overview about MR imaging in MS, the reader is referred e. g. to [24–26].

2.2.2 *Tumors and angiogenesis*

Brain tumors can be classified as primary brain tumors, originating from brain tissue, or secondary brain tumors, that originate

from other organs and have metastasized into the central nervous system. Both types of tumors can produce similar symptoms by invasion of the brain, by compression of structures and by increase of the intracranial pressure. The clinical symptoms are determined by the area of the brain that is affected by the tumor.

A critical step in the evolution of a tumor is the onset of angiogenesis. In its initial stage, which is also called *dormant stage*, any tumor is supplied by diffusion, which is limited to short distances. Consequently, any tumor that does not have a vascular supply is limited to a sub-millimeter size, determined by the distance over which sufficient amounts of oxygen and nutrients can diffuse. To grow beyond this size, the tumor needs some form of angiogenesis to form new blood blood vessels, which allow supply with nutrients and removal of metabolic waste by convective flow.

Angiogenesis is a common process during growth, but also in wound healing and in the female reproductive cycle. The start of angiogenesis, however, forms also a critical step in the development of a tumor, since only a vascular supply allows a tumor to grow beyond microscopic size.

The process of vessel formation can be accomplished with different mechanisms. *Sprouting angiogenesis* occurs in well characterized stages [27]. In an early stage, angiogenic growth promoting factors such as VEGF (*vascular endothelial growth factor*) are released by inflammatory, hypoxic or tumor cells. These factors initiate detachment of pericytes that cover the vessel wall, increase the permeability of the endothelial cell layer, and activated endothelial cells release enzymes that degrade the basement membrane. In this stage, plasma proteins can extravasate from the vessel and build an extracellular matrix. Endothelial cells then proliferate into this matrix and form *sprouts*. These sprouts extend towards the source of the angiogenic stimulus and ultimately fuse with other vessels to initiate blood flow. Eventually, the newly formed vessel becomes mature and stable, however, in a tumor, this rarely occurs, resulting in a malformed vessel network. Other types of vessel formation such as *intussusceptive angiogenesis* have been described, but the relevance of these processes for tumor angiogenesis is less understood [27].

The morphology and function of pathologic tumor vessels that result from dysregulated angiogenesis differs from that of normal vessels in a range of points [28]. Tumor vessels are leaky as a result of large gaps between endothelial cells and an abnormal basement membrane due to high levels of vascular endothelial growth factor expressed by tumor cells. Moreover, tumor vessels are not organized in a hierarchical and successively branching fashion like normal vascular networks, but instead are disorganized with varying and large vessel lumen diameter, resulting in

non-uniform and chaotic blood flow. The interstitial pressure in the tumor is high, partly due to the lack of a functional lymphatic system, so that not all areas of the tumor are supplied by blood, resulting in areas that are hypoxic and also not accessible to blood-borne drugs.

3 FUNDAMENTALS OF MR IMAGING

Magnetic resonance imaging *(MRI)* employs the effect of nuclear magnetic resonance for the purpose of spatially resolving the distribution and relaxation properties of hydrogen atoms (or other atomic nuclei with non-vanishing nuclear spins). This chapter can only provide a high-level overview about the fundamentals of magnetic resonance, for a detailed review, the reader is referred to standard textbooks about magnetic resonance imaging [29, 30].

3.1 NUCLEAR SPIN AND MACROSCOPIC MAGNETIZATION

The atomic nucleus is composed from protons and neutrons and is characterized by the *atomic number* Z, describing the number of protons, the *mass number* A, which describes the total number of protons and neutrons in the nucleus, and the *nuclear spin quantum number* I. I may be zero, half-integer or integer. Generally, isotopes with even mass numbers have integer spin and isotopes with odd mass numbers have half-integer spin. The simplest example is the hydrogen nucleus ^1H, consisting of a single proton with $I = 1/2$. For isotopes with even mass numbers, two more rules apply [30]:

- If both the numbers of protons and neutrons are even, the nuclear spin is $I = 0$, an example is ^{12}C with 6 protons and 6 neutrons.
- If both the numbers of protons and neutrons are odd, the nuclear spin is integer and larger than zero, for example the spin of deuterium ^2H is $I = 1$.

If I is non-zero, the magnetic moment $\boldsymbol{\mu}$ of the nucleus is connected to the nuclear spin $\boldsymbol{I}$ via

$$\boldsymbol{\mu} = \gamma \boldsymbol{I} \tag{3.1}$$

Here, γ is the *gyromagnetic ratio*, which is a characteristic constant for the nucleus. For the hydrogen nucleus, γ has the value $2.675 \times 10^8\,\mathrm{rad\,T^{-1}\,s^{-1}}$.

SPINS IN AN EXTERNAL MAGNETIC FIELD The behavior of an atomic nucleus with non-zero spin and magnetic moment $\boldsymbol{\mu}$ in an external magnetic field $\boldsymbol{B}$ can be described classically by

$$\frac{d\boldsymbol{\mu}}{dt} = \gamma \boldsymbol{\mu} \times \boldsymbol{B} \tag{3.2}$$

This is the classical equation for the magnetic dipole and implies, that a given magnetic moment will precess around the vector of the magnetic field with the field strength B with the *Larmor frequency* $\omega_0 = \gamma B$.

In the absence of an external field, a collection of a large number of spins, such as the ^1H nuclei in a sample of water, has a vanishing net magnetization, since the individual magnetic moments point in all possible orientations in space and are distributed uniformly. If the sample is brought into a static magnetic field (or, equivalently, an external magnetic field is switched on), a non-vanishing net magnetization will develop, since the distribution of the individual magnetic moments will be skewed by the direction of the magnetic field.

This effect can be described classically (see e. g. [31]), since the angular distribution of the magnetic moments obeys Boltzmann statistics:

$$P(\theta) = \frac{\exp(-E(\theta)/kT)}{\int_0^\pi exp(-E(\theta)/kT)\sin\theta d\theta} \tag{3.3}$$

with the energy $E(\theta) = -\mu B\cos\theta$ that depends on the angle θ between the magnetic moment $\boldsymbol{\mu}$ and the magnetic field $\boldsymbol{B}$.

With this distribution, the equilibrium magnetization of the sample in water can be calculated [31] as

$$\begin{aligned} M_z &= \int_0^\pi P(\theta)(\mu\cos\theta)\sin\theta d\theta \\ &\approx \frac{\hbar^2\gamma^2 B_0}{4kT}. \end{aligned} \tag{3.4}$$

This approximation is valid for small degrees of polarization, which occur if thermal energies are not too low ($kT > \gamma\hbar B_0$). In this limit, the classical description yields the same result as the quantum-mechanical description. In a setting typical for MRI, i. e. a magnetic field of 1.5 T and room temperature, the polarization is in the order of 10^{-6}. This illustrates that high magnetic fields are required to produce a measurable magnetization in a water sample.

Just as in the case of a single spin in an magnetic field, the temporal evolution of the macroscopic magnetization $\boldsymbol{M}(t)$ of a collection of spins in an arbitrary magnetic field $\boldsymbol{B}(t)$ is described by the differential equation

$$\frac{d\boldsymbol{M}(t)}{dt} = \gamma\boldsymbol{M}(t)\times\boldsymbol{B(t)}. \tag{3.5}$$

In particular, the transverse component of the magnetization will precess with the Larmor frequency ω_0 around the direction of

the magnetic field. This precession produces a radiofrequency field, this field is the quantity that is measured in MRI.

3.2 RADIOFREQUENCY EXCITATION

The angle between the macroscopic magnetization $\boldsymbol{M}$ and the magnetic field $\boldsymbol{B_0} = B_0 \cdot \boldsymbol{e_z}$ can be modified by irradiation with a radiofrequency (RF) pulse $\boldsymbol{B}_1(t)$. If $\boldsymbol{B}_1(t)$ rotates around $\hat{\boldsymbol{e}}_z$ with the frequency ω_1

$$\boldsymbol{B_1}(t) = B_1 \cdot (\hat{\boldsymbol{e}}_x \cos(\omega_1 t) + \hat{\boldsymbol{e}}_y \sin(\omega_1 t)), \tag{3.6}$$

the temporal evolution of the magnetization can be written as

$$\begin{aligned} \frac{d\boldsymbol{M}(t)}{dt} &= \gamma \cdot \boldsymbol{M}(t) \times (\boldsymbol{B_0} + \boldsymbol{B_1}(t)) \\ &= \gamma \cdot \boldsymbol{M}(t) \times (B_1 \cos(\omega_1 t)\hat{\boldsymbol{e}}_x + B_1 \sin(\omega_1 t)\hat{\boldsymbol{e}}_y + B_0 \hat{\boldsymbol{e}}_z). \end{aligned} \tag{3.7}$$

After transformation from the laboratory system (x, y, z) into a coordinate system that rotates around $\hat{\boldsymbol{e}}_z$ with the frequency ω_1 ($x' = x\cos(\omega_1 t) + y\sin(\omega_1 t), y' = -x\sin(\omega_1 t) + y\cos(\omega_1 t), z' = z$), Eq. (3.7) simplifies to

$$\frac{d\boldsymbol{M}(t)}{dt} = \gamma \cdot \boldsymbol{M}(t) \times (B_1 \hat{\boldsymbol{e}}_x + (B_0 - \frac{\omega_1}{\gamma})\hat{\boldsymbol{e}}_z). \tag{3.8}$$

Eq. (3.8) describes a precession of the macroscopic magnetization around the effective magnetic field $\boldsymbol{B}_{\text{eff}} = B_1 \hat{\boldsymbol{e}}_x + (B_0 - \frac{\omega_1}{\gamma})\hat{\boldsymbol{e}}_z$ with a frequency of $\omega_{\text{eff}} = \gamma B_{\text{eff}}$. If the frequency ω_1 of the RF pulse equals the Larmor frequency ω_0, the z-component of the effective field vanishes and $\boldsymbol{M}$ precesses around the x'-axis alone. If such a RF pulse is irradiated over a time interval Δt, the magnetization $\boldsymbol{M}$ is *flipped* from the z-axis by the *flip angle*

$$\alpha = \gamma B_1 \Delta t \tag{3.9}$$

Hence, the magnitude of the flip angle can be adjusted either by the duration Δt or the amplitude B_1 of the RF pulse. After the RF pulse is switched off, the transverse magnetization $M_{\text{trans}} = M \sin\alpha$ that was created by flipping the magnetization away from the z-axis precesses around the z-axis with the Larmor frequency ω_0.

3.3 RELAXATION AND BLOCH EQUATIONS

After the magnetization $\boldsymbol{M}$ has been flipped by a RF pulse, several relaxation processes occur that eventually restore the equilibrium magnetization $\boldsymbol{M_0} = M_0 \hat{\boldsymbol{e}}_z$.

The *longitudinal* or *spin-lattice* relaxation time T_1 characterizes the exponential restoration of the longitudinal component M_z of the magnetization, the reason for this relaxation is spin-lattice interaction. Consequently, the energy that is released by relaxation of the longitudinal magnetization is absorbed by the lattice.

On the other hand, the coherent transverse magnetization that exists immediately after a RF excitation pulse decays by a loss of phase coherence between the different spins. Every spin is exposed to fluctuating field which vary the z-component of the magnetic field and hence the precession frequency and the phase. This decay of the transverse relaxation is characterized by the *spin-spin* relaxation time T_2.

Generally, the decay of the transverse relaxation is faster as the T_2-relaxation alone can explain. This is due to magnetic field inhomogeneities and changes in susceptibility that result in additional variations in the phase of the spins, this component of the transverse relaxation is characterized by a time constant T_2'. In contrast to the T_2-relaxation, the T_2'-relaxation can be reversed by inverting the phase. The entire decay of the transverse magnetization is described by a time constant T_2^*:

$$\frac{1}{T_2^*} = \frac{1}{T_2} + \frac{1}{T_2'} \tag{3.10}$$

In general, the relaxation times T_1, T_2 and T_2^* vary e. g. between different types of tissue, but depend also on the magnetic field B_0.

Empirically, the relaxation processes can be described by the *Bloch equations*:

$$\begin{aligned} \frac{dM_x}{dt} &= \gamma(\boldsymbol{M} \times \boldsymbol{B})_x - \frac{M_x}{T_2} \\ \frac{dM_y}{dt} &= \gamma(\boldsymbol{M} \times \boldsymbol{B})_y - \frac{M_y}{T_2} \\ \frac{dM_z}{dt} &= \gamma(\boldsymbol{M} \times \boldsymbol{B})_z + \frac{M_0 - M_z}{T_1} \end{aligned} \tag{3.11}$$

We now consider the simple case of a constant and homogeneous magnetic field $\boldsymbol{B} = B_0\hat{\boldsymbol{e}}_z$ and excitation of the equilibrium magnetization $\boldsymbol{M_0} = M_0\hat{\boldsymbol{e}}_z$ with a RF pulse resulting in transverse and longitudinal magnetizations $M_x(0), M_y(0), M_z(0)$. The Bloch equation for the longitudinal component M_z of the magnetization is solved by the exponential

$$M_z(t) = M_0 - (M_0 - M_z(0))e^{-t/T_1}. \tag{3.12}$$

If we introduce complex notation for the transverse magnetization $M_\perp(t) = M_x(t) + iM_y(t)$, the solution of the Bloch equations (3.11) for the transverse magnetization becomes simply

$$M_\perp(t) = M_\perp(0)e^{i\omega t}e^{-t/T_2^*} \tag{3.13}$$

The transverse magnetization $M_\perp$ precesses around the z-axis with the Larmor frequency ω_0 and decays exponentially with the time constant T_2^*, whereas the longitudinal magnetization recovers exponentially with time constant T_1 to the equilibrium magnetization. The time constant T_2^* that is used here describes the decay of the transverse magnetization due to reversible and irreversible dephasing. This behavior is commonly referred to as *free induction decay* or FID.

3.4 SPIN AND GRADIENT ECHOES

As stated above, the free induction decay of the transverse relaxation after excitation with a RF pulse is caused by dephasing due to spin-spin interactions and due to static inhomogeneities of the external magnetic field. The latter effect can be reversed e. g. by applying a RF pulse that flips the magnetization by 180° at a time $T_E/2$ after the excitation pulse. If we consider two spins that experience a slightly different external magnetic field, these spins will have acquired a phase difference of $\Delta\phi = \Delta\omega T_E/2$ after the time interval $T_E/2$. Applying a 180°-RF pulse inverts the phase between those two spins to $\Delta\phi = -\Delta\omega T_E/2$. Since the precession frequencies of these two spins are constant in time (if the spins remain at the same position), the phase difference $\Delta\phi$ will vanish after the time T_E after the excitation pulse and a so-called *spin echo* will form. This spin echo has the form of a reversed FID before the echo time T_E, and is similar to a FID after the echo time. If the echo time is increased, an exponential decay of the spin echo can be observed. The reason for this is that the 180°-pulse can only recover the dephasing that occurs due to static, local field inhomogeneities, but not the dephasing that is due to dynamic spin-spin interactions.

GRADIENT ECHO A different method for the generation of an echo relies on the application of an additional magnetic field gradient. This gradient changes the magnetic field in a position-dependent manner and hence changes the local Larmor frequencies. For simplicity, we consider a gradient field that has only a component $G_z = G$ parallel to the external magnetic field and varies linearly in z-direction. In a gradient sequence as illustrated in Fig. 8, the constant negative gradient in the time interval (t_1, t_2) causes a phase accumulation for a spin at position z and time t

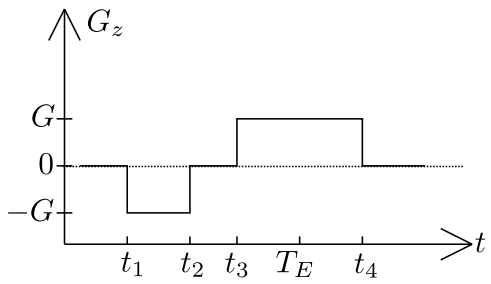

Figure 8: If this gradient switching scheme is applied after RF excitation at time $t_0 < t_1$, a gradient echo is produced at time T_E. The area under the negative first gradient lobe equals the first half of the second gradient lobe from t_3 to T_E.

in $[t_1, t_2]$ of $\Delta\phi = \gamma G z(t - t_1)$. During the second gradient lobe with a positive value of G, the phase accumulation of the same spin is

$$\Delta\phi = \gamma G z(t_2 - t_1) - \gamma G(t - t_3) \tag{3.14}$$

and it is obvious that the phase accumulation of each spin, independent of its z-position, vanishes at $t = t_3 + (t_2 - t_1) = T_E$. Hence, a *gradient echo* occurs at the time where the area under the second gradient lobe cancels out the area under the first gradient lobe.

3.5 SPATIAL ENCODING AND MR IMAGING

All spins in an homogeneous magnetic field have the same Larmor frequency ω_0; hence the FID that occurs after excitation does not contain any information about the localization of the spins. In order to produce an image, it is therefore necessary to spatially encode the signal, so that an image can be reconstructed. A means to achieve this is the spatial modulation of the magnetic field by overlaying of a magnetic gradient field $\boldsymbol{B_G} = \boldsymbol{G}(t) \cdot \boldsymbol{x}\hat{\boldsymbol{e}}_z$, so that the external magnetic field becomes

$$\boldsymbol{B}(\boldsymbol{x}, t) = \boldsymbol{B_0} + \boldsymbol{G}(t) \cdot \boldsymbol{x}\hat{\boldsymbol{e}}_z \tag{3.15}$$

For simplicity, we consider a simple one-dimensional example, which can easily be generalized to the three-dimensional case. We assume a spatially varying spin density $\rho(x)$ and an external magnetic field with time-dependent, overlaid gradients that vary linearly in x. Neglecting relaxation effects, the transverse magnetization after excitation can be written as

$$M_\perp(x, t) = \rho(x) e^{i\phi(x,t)} M_\perp(0) \tag{3.16}$$

Here $\phi(x,t)$ is the phase of the transverse magnetization that accumulated in the magnetic field $B(x,t) = B_0 + xG(t)$:

$$\begin{aligned}\phi(x,t) &= \int_0^t d\tau\omega(\tau) = \gamma\int_0^t d\tau B(x,\tau)\\ &= \omega_0 t + x\gamma\int_0^t d\tau G(\tau)\\ &= \omega_0 t + xk(t)\end{aligned} \tag{3.17}$$

with the definition of the *spatial frequency*

$$k(t) = \gamma\int_0^t d\tau G(\tau). \tag{3.18}$$

The RF signal that is detected in an MRI experiment is proportional to the spatial average of the transverse magnetization:

$$S(t) \propto \int dx M_\perp(x,t) \tag{3.19}$$

and, with the phase (3.17), can thus be written as

$$\begin{aligned}\tilde{S}(t) &= \int dx\rho(x)e^{i\omega_0 t}e^{ixk(t)}\\ &= e^{i\omega_0 t}\int dx\rho(x)e^{ixk(t)}\end{aligned} \tag{3.20}$$

Apart from a scaling factor, the measured RF signal $S(t) = S(k(t))$ is therefore the value of the Fourier transform of the spin density $\rho(x)$ at the point $k(t)$. Since $k(t)$ is determined by the gradient field $G(t)$, it is possible to measure $S(k)$ for arbitrary values of k; in particular, if $S(k_i)$ is measured in a sufficient number of points k_i, it is possible to determine an approximation of the spin density $\rho(x)$ by an inverse discrete Fourier transform (DFT):

$$\rho(x) \propto \sum_i S(k_i)e^{-ik_i x} \tag{3.21}$$

In MRI, $S(k)$ is often measured in an equidistantly spaced grid of $2N$ points in k-space centered at the origin. In the one-dimensional case, $\rho(x)$ can then be determined with a proportionality constant C as

$$\rho(x = C\sum_{n=-N}^{N} S(n\Delta k)e^{-ixn\Delta k}. \tag{3.22}$$

The distance Δk between two points in k-space determines the *field of view* (FOV) as

$$FOV = \frac{2\pi}{\Delta k} \tag{3.23}$$

this follows from the periodicity of the exponential in Eq. (3.21). Since the DFT is reversible, $\rho(x)$ can be calculated likewise at $2N$ equidistant values of x in image space; the spatial resolution of the image in the 1D case is thus

$$\Delta x = \frac{FOV}{2N} = \frac{2\pi}{2N\Delta k}. \tag{3.24}$$

In the three-dimensional case, $k(t)$ is replaced by a three-dimensional vector $\boldsymbol{k}(t)$ in a vector space commonly referred to as *k-space*. The value of $\boldsymbol{k}(t)$ is determined by the time integral over the gradient field $\boldsymbol{G}(t)$, by choosing appropriate gradient fields $\boldsymbol{G}(t)$, the value of $S(\boldsymbol{k})$ can be measured at arbitrary points in k-space. A special case is 2D imaging, here, only a thin slice of the volume is excited and k-space becomes two-dimensional. Consequently, only 2D gradient fields need to be applied.

SLICE SELECTION The spatial encoding with magnetic field gradients takes place after the spins have been excited with a RF pulse at time $t = 0$. This excitation can be *non-selective* in the sense that all spins in a given volume are excited; for this purpose, a RF pulse alone with the appropriate Larmor frequency suffices. It is, however, also possible to excite only a single slice, by applying a magnetic field gradient during the RF pulse. This gradient detunes the Larmor frequency along its direction, so that only a single plane perpendicular to the gradient direction has a Larmor frequency that matches the frequency of the pulse. The thickness and the profile of the slice that is excited by the pulse depend on the frequency spectrum and the bandwidth of the pulse as well as on the gradient amplitude.

The excitation of a single, sufficiently thin slice in the xy-plane, as opposed to non-selective excitation, leads to a signal

$$S(k_x, k_y, t) \propto \int_{x,y} M_{xy}(x, y, t_0) e^{-i(k_x x + k_y y)} dx dy \tag{3.25}$$

so that the k-space needs to be sampled only in two dimensions.

K-SPACE SAMPLING To calculate the inverse Fourier transformation without additional complications such as regridding, k-space needs to be sampled in a equidistantly spaced grid with $N_x \cdot N_y$ points. Fig. 9 illustrates a simple, single-slice 2D gradient echo sequence with 2D cartesian readout. Immediately after an excitation, the phase is given by $k_x = k_y = 0$. A *phase encoding* gradient G_y is applied in y-direction for the time τ_y, together with a *read dephasing* gradient $-G_x$, applied for the time span $\tau_x/2$ to locate the point $(k_x, k_y) = \gamma(-G_x\tau_x/2, G_y\tau_y)$ in k-space. Subsequently, a *readout* gradient G_x is applied for the time span

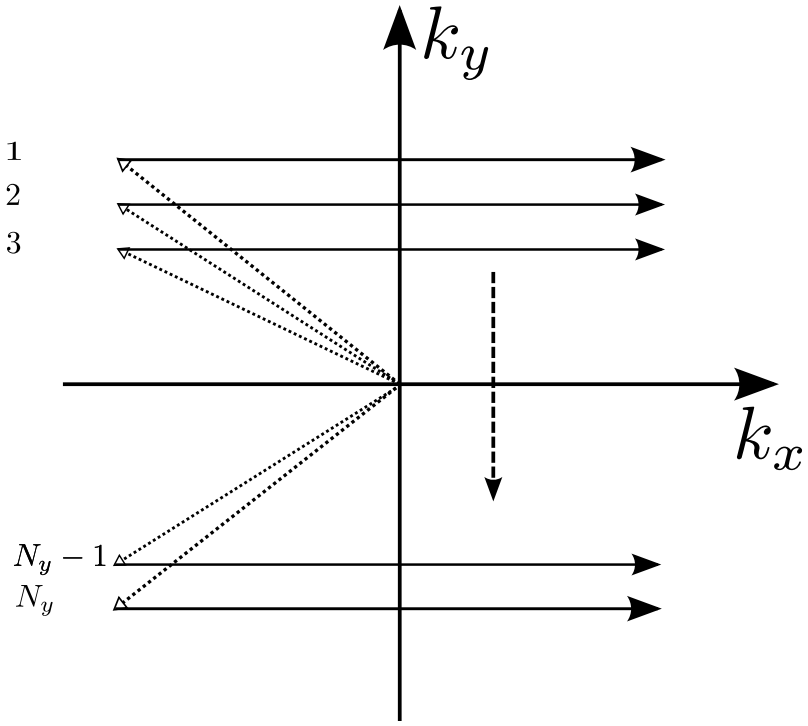

Figure 9: 2D cartesian sampling of k-space in the case of a simple, single-slice 2D gradient echo sequence.

τ and N_x signal points are collected along a line in k-space. This experiment is repeated N_y times with varying values of the phase encoding gradient, so that k-space is finally sampled at $N_x \cdot N_y$ data points.

A multitude of different k-space sampling schemes (e. g. cartesian, radial, spiral) and phase-encoding orders (e. g. sequential, centric, reverse centric) have been proposed and are in use. For an overview, the reader is referred e. g. to [29].

SEQUENCES In MR imaging, the combination of the steps excitation, possibly refocusing pulses, spatial encoding, echo generation and signal acquisition is generally referred to as *pulse sequence*. An important parameter for a sequence is its repetition time T_R, which is generally defined as the time from one excitation pulse to the next.The choice of various sequence parameters such as T_E, T_R or the flip angle α has strong influence on the image contrast that is generated between tissues that differ e. g. in their relaxation times.

In MR imaging, a wealth of different sequences exist, and new sequences are developed (and named according to imaginative acronyms) on a regular basis. These sequences can differ in various parameters, such as the way in which the echo is generated (e. g. spin-echo or gradient-echo), the image contrast that is generated by variation of sequence parameters such as T_E, T_R or the

flip angle α or the k-space sampling scheme (cartesian, radial, spiral, 2D or 3D).

3.6 CONTRAST AGENTS

The scope of the medical application of magnetic resonance can be widened considerably through the application of *contrast agents*. In the context of magnetic resonance imaging, a contrast agent is a substance that alters the relaxation times T_1, T_2 and T_2^* in its vicinity. Depending on the biological and chemical properties of the contrast agent as well as the way of administration, different tissues are affected differently by the contrast agent, so that the image contrast can be altered significantly, thereby providing a wealth of additional information about the tissue.

A fundamental difference to other medical imaging modalities such as X-ray imaging or computed tomography is that in MR imaging the contrast agent is never visualized directly. Instead, the effect of the contrast agent on the relaxation of spins is observed.

The most widely used contrast agents in MR imaging are based on the Gadolinium ion Gd^{3+}. Due to its seven unpaired electrons, this ion is strongly paramagnetic and thereby reduces the T_1 and T_2 relaxation times. To reduce the toxicity of Gd^{3+}, it is usually embedded into a chelate complex with ligands such as DTPA (*diethylene triamine pentaacetic acid*).

The interaction of the unpaired electrons of the Gadolinium ion with the hydrogen nuclei of water results in a reduction of the relaxation times T_1 and T_2 by dipole-dipole interaction. This effect is a short-range effect, the Gadolinium ion affects only spins in its immediate vicinity.

The presence of a paramagnetic contrast agent in tissue also results in an increase of the local magnetic susceptibility. In an external magnetic field, this results in a higher local field in the vicinity of the contrast agent. If the contrast agent is distributed homogeneously in the tissue, this leads to an increase of the Larmor frequency and equilibrium magnetization. If, however, the contrast agent is distributed inhomogeneous, local magnetic field gradients arise between the compartments that contain contrast agent and those that do not. These gradients shorten the T_2^* relaxation times of the tissue; an important characteristic of this effect is that it acts over mesoscopic distances. This is particularly relevant in a situation where the contrast agent is confined to blood vessels and cannot extravasate into the interstitial space – here, the induced gradients strongly increase the T_2^* effects of the contrast agent.

The effect of contrast agent on the longitudinal relaxation time T_1 of a homogeneous medium is described by:

$$R_1 = R_{1,0} + r_1 \cdot c \tag{3.26}$$

where $R_1 = T_1^{-1}$ is the relaxation rate in presence of contrast agent, $R_{1,0}$ is the relaxation rate in absence of contrast agent, r_1 is the *relaxivity* and c is the concentration of the contrast agent. Generally, the r_1-relaxivity of a given contrast agent depends on a variety of factors such as the magnetic field strength, the temperature and the chemical composition of the contrast agent.

The majority of contrast agents that are used in MR imaging are extracellular, hence, the contrast agent is usually distributed inhomogeneously in tissue. In that case, the susceptibility effects of the contrast agent that were discussed above contribute strongly to the effect of the contrast agent on the relaxation of the transverse magnetization. Consequently, the r_2^*-relaxivity depends strongly on the structure of the tissue and the distribution of contrast agent in this structure, so that a functional relation can only be provided for special situations such as intact brain tissue. Here, a dependence of the relaxivity on the vessel size and orientation has been observed within certain regimes and used for *vessel size imaging* [32]. Additional difficulties arise if the distribution of the contrast agent in the tissue is not constant during the measurement. This may happen e. g. in the imaging of tumors: the contrast agent arrives in the blood vessels, causing small gradients and thereby shortening the transverse relaxation time T_2^*. Gradually, the contrast agent leaks into the interstitial space, the local gradients and hence the effect of the contrast agent on T_2^* reduce, although the macroscopic concentration in the tissue remains unchanged or even increases due to the accumulation of contrast agent in the interstitium.

4 DYNAMIC CONTRAST-ENHANCED MRI

In the context of bolus-tracking measurements, the quantification of perfusion is composed of two distinct steps. In the first step, the time-dependent concentrations of contrast agent or tracer after bolus administration are measured in a supplying artery and in the tissue of interest. In the second step, hemodynamic parameters such as blood flow, blood volume or the flow across vessel wall are derived from the form of these curves using the theory of tracer kinetics. This chapter discusses the first step, the measurement of time-dependent contrast agent concentration using magnetic resonance imaging (MRI).

It is the purpose of the MRI acquisition to produce time-resolved signal intensities $S(t)$ before, during and after the administration of the contrast agent. Care must be taken to find a suitable balance between a range of factors influencing the data quality, these factors include the contrast-to-noise ratio (CNR) as well as the temporal and spatial resolution of the measurement. Contrast agent concentrations or approximations thereof can be derived from the measured signal intensities using MR signal theory. Depending on the degree of sophistication, it may be necessary to acquire further calibration data, such as precontrast T_1 values or the actual flip angle distribution.

The first part of this chapter briefly presents two popular methods for the MRI acquisition, the second part describes MR signal analysis with the aim to derive contrast agent concentrations (or approximations thereof) from the measured signal intensities. The third part of this chapter deals with several aspects of the MR acquisition itself.

4.1 DSC OR DCE MRI

The presence of contrast agent causes changes of the longitudinal and transverse relaxation rates R_1, R_2 and R_2^*. Depending on the MR sequence used for the acquisition, these changes lead to changes of the measured signal intensity, which in turn can be utilized to estimate the contrast agent concentration using MR signal theory. Two different approaches have seen widespread use for the dynamic measurement of contrast agent concentration: In *dynamic contrast-enhanced* (DCE) MRI, the $T_1 = 1/R_1$ shortening effect of paramagnetic contrast agents is employed. When images are acquired with a T_1-weighted sequence, the presence of contrast agent thus leads to an increase of the signal intensity.

Dynamic susceptibility contrast-enhanced (DSC) MRI, on the other hand, utilizes the fact that the contrast agent produces local magnetic field gradients. When the signal is acquired with a T_2- or T_2^*-weighted sequence, these gradients cause a dephasing of the water protons and hence a decrease of signal intensity.

For most organs of the body, DCE MRI is the preferred method for perfusion measurements [4, 6, 33–35], since either the blood volume is large, or the contrast agent can readily extravasate into the interstitial volume, so that the total amount of contrast agent is large enough to cause strong signal changes. In the brain, however, the setting is different. Not only is the cerebral blood volume small (3-5 ml/100m [36]), but also, the tracer is confined to the intravascular space by the blood-brain barrier. Thus, the total amount of contrast agent in brain tissue is small, leading only to small signal changes in DCE MRI. The compartmentalization of the tracer to the intravascular space, however, causes strong magnetic field gradients on a microscopic scale [12], so that the T_2^* effects of contrast agent and hence the signal changes in healthy brain parenchyma are strong [11]. This has lead to a widespread use of DSC MRI for the assessment of cerebral perfusion [1, 37–40] in a wide range of applications, including brain tumors and multiple sclerosis.

Absolute quantification of cerebral hemodynamics with DSC MRI, however, remains challenging. For a quantitative analysis, it is necessary to measure tracer concentrations both in the tissue of interest and in a tissue-feeding artery (see chapter 5). However, the T_2^* relaxivities of contrast agent are different between artery and tissue, thus producing a scaling error in the quantification. Moreover, if the tracer can leak into the interstitial volume due to blood-brain barrier leakage, the local magnetic field gradients causing the susceptibility contrast are reduced, which leads to smaller signal changes, thus distorting estimates of the tracer concentration. Additionally, the tracer that accumulates in the interstitial space causes T_1 effects and thus a signal increase, which leads to underestimation of the tracer concentration. To minimize these T_1 effects, several approaches such as data truncation [41] or modeling [14, 16] have been proposed, but the loss of susceptibility contrast cannot be easily corrected for. This raises the question, whether, despite the lower CNR, a T_1-weighted sequence would be more suitable for the quantification of cerebral hemodynamics, both in healthy brain parenchyma and in lesions with blood-brain barrier leakage. The remainder of this chapter thus focuses on MRI signal analysis and acquisition with T_1-weighted MRI.

4.2 MR SIGNAL ANALYSIS

The purpose of MR signal analysis in the context of DCE MRI is to derive the tracer concentration $c(t)$ from the measured signal intensity $S(t)$. Two distinct aspects play a key role in MR signal analysis:

1. *Relaxation:* The contrast agent shortens the T_1 relaxation time of the water protons in its vicinity.
2. *Signal:* The shortening of T_1 leads to an increase of signal intensity. The amount of signal increase depends on the pulse sequence that was used for the acquisition as well as on the imaging parameters.

The presence of a paramagnetic contrast agent leads to an increase of the longitudinal relaxation rate R_1 and a shortening of the longitudinal relaxation time $T_1 = 1/R_1$. Whereas the actual interactions leading to this effect are quite complex, it has been shown [42] that the relation of the relaxation rate to the concentration is linear for concentrations that occur in typical DCE MRI measurements and is of the form

$$R_1 = R_{10} + r_1 c \tag{4.1}$$

Here, R_{10} is the precontrast relaxation rate, r_1 is the *relaxivity* of the contrast agent and c is the concentration. The time-dependent concentration in the tissue can then be derived from the change in relaxation rate $R_1(t) - R_{10}$ and the relaxivity r_1 as

$$c(t) = \frac{R_1(t) - R_{10}}{r_1} \tag{4.2}$$

if the relaxivity of the contrast agent is known. However, under the assumption that the relaxivity is independent of the tissue type, the value of r_1 cancels out in a quantitative tracer kinetic analysis as in chapter 5 .

It remains to derive the change in relaxation rate from the measured signal intensity. In virtually all sequences that are used for DCE MRI, the signal intensity $S(t)$ is of the form [43]:

$$S(t) = \Omega \cdot e^{-T_E/T_2^*} \cdot \sin(\alpha) \cdot m_z(R_1(t)) \tag{4.3}$$

Here, Ω is a global calibration constant, which absorbs the coil sensitivity and the equilibrium magnetization. The exponential describes the T_2^*-weighting, α is the flip angle and m_z is the longitudinal magnetization as a function of the relaxation rate.

In general, the echo time T_E is chosen so short that the influence of changes in R_2^* is negligible, so that all factors in Eq. (4.3) apart

from $m_z(R_1(t))$ can be regarded as constant in time. Thus, we can write the signal $S(t)$ in presence of contrast agent and the baseline signal S_0 with a quantity $\Gamma(\boldsymbol{x})$ that is constant in time as

$$\begin{aligned} S(t) &= \Gamma(\boldsymbol{x}) \cdot m_z(R_1(t)) \\ S_0 &= \Gamma(\boldsymbol{x}) \cdot m_z(R_{10}) \end{aligned} \tag{4.4}$$

Γ is, however, not necessarily constant in space, since it absorbs the coil sensitivity and the sinus of the flip angle, which both may vary inside the acquired volume, e. g. if surface coils are used for the signal reception.

The exact form of the function m_z in Eq. (4.4) is determined by the sequence that is used for the acquisition and in general depends not only on the relaxation rate, but also on sequence parameters such as the repetition time between excitation pulses or the flip angle.

However, even without knowledge of the exact form of m_z, the change in relaxation rates and thus the contrast agent concentration can be approximated using either the *signal enhancement* or the *relative signal enhancement*.

4.2.1 *Signal enhancement*

Subtraction of eqs. (4.4) yields

$$S(t) - S_0 = \Gamma(\boldsymbol{x}) \cdot [m_z(R_1) - m_z(R_{10})] \tag{4.5}$$

With the assumption that m_z is linear in R_1, the change in relaxation rate depends in a linear fashion on the change in signal intensity:

$$R_1(t) - R_{10} = k \cdot \Gamma^{-1}(\boldsymbol{x}) \cdot (S(t) - S_0) \tag{4.6}$$

and the tracer concentration (4.2) is thus proportional to the signal enhancement (SE) $S(t) - S_0$:

$$c(t) = \frac{k}{r_1}\Gamma^{-1}(\boldsymbol{x})(S(t) - S_0) =: \hat{k} \cdot (S(t) - S_0) \tag{4.7}$$

The value of the factor $\hat{k}$ in Eq. (4.7) cannot be determined without additional calibration measurements of e. g. the flip angle and the coil sensitivity profile. However, if $\hat{k}$ is equal in the artery and in the tissue of interest, the value of $\hat{k}$ cancels out in a quantitative, tracer-kinetic analysis (see chapter 5).

If this equality is not given, for example if surface coils with a rather inhomogeneous coil sensitivity are used or if the B_1-field is inhomogeneous, the ratio of $\hat{k}_{\text{artery}}$ and $\hat{k}_{\text{tissue}}$ enters directly as a scaling error of the perfusion parameters.

4.2.2 *Relative signal enhancement*

Under the assumption that $\Gamma(\boldsymbol{x})$ is constant in time, division of Eqs. (4.4) yields

$$\frac{S(t)}{S_0} = \frac{m_z(R_1(t))}{m_z(R_{10})} \tag{4.8}$$

so that $R_1(t)$ can be determined as

$$R_1(t) = m_z^{-1}\left\{ m_z(R_{10}) \cdot \frac{S(t)}{S_0} \right\} \tag{4.9}$$

Again with the assumption of m_z being linear in R_1, the change in relaxation rate and thus the concentration in Eq. (4.2) can be expressed in terms of the relative signal enhancement (RSE) as

$$c(t) = \frac{R_{10}}{r_1} \frac{S(t) - S_0}{S_0} \tag{4.10}$$

The scaling factor in (4.10) is independent of both flip angle and coil sensitivity, which both may vary in space. However, the formula shows that an additional measurement of R_{10} is required to accurately quantify the tracer concentration using the relative signal enhancement. Without the knowledge of the precontrast relaxation rates R_{10} in artery and tissue, the approximation of the tracer concentrations with the relative signal enhancement would produce an error with the amplitude of $R_{10,\text{artery}}/R_{10,\text{tissue}}$, even in the linear regime of m_z.

4.2.3 *Direct measurement of R_1 and R_2^**

The approximation of the contrast agent concentration using the signal enhancement or the relative signal enhancement both rely on the assumption that m_z depends linearly on R_1. Although this assumption is generally valid for small concentrations and relaxation rates, it does not necessarily hold for large concentrations that can occur e. g. in vessels during the first pass of the contrast agent.

If we consider the example of a spoiled gradient-echo (SPGR) sequence with flip angle α and repetition time T_R in the steady state, m_z has the following form [29]:

$$\begin{aligned} S &= M_0 \cdot \sin(\alpha) e^{-T_E R_2^*} \cdot m_z(R_1) \\ m_z(R_1) &= \frac{1 - e^{-T_R R_1}}{1 - \cos(\alpha) e^{-T_R R_1}} \end{aligned} \tag{4.11}$$

This dependence of m_z on the relaxation rate for a SPGR sequence is illustrated in Fig. 10. Clearly, m_z is linear only for small

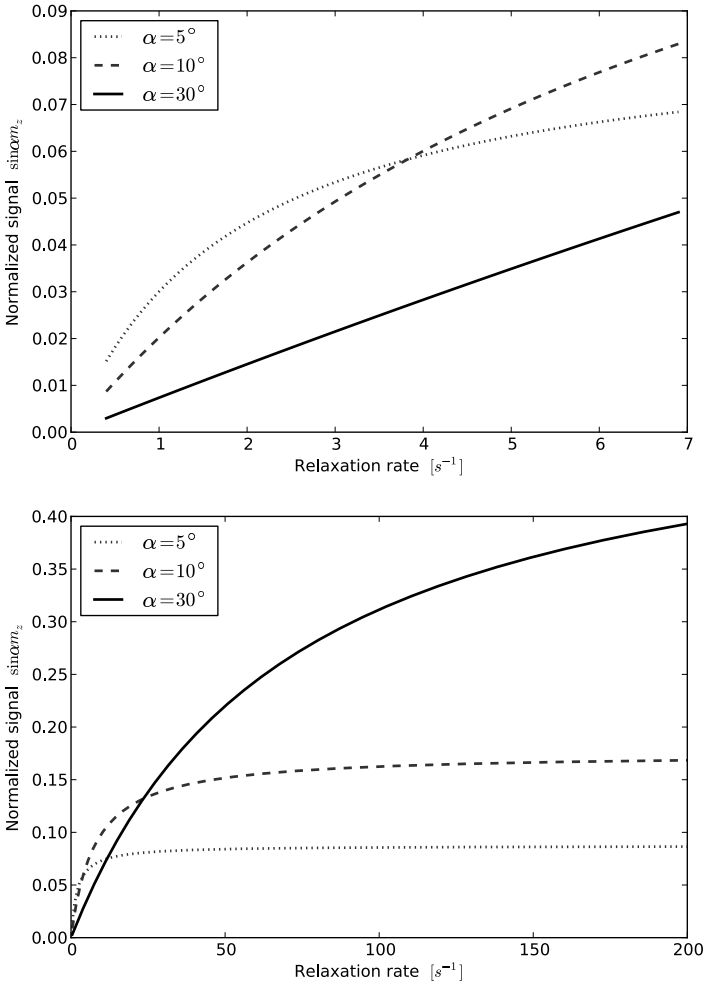

Figure 10: Normalized longitudinal magnetization produced by a SPGR sequence with different flip angles and $T_R = 2.0\,\text{ms}$. Top: R_1 values that occur in blood plasma with typical CA concentrations [42]. Bottom: the same sequence with high relaxation rates, demonstrating the nonlinear behavior of m_z

values of R_1, for higher values of the longitudinal relaxation rate, a nonlinear regime and even saturation is reached. The linear regime and the signal yield can be extended if higher flip angles are used. However, a higher flip angle deposits more RF energy in the tissue, so that in clinical practice the maximal value of the flip angle is limited by the specific absorption rate (SAR). Practically, the flip angle is often chosen as high as the SAR limit allows.

Since the highest concentration of contrast agent in DCE MRI measurements typically occur in the arteries during the first pass of the contrast agent bolus, the approximation of concentration either by relative or absolute signal enhancement typically results in an underestimation or even clipping of the arterial input function. This, in turn, would be directly reflected in the estimates of tissue blood flow or tissue blood volume in a subsequent tracer kinetic analysis.

The influence of T_2^* effects in Eq. (4.3) is typically small in DCE MRI, since the echo time T_E is usually in the order of milliseconds or below. However, if high concentrations of contrast agent occur, such as during the first pass of the bolus in the artery, ignoring T_2^* effects may lead to a significant underestimation of the arterial concentration.

If the above mentioned effects cannot be minimized either through optimization of the acquisition sequence (i. e. optimal choices of sequence parameters like T_R, T_E, α and possibly saturation or inversion times) or the injection protocol (e. g. slower injection rates, smaller dose of contrast agent, splitting into several injections), a possible remedy is to directly measure the $R_1(t)$ and $R_2^*(t)$ relaxation rates at each time point at the cost of temporal resolution.

This approach is demonstrated in [44] and [45], in which a saturation-recovery gradient multi-echo sequence is employed. Briefly, this sequence employs a global saturation pulse and, after a certain saturation recovery time T_S, acquires a series of images at different echo times for each time point. From the series of signal intensities at each time point t, the relaxation rate $R_2^*(t)$ can be determined by fitting a monoexponential to the data. For the calculation of $R_1(t)$, a precontrast measurement of R_{10} and R_{20}^* is necessary; this precontrast measurement is carried out once with two different saturation recovery times T_S. With knowledge of R_{10} and the previously determined $R_2^*(t)$, $R_1(t)$ can then be determined for each time point.

4.3 MR ACQUISITION

The setup of a DCE MRI experiment involves the choice of the MR scanner, in particular with respect to the field strength, as well

as the choice of contrast agent, injection protocol and imaging sequence, and, lastly, the careful optimization of the sequence with respect to measurement properties such as CNR, temporal and spatial resolution and spatial coverage. Each of these choices affects and depends on the others, and is also influenced by the tissue under investigation and the actual objective of the measurement.

In general, setting up a measurement protocol for DCE MRI involves a trade-off between

CONTRAST-TO-NOISE RATIO In the context of DCE MRI, the "data quality" cannot be assessed with the conventional quantity *signal-to-noise ratio*. Instead, the contrast-to-noise ratio (CNR) should be used, which in this context describes the amount of signal change caused by the presence of contrast agent compared to the noise in the data. A possible measure of CNR is the ratio of the maximum of the signal-time curve and the noise in the baseline signal (before the arrival of contrast agent). CNR can be increased by sacrificing spatial or temporal resolution, by increasing the dose of contrast agent or through the use of a higher field strength. Moreover, CNR depends on the tissue type, especially on the blood volume in the tissue.

SPATIAL RESOLUTION AND COVERAGE Obviously, the spatial resolution needs to be high enough to identify the structures of interest. Moreover, for a quantitative analysis, it is necessary that an arterial input function can be measured. For this purpose, it is beneficial if the voxel size is so small that at least one, better several, voxels can be identified that are completely embedded in an artery to reduce the influence of partial volume effects. If this cannot be achieved due to other constraints, it is sometimes possible to find a voxel that is completely embedded in large venous vessel, which then allows for correction of partial volume effects(see 6.3). It is important to mention that the signal-to-noise ratio of an MR acquisition is proportional to the voxel volume and hence the in-plane resolution, so that large signal gains can be achieved by reducing the spatial resolution.

TEMPORAL RESOLUTION Another important matter is the temporal resolution of the measurement. Intuitively, one would assume that the measurement is better the faster it is. Unfortunately, this is not true in MRI, since a faster measurement almost inevitably leads to a decrease in signal-to-noise ratio (unless sophisticated acceleration schemes are used). Moreover, a reduction in sampling speed can be utilized to increase either spatial coverage, spatial resolution or CNR. It is thus of importance to identify the minimal temporal

resolution that still allows for accurate quantification. One requirement is that all concentration-time curves, in particular the rapid signal changes in the artery during the first pass of the contrast agent, are sufficiently sampled to observe the broadening of the contrast agent bolus between the artery and the tissue (this already indicates that the term "sufficient sampling" includes not only high temporal resolution, but also sufficient CNR). In general, it is reasonable to assume that the temporal resolution should be faster than the time scales of the processes that are to be observed. Since the shortest time scales in the context of perfusion quantification are the plasma transit times which are usually not faster than 3 to 5 seconds, a sampling interval of less than 2 seconds is usually recommended [4, 46] for the assessment of plasma flow.

4.3.1 *Dynamic imaging*

The ultimate aim of imaging in the context of perfusion quantification is to produce temporally resolved and accurate measurements of tracer concentrations in tissue and in arterial blood.

PULSE SEQUENCES For the assessment of hemodynamics from time-resolved data, DCE MRI usually employs 2D [47–49] or 3D [50–52] sequences with a spoiled gradient-echo readout.

With 2D sequences, high temporal resolutions can be achieved by acquiring only a limited number of slices, thereby sacrificing spatial coverage. 3D sequences, on the other hand, provide large spatial coverage and resolution, but require more effort to achieve sufficient temporal resolution. Through the introduction of parallel imaging [53, 54] and view sharing [55, 56], data quality and speed of 3D acquisition have become considerably better and are gradually replacing 2D measurements in current practice.

The use of 3D acquisitions is beneficial for a number of reasons. For example, it is possible that the precise location of a pathology cannot be determined on precontrast images – and contrast agent cannot be administered before a perfusion measurement. With a 2D acquisition, only a limited number of slices can be placed in the area where a pathology is suspected, and the risk of missing the pathology is greatly increased. A 3D acquisition in the same situation might provide coverage of e. g. the whole brain and thus guarantees to capture *all* existing lesions

Likewise, longitudinal studies benefit as well from the use of 3D acquisitions, since reproducible slice placement between MR examinations is often an issue with 2D acquisitions. Moreover, even if the same slice positioning can be achieved, it is possible that location or size of the pathology have changed, so that

acquisition of a single slice often does not allow conclusions about the state of the pathology. This is of particular relevance if the characterization of very heterogeneous regions such as metastases or primary tumors is an objective of the measurement – here, a 3D acquisition could capture the whole tumor, whereas a slice of a 2D acquisition might capture either the highly vascularized tumor rim or a central necrotic region with no perfusion at all, with a corresponding outcome of perfusion quantification.

ACCELERATION To reduce scan time, or, correspondingly, increase the temporal resolution, it is possible to acquire only a part of the k-space (undersampling), thereby saving data acquisition time, and reconstruct the full k-space data after the measurement by utilizing different properties of k-space.

Partial Fourier methods employ the symmetry of k-space to reduce the number of phase-encoding steps, either in phase-encoding or slice-encoding direction, so that fewer k-space lines are to be acquired. Typical partial Fourier factors are 5/8, 6/8 or 7/8, however the scan time reduction leads to a loss of signal-to-noise ratio.

A different class of methods is formed by the *parallel imaging* algorithms (see e. g. [57] for a review or [58] for a comprehensive overview). There is a large number of algorithms available, including SENSE, SMASH, PILS, CAIPIRINHA and GRAPPA. These methods have in common that they use an array of receiver coils for the data acquisition and acquire only a subset of the k-space lines, typically every second or every third line. Such an undersampling of k-space would lead to aliased images; therefore, parallel imaging methods employ the spatial sensitivity profiles of the multiple coils to reconstruct the full data either in k-space, such as in GRAPPA, or in image space, such as in SENSE.

For time-resolved angiography, so-called *view sharing* techniques such as TRICKS [59], TREAT [55] and TWIST [56] have been developed. These methods employ temporal k-space undersampling, where the central part of k-space is sampled more often than peripheral regions of k-space. For each reconstructed time point, the peripheral k-space data is then reconstructed using data acquired at earlier (forward data sharing) or later (backward data sharing) time points. The underlying assumption of these methods is that data in the central part of k-space, which is responsible for image contrast, changes more rapidly during administration of contrast agent than data in peripheral k-space regions, so that it is sufficient to update the peripheral k-space data less often. The image quality and the temporal resolution that can be achieved with these methods depend on the size of the central k-space region that is updated often(obviously, a

larger central region results in less artifacts and slower measurement) and the extent of undersampling in the peripheral k-space. A further increase in measurement speed is achieved with the TREAT and TWIST sequences through the additional use of parallel imaging, which further reduces the amount of k-space data that is sampled.

The TWIST scheme is applied in the $k_y - k_z$ (phase encoding) plane of k-space, the readout direction k_x is neglected, since readout of a single k-space line is fast. The phase encoding plane is divided by a critical distance k_c into a central, low-frequency region A and a complimentary high-frequency region B. Region B is further divided into N subsets, so that each point in B is in exactly one subset. During the acquisition, the full k-space data is acquired only once, either for the first or the last image. For all other images, only region A and one of the subsets in B is acquired, the missing B subsets are copied from earlier or later measurements. Hence, the degree of undersampling with TWIST is characterized by two parameters pA and pB. pA describes the central portion of k-space, $pB = 1/N$ is the fraction of the region B that is acquired for each image.

4.3.2 *Contrast agents and injection protocol*

All standard MR contrast agents can be used for dynamic imaging. As a rule of thumb, the vascular parameters such as blood flow and blood volume are determined from the dispersion of the first pass of contrast agent between artery and tissue, whereas extravascular parameters such as the permeability surface area product or the interstitial volume are determined from the form of the later phase. Hence, the contrast agent administration needs to be accomplished in a way that allows for the observation of a first pass, typically, the contrast agent is injected as a *bolus* with a high injection rate in the order of 2 to 4 ml/s.

Typically, a standard dose of contrast agent (0.1 mmol/kg body weight) is used. Most contrast agents have a concentration of 0.5 mmol/l so that for a 70 kg patient 14 ml of contrast agent are injected. A notable exception is Gadovist with the double concentration, allowing for sharper bolus profiles. Care should be taken that the arterial concentration remains in the linear regime even at the peak concentration during the first pass of the contrast agent, in order to avoid an underestimation of the AIF. For this purpose, the injection flow or the dose of contrast agent can be reduced. This approach, however, might render it impossible to observe the broadening of the bolus, in particular in weakly perfused tissue. To circumvent this problem, it has been proposed in several studies to construct the AIF from a *prebolus measurement* [9, 60], where the measurement is preceded by a measurement

with a very small amount of contrast agent. Through shifting and summing up the arterial concentration curve produced by the prebolus, an AIF can be reconstructed that does not suffer from saturation effects. This approach, however, requires additional post-processing time and effectively doubles the measurement time, which is often unfeasible in clinical practice.

An interesting compromise might be to split the single, standard-dose injection into two half-dose injections [49, 61]. Thereby, the peak concentration could be reduced substantially, while maintaining sharp bolus profiles and the full dose of contrast agent.

If measures of permeability are an objective of the measurement and if extravasation of the contrast agent is expected, protein-bound tracers should be avoided. Firstly, the relaxivity of such contrast agents depends on the protein concentration which is usually different between blood plasma and interstitial fluid, so that the tracer concentration cannot be readily determined. Furthermore, the pharmacokinetics differ between protein-bound and unbound tracer particles, obviously, unbound particles can pass the vessel walls more easily than protein-bound particles.

4.3.3 *Calibration measurements*

If the concentration-time curves are to be approximated using the relative signal enhancement, a measurement of the precontrast relaxation rate R_{10} or, equivalently, the precontrast T_{10} time is necessary. For 2D saturation recovery acquisitions, this is usually done by acquiring several datasets with varying saturation recovery times T_S before the administration of contrast agent. The precontrast saturation recovery signal depends exponentially on T_S and R_{10}:

$$S \propto \left(1 - e^{-T_S R_{10}}\right) \tag{4.12}$$

so that R_{10} (and M_0) can then be determined by fitting Eq. (4.12) to the measured data (e. g. [34, 49]).

Although this approach is considered the gold standard for T_1 mapping, the long acquisition times render inversion-recovery approaches unfeasible for T_1 mapping in 3D datasets.

Therefore, T_1 mapping for 3D datasets is usually performed with 3D SPGR acquisitions with several flip angles [62–65]. Precontrast T_{10} values can then be obtained by fitting the measured data to the signal equation of a 3D SPGR sequence.

In particular at higher field strengths, an inhomogeneous distribution of the flip angle α cannot be ruled out. Since the actual flip angle enters into the calculation of T_1, it is advisable to measure the actual flip angle and use this correction for the calculation of T_1 [66, 67].

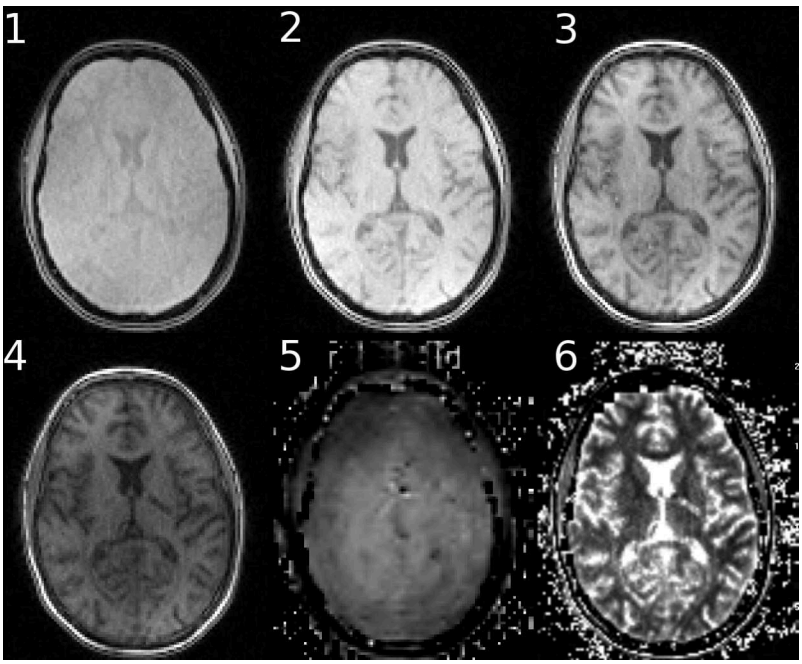

Figure 11: Calculation of a precontrast 3D T_1 map. Images 1 to 4: a representative slice of 3D volumes acquired with flip angles of 2.5°, 5°, 10° and 19°, image 5: map of the relative flip angle, scaled from 70% to 150%, image 6: resulting T_1 map, scaled from 0 to 2000 ms

Fig. 11 shows an example of this 3D T_1 mapping strategy. Four 3D volumes (matrix size 128×104, 44 slices) of the brain were acquired with flip angles of 2.5°, 5°, 10° and 19° and a constant repetition time $T_R = 3.1$ms (see images 1 to 4 in Fig. 11).

A map of the relative flip angle $\alpha_{\text{measured}}/\alpha_{\text{preset}}$ was measured using a pulsed steady-state sequence [67] with alternating repetition times T_R of 20 and 100 ms. The resulting map of the flip angle distribution is shown in image 5 in Fig. 11 and was used to calculate the T_1 map (image 6) from the four volumes measured with variable flip angles.

Unfortunately, the pulsed steady-state sequence is not generally available as a product sequence, so that a measurement of the actual flip angle and thus quantitative 3D T_1 mapping with a variable flip angle approach is currently not feasible in a clinical setting. Therefore, the most reliable strategy for the approximation of contrast agent concentration from 3D DCE MRI is currently the absolute signal enhancement (see 4.2.1), since quantitative values of tissue and blood T_1 are a prerequisite for the use of relative signal enhancement.

5

TRACER KINETICS – QUANTIFICATION OF HEMODYNAMICS

The overall aim of perfusion quantification is to derive information about the hemodynamic status of the tissue of interest from the measured concentration (or signal) time curves. Several strategies are feasible for this purpose, the most simple is a visual analysis of the dynamically acquired images. This form of analysis allows for quick detection of areas with e. g. perfusion defects or blood-brain barrier leakage (see Fig. 12), however, it is of limited use e. g. for the purpose of therapy monitoring, since it does not yield any quantitative scores.

PIXEL LEVEL OR REGION LEVEL Generally speaking, all parameters that go beyond a purely visual characterization of perfusion patterns can be calculated either on the pixel level or on the *region of interest* (ROI) level. In pixelwise calculations, the signal-time course of each pixel is evaluated and one or more parameters are derived from each curve, thereby producing images or *maps* of each parameter. In a ROI analysis, the signal intensities of all pixels in the region are averaged for each time point, so that a single, averaged signal-time course is produced, which is then further evaluated.

An analysis on the region level is usually more robust and accurate, since averaging over several pixels increases the contrast-to-noise ratio – on the downside, information about potential heterogeneity in the region is lost. A popular approach is to calculate a map of a robust parameter such as area under the

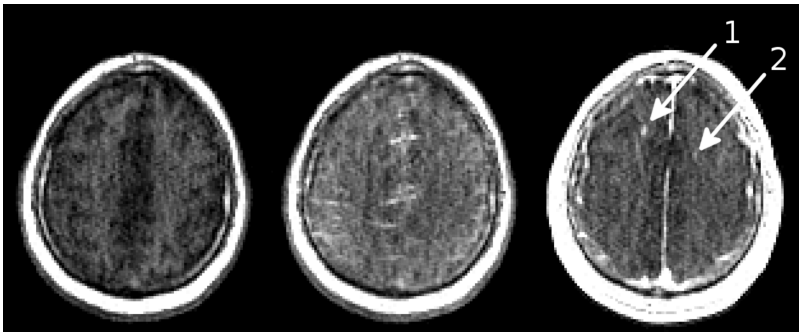

Figure 12: Three phases from a perfusion measurement in a patient with multiple sclerosis. Left: before arrival of contrast agent, center: arterial phase, right: late enhancement. In the late phase, two contrast-enhancing lesions (arrows) can be identified

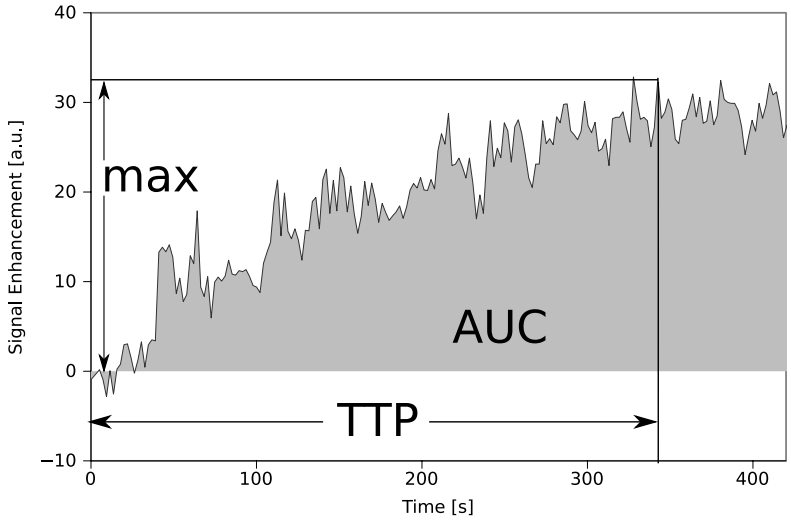

Figure 13: Illustration of several descriptive parameters: AUC: area under the curve (shaded); max: maximal signal enhancement; TTP: time to peak. This curve was measured in lesion #2 in the dataset shown in Fig. 12.

curve (see below) and use this map to localize and define a region; the averaged curve of this region can then, due to the increased CNR, be further analyzed with a more sensitive method.

The simplest form of quantification derives *descriptive* or *semi-quantitative* parameters from the form of the tissue curve alone. Popular parameters of this type are, among others, the *area under the curve* (AUC), the maximum of the curve, the time to peak and the bolus arrival time (see Fig. 13). All these parameters have in common that they in one way or another describe the form of the tissue curve.

Although these parameters are easy to calculate, they have several drawbacks. Their interpretation in terms of physiology is unclear, e. g. a large AUC may either be related to a large vascular volume, or to a large vessel wall permeability and consequently much extravasation. Likewise, a large maximum value might be caused either by strong enhancement during the first pass of contrast agent due to high values of blood flow and blood volume and or by very slow enhancement, where the peak value is reached at the end of the measurement.

Moreover, the values of semiquantitative parameters depend very much on acquisition parameters, such as the total acquisition time, the speed and dose of contrast agent injection or image contrast. Therefore, they are of limited use for cross-sectional or longitudinal studies.

Obviously, the exact form of the tissue concentration-time curve is determined by two different factors: the hemodynamic properties of the tissue itself and the tracer concentration in the vessels

feeding the tissue, generally referred to as *arterial input function* (AIF). Therefore, it should be possible to derive tissue hemodynamics from the tissue and arterial plasma concentration-time curves. The link between those quantities is provided by the theory of tracer kinetics, which is valid for linear and stationary tissues [68]. A tissue is considered linear, if the response of the tissue is proportional to contrast agent dose; it is considered stationary, if the tissue response is independent of the time of injection. This implies the assumption, that the hemodynamic parameters of the tissue remain constant during the measurement.

For linear and stationary tissues, the theory of tracer kinetics relates the concentrations in arterial blood plasma[1] and tissue $c_a(t), c_t(t)$ by convolution with a residual function $R(t)$:

$$c_t(t) = F_P \cdot R(t) \otimes c_a(t) \tag{5.1}$$

In this equation, $\otimes$ denotes convolution, F_P is the flow of blood plasma into the tissue and $R(t)$ is the *tissue residue function*.

$R(t)$ describes the fraction of tracer that is present in the tissue at any given time $t > 0$ after an ideal, instantaneous contrast agent administration. Hence, a residue function is always positive, monotonously decreasing and $R(0) = 1$.

The product $F_P \cdot R(t)$ is called *tissue response function* or *impulse response function* (IRF). It describes the response of the tissue to an ideal, instantaneous arterial input function ("impulse") and contains all hemodynamic properties of the tissue. Quantification of hemodynamics thus boils down to the determination of $F_P \cdot R(t)$ from the concentrations measured in arterial blood and tissue.

Two classes of methods exist for this purpose: the model-free approach makes no assumptions about the form of the residue function and aims to determine $R(t)$ numerically from the measured arterial and tissue concentrations. This approach is described in section 5.1. Section 5.2 deals with the model-based approach, which assumes a certain mathematical structure of the residue function; the form of the residue function is derived from assumptions about the physiology of the tissue. Thus, model-based approaches are less general than the deconvolution approaches, but promise, through inclusion of this *a priori* knowledge, to yield more information and more independent parameters than model-free methods.

1 In MRI, the concentration in arterial plasma is usually derived from the signal intensity in an artery supplying the tissue. This yields the concentration in arterial *blood*, from which the plasma concentration can be obtained by scaling with the hematocrit *hct*: $c_{a,p} = c_a/(1 - hct)$.

5.1 DECONVOLUTION ANALYSIS

Model-free approaches applied to measured data $c_t(t)$, $c_a(t)$ produce the impulse response function $F_P \cdot R(t)$ directly with a procedure called *deconvolution* [69–73].

From the IRF, two important microcirculatory parameters describing the hemodynamic properties of the tissue can be derived. The plasma flow F_P to the tissue can be determined as the maximum of the IRF, since $R(t = 0) = 1$. Furthermore, the mean transit time (MTT) of the tissue equals the area under $R(t)$. From these quantities, the volume of distribution v_D can be derived by the *central volume theorem* as $v_D = F_P \cdot MTT$. The volume of distribution is the entire volume that is accessible for the tracer: If the tracer is confined to the vasculature, such as in healthy brain tissue, v_D equals the plasma volume, if however the tracer can extravasate, such as in brain tumors or inflammatory lesions, v_D represents the entire extravascular, extracellular volume.

The deconvolution itself, i. e. the determination of the impulse response function from the measured concentrations, is an ill-posed problem, which means that some kind of regularization is necessary in order to suppress unphysical solutions. A large number of regularization methods is available, one of the more popular approaches is *truncated singular value decomposition* [69, 70], an alternative regularization procedure is *standard form Tikhonov regularization* (see e. g. [71]). Both of these procedures require the determination of an optimal value of a regularization parameter, so that an appropriate compromise between suppression of unphysical oscillations and minimal bias of the solution is maintained. A regularization parameter that is chosen too small will lead to unphysical solutions with high-frequency oscillations with a large amplitude, a regularization parameter that is chosen too large will suppress details and produce a solution with too much dampening [73]. Unfortunately, the optimal value of the regularization parameter is not necessarily constant for all pixel curves in a measurement, but depends on physiological as well as measurement variables, such as the contrast-to-noise ratio; hence, it might be necessary to determine the optimal value of the regularization parameter for each single curve. For this purpose, a range of methods is available, two of which are *generalized cross validation* and an *optimized L-curve-criterion*, for details, the reader is referred to e. g. [73].

As an example, Fig. 14 shows the results of an deconvolution analysis of the same data as in Fig. 13, the corresponding arterial input function and the residue function that in this case was determined with an optimized L-curve-criterion. The bold line that approximates the measured curve shows the convolution of the determined residue function with the arterial input function.

It is well known that the results of a deconvolution analysis are quite sensitive to noise in the data (see e. g. [4] for a simulation study), in particular, the plasma flow F_P tends to be increasingly underestimated with increasing noise in the data. In the context of cerebral perfusion measurements, this sensitivity to noise is a minor concern if large signal changes occur, such as in T_2^*-weighted perfusion measurements. In T_1-weighted perfusion imaging however, the signal changes and hence the available contrast-to-noise ratio are much smaller due to the low cerebral blood volume, so that additional constraints may need to be imposed on the form of the residue function to facilitate reliable quantification of perfusion. In [47], the residue function is constructed from a set of polynomials, thereby decreasing the number of degrees of freedom in the solution and thus increasing the stability of the solution. The number of degrees of freedom can be reduced to an absolute minimum by a different strategy, which is presented in the following section.

5.2 TWO-COMPARTMENT MODELS

In contrast to the model-free deconvolution approach, so-called *compartment models* assume a certain internal structure of the tissue of interest. Specifically, tissue is assumed to be composed of one or more compartments; a compartment is defined as a space in which the contrast agent is distributed instantly and uniformly ("well-mixed"). A more general definition of a compartment is that the flux of contrast agent $J_{\text{out},i}(t)$ out of the compartment through a specific outlet i is proportional to the concentration $c(t)$ in the compartment:

$$J_{\text{out},i}(t) = F_i c(t) \tag{5.2}$$

The proportionality constant F_i is referred to as the clearance or transfer rate. If the tracer is transported through the outlet by convection, the clearance equals the flow through the outlet [46, 68]. In the context of DCE MRI, typical examples for compartments are the blood plasma or the extracellular, extravascular space.

To model a tissue that is composed of several compartments, it is necessary to identify the compartments as well as the respective in- and outlets of each compartment. With the definition of a compartment (5.2) and conservation of mass in each compartment, a set of first order differential equations can be built that describes the time-dependent concentrations in each compartment. The residual function that solves such a system with n compartments is always a sum of n exponentials [46].

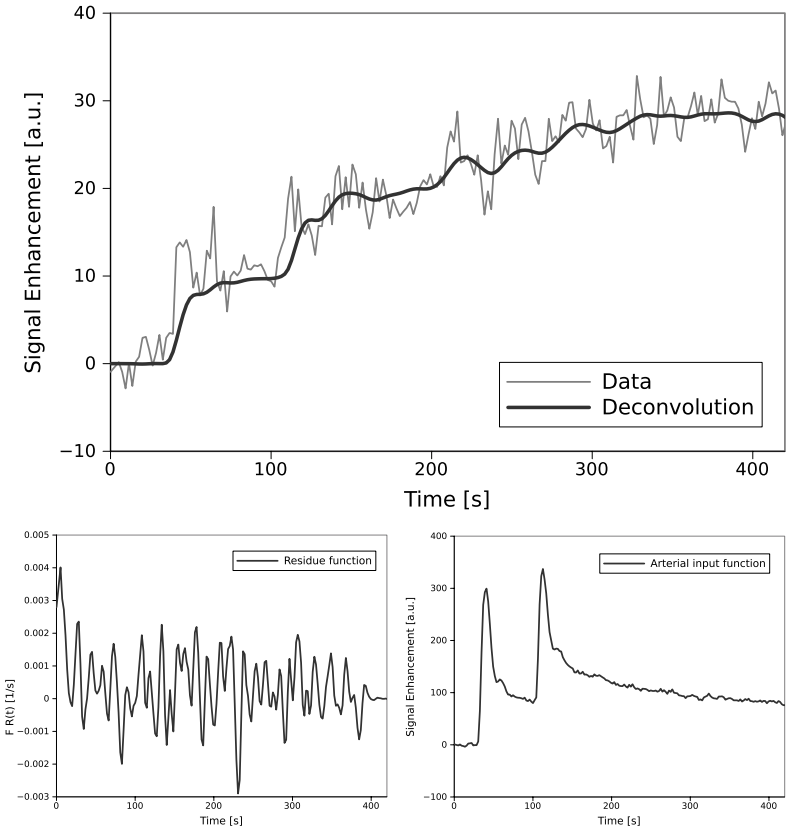

Figure 14: This figure shows the same data as Fig. 13 along with a "fit" to the original data, calculated with Tikhonov-regularized deconvolution (top). Estimated parameters were (after correction for partial volume effects in the AIF) $F_P = 9.5\,\mathrm{ml/100ml/min}$ and $v_D = 14\,\mathrm{ml/100ml}$. The calculated residual function $F_P R(t)$ is shown on the bottom left, the convolution of this residual function with the arterial input function (bottom right) produces approximates the measured curve.

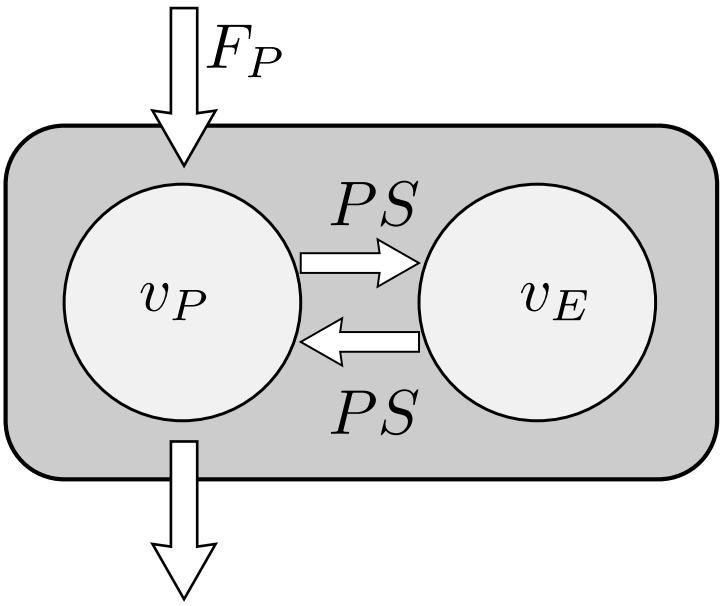

Figure 15: Illustration of the two-compartment exchange model. Tracer is transported with the plasma flow F_P into the vascular compartment with volume v_P. From there, it is either removed from the system via the venous outflow, or it is transported with the permeability surface area product PS into the extravascular, extracellular (i. e. interstitial) volume v_E, from whence it will eventually flow back into the vascular compartment.

5.2.1 *Two-compartment exchange model*

The two-compartment exchange (2CX) model is applicable for most tissues where the tracer can access the blood plasma and the extravascular, extracellular (interstitial) space. The model was introduced for tumors in [34] and is illustrated in Fig. 15. It is defined by the following assumptions:

A. Both the blood plasma space P and the interstitial space E can be described as compartments, i. e. Eq. (5.2) holds.

B. The interstitial compartment exchanges tracer only with the plasma compartment.

C. The clearance from P to E and the clearance from E to P are equal.

D. The clearance from P out of the system equals the plasma flow into P.

With the above mentioned assumptions, the differential equations defining the model can be written as [45, 46, 49]:

$$\begin{aligned} v_P \frac{dC_P}{dt} &= -PS(C_P - C_E) + F_P(C_{P,A} - C_P) \\ v_E \frac{dC_E}{dt} &= +PS(C_P - C_E) \end{aligned} \tag{5.3}$$

where C_E, C_P and $C_{P,A}$ denote the tracer concentrations in the interstitial volume, the plasma volume and the arterial plasma volume, respectively. v_P and v_E are the relative volumes of the plasma and interstitial compartments, F_P is the arterial plasma flow and PS, the *permeability surface area product*, is the flow from the plasma compartment over the vessel wall into the interstitial compartment and back. It is immediately clear from Eqs. (5.3) that the 2CX model is fully defined by four parameters.

The solutions for C_P and C_E can then be written as the convolution of the arterial plasma concentration $C_{P,A}$ with the accordant *residue function* $F_P \cdot R_P(t)$ or $F_P \cdot R_E(t)$, respectively:

$$\begin{aligned} R_P(t) &= e^{-tK_+} + T_B K_- E_-(e^{-tK_-} - e^{-tK_+}) \\ R_E(t) &= (1 - T_B K_-)E_-(e^{-tK_-} - e^{-tK_+}) \end{aligned} \tag{5.4}$$

The parameters K_+, K_-, E_- are given by:

$$K_\pm = \frac{1}{2}\left(T_P^{-1} + T_E^{-1} \pm \sqrt{(T_P^{-1} + T_E^{-1})^2 - 4T_E^{-1}T_B^{-1}}\right) \tag{5.5}$$

$$E_- = \frac{K_+ - T_B^{-1}}{K_+ - K_-} \tag{5.6}$$

In this notation, the two compartment exchange model is fully defined by the four parameters $\{F_P, T_B, T_E, T_P\}$, with T_B being the mean transit time of a hypothetical intravascular tracer and T_E, T_P the mean transit times in the interstitial and vascular compartment, respectively. These transit times are related to the four parameters defining the model by

$$T_P = \frac{v_P}{PS + F_P} \qquad T_E = \frac{v_E}{PS} \qquad T_B = \frac{v_P}{F_P} \tag{5.7}$$

The inverse transformation is given by [45]:

$$PS = F_P\left(\frac{T_B}{T_P} - 1\right) \qquad v_E = PS \cdot T_E \qquad v_P = F_P T_B \tag{5.8}$$

Hence, the total tissue concentration $C_t(t) = v_P C_P(t) + v_E C_E(t)$ can be written as convolution of the arterial plasma concentration

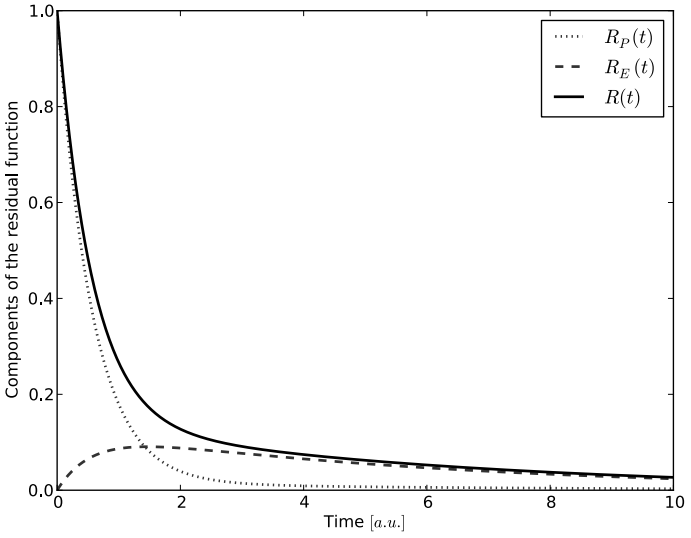

Figure 16: Components of the residual function of the 2CX model; for clarity, parameters have been arbitrarily adjusted.

with a biexponential total residue function $R(t) = R_P(t) + R_E(t)$:

$$C_t(t) = F_P \cdot \left[e^{-tK_+} + E_-(e^{-tK_-} - e^{-tK_+}) \right] \otimes C_a(t) \tag{5.9}$$

The residue functions for the plasma and interstitial compartments $R_P(t), R_E(t)$ are shown in Fig. 16, along with the total residue function. It should be noted that the residual function for the interstitial compartment $R_E(t)$ does not fulfill the properties of residue functions stated above. In particular, $R_E(0)$ is zero, and only starts decreasing after having reached a peak at $t > 0$. This observation does not violate the principles of tracer kinetics, since the residual function for the whole tissue fulfills the expected properties; instead, it reflects the fact that the tracer arrives in the vascular compartment first and only then can reach the interstitial compartment.

SPECIAL CASES OF THE 2CX MODEL In several imaginable situations, the measured data $c_t(t)$, $c_a(t)$ might not contain enough information for a reliable estimation of all four parameters of the 2CX model, so that the full 2CX model is underdetermined. In these situations, it may be helpful to introduce additional assumptions that reduce the number of free parameters.

The 2CX model is underdetermined in the following scenarios:

1. The tracer extravasates slowly, so that the interstitial concentration remains small during the acquisition time.

2. The tracer extravasates rapidly, so that the intra- and extravascular compartments appear as one well-mixed compartment.

3. The intravascular concentration cannot be distinguished from the arterial concentration. This can occur if (i) the plasma flow is large or if (ii) the temporal resolution and the contrast-to-noise ratio (CNR) of the measurement are not sufficient.

In these situations, the four-parameter 2CX model is underdetermined so that not all four parameters can be determined reliably. This underdetermination can be handled by modifying the model equations (5.3) and incorporating additional assumptions. Essentially, these modifications reduce the bi-exponential residue function in (5.9) to a mono-exponential residue function, thereby removing interpretation difficulties.

5.2.2 *Two-compartment uptake model*

Under the assumption that the interstitial concentration remains much smaller than the plasma concentration ($C_E \ll C_P$), the model equations (5.3) reduce to:

$$\begin{aligned} v_P \frac{dC_P}{dt} &= -PS \cdot C_P + F_P \left(C_{P,A} - C_P\right) \\ v_E \frac{dC_E}{dt} &= +PS \cdot C_P \end{aligned} \tag{5.10}$$

These equations define the *two-compartment uptake model* (2CU) [49, 74]. The solution of (5.10) yields the partial residue functions of the uptake model as

$$\begin{aligned} R_P(t) &= e^{-t/T_P} \\ R_E(t) &= E(1 - e^{-t/T_P}) \end{aligned} \tag{5.11}$$

with the *extraction fraction*

$$E = \frac{PS}{PS + F_P} \tag{5.12}$$

The total residual function of the uptake model is then the mono-exponential

$$R(t) = e^{-t/T_P} + E(1 - e^{-t/T_P}) \tag{5.13}$$

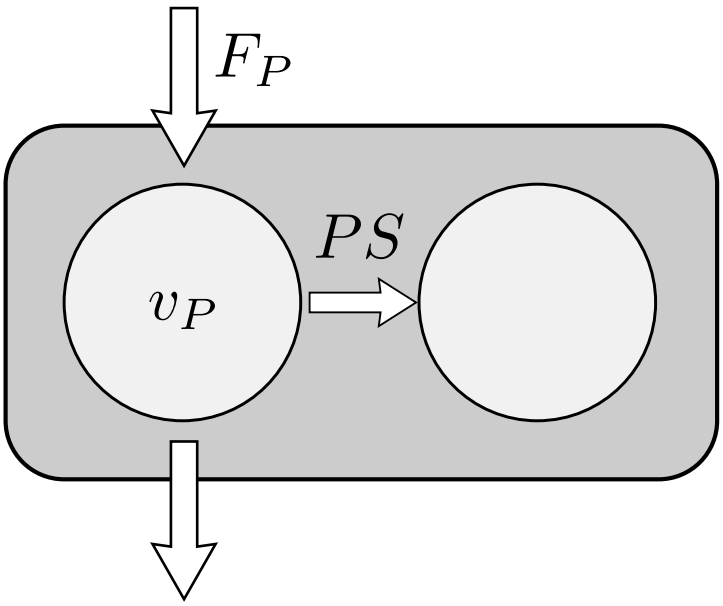

Figure 17: The two-compartment uptake model, characterized by the assumption of small tracer concentration in the interstitial space, so that no tracer flows back from the interstitium into the plasma space. This has the consequence that the interstitial volume v_E cannot be measured.

From the three parameters F_P, T_P, E that fully define the uptake model, the plasma volume v_P and the permeability surface area product PS can be derived as

$$PS = \frac{EF_P}{1-E} \qquad v_P = \frac{T_P F_P}{1-E} \tag{5.14}$$

We refer to this model with the term *uptake model*, since it is able to describe extravasation of the tracer into the interstitium, but not its washout. This behaviour is reflected in the interstitial residue function $R_E(t)$ (5.11), which does not return to zero, but instead reaches a constant, positive value, hence describing a fraction of the tracer remaining in the interstitial compartment (*uptake*). The assumption of small interstitial concentration C_E holds true not only if the extravasation of contrast agent is very small, but also, if the total acquisition time of a bolus tracking experiment is so short that C_E never reaches high values. In such a situation, the 2CX model would be underdetermined and fitting the 2CX model to such data would result in parameter estimates with poor precision.

As a corollary, we note that the uptake model obviates the need for even simpler models [75] for situations in which the tracer is distributed in a single compartment only. This is the case e. g. in a scenario, where the flow of the tracer between the intravascular and interstitial compartment is comparable to or larger than

the plasma flow into the intravascular compartment, so that the tissue appears as a single, well-mixed compartment with the volume of distribution $v_D = v_P + v_E$. Describing such a tissue with the uptake model yields the plasma flow F_P, the volume of distribution v_D and a permeability surface area product $PS = 0$.

A similar situation occurs if the tracer is confined to the intravascular compartment, e. g. in healthy brain tissue, where the blood brain barrier effectively impedes the passage of the tracer across the capillary walls, or if an intravascular tracer is used. Likewise, this scenario can be described by the uptake model with a permeability surface area product $PS = 0$. In this case, the volume obtained with the uptake model is the plasma volume v_P.

Without additional assumptions about the tissue structure, it is, however, impossible to decide whether the volume that the uptake model yields is the plasma volume v_P alone or the entire extracellular volume $v_D = v_P + v_E$.

5.2.3 *Two-compartment Tofts model*

For tissues with negligible amounts of intravascular contrast agent, the widely used *Tofts model* [76, 77] has been developed. The residue function of this model is the mono-exponential

$$R(t) = K^{trans} e^{-tk_{ep}} \tag{5.15}$$

where the model parameters K^{trans} and k_{ep} are related to the interstitial volume v_E, the plasma flow F_P and the extraction fraction E via

$$K^{trans} = EF_P \qquad\qquad k_{ep} = EF_P/v_E \tag{5.16}$$

The extraction fraction E measures the amount of tracer that is extracted from the capillary bed, it is related both to the plasma flow F_P and the permeability surface area product PS. Since these quantities are not measurable separately with the Tofts model, the term K^{trans} is introduced. In this form, the Tofts model is a two-parameter model.

The assumption of negligible intravascular concentrations does not hold in a wide range of tissues; tumors in particular are often strongly vascularized. To facilitate the use of the Tofts model in such a tissue, the original Tofts model has been extended by adding a vascular term to the residue function

$$R(t) = v_P \delta(t) + K^{trans} e^{-tk_{ep}} \tag{5.17}$$

Here, v_P denotes the plasma volume and $\delta(t)$ is a Dirac delta function. This three-parameter model is usually referred to with

the term *extended* or *modified* Tofts model [75, 77, 78] and has seen widespread use. For the sake of consistency, we abbreviate the modified Tofts model as 2CT in this thesis, since the modified Tofts model can be seen as a special case of the 2CX model. For this reason, it may be inappropriate under certain conditions to use the 2CT model instead of the 2CX model. This has been observed both in experimental data [65] as well as in simulation studies [79, 80]. In a recent study [81], Sourbron and Buckley showed that the 2CT model is valid only in the regime of vanishing intravascular volume $v_P \to 0$ and high plasma flow $F_P \to \infty$, i. e. in tissue that is at the same time weakly vascularized and highly perfused. If this is the case, the 2CT model is a special case of the 2CX model and K^{trans} can be interpreted as PS. In reality, the conditions of infinite plasma flow or vanishing plasma volume are seldom fulfilled, but in the context of DCE MRI, they can be relaxed since the measured concentrations are i) sampled at discrete time points and ii) suffer from noise in the data. Consequently, the 2CT model may still be the appropriate model, if e. g. the plasma flow is high, and either the temporal resolution or the contrast-to-noise ratio in the data is insufficiently low to estimate the plasma flow.

Part II

DEVELOPMENTS AND APPLICATIONS

6 METHODOLOGICAL DEVELOPMENTS

After the overview about quantification of hemodynamics with DCE MRI that was presented in the first part of this work, this first chapter of the second part presents new methodological developments for the evaluation and absolute quantification of hemodynamic parameters in the brain with DCE MRI. Applications of these technical developments in two patient studies are presented in the two following chapters.

In this chapter, a robust method for automated model selection is introduced and evaluated in a simulation study (section 6.1). Section 6.2 is concerned with details of model fitting and implementation issues; section 6.3 discusses the issue of measuring tracer concentrations in arteries.

6.1 MODEL SELECTION

We have seen in section 5.2 that the most general two-compartment model is the 2CX model. However, the use of the 2CX model may be inadequate for data analysis if the structure of the data does not support the reliable estimation of all four parameters defining the 2CX model. In these cases, it is advisable to use either the 2CU or the 2CT model to remove parameter redundancies and to increase the precision of the parameter estimates.

Conversely, an insufficient model that is not able to describe all important features of the data will produce parameter estimates with a large bias.

Hence, a central issue in modelling DCE data is to select a model that is complex enough to describe all features in the data and not too complex to avoid parameter redundancy and thus meaningless estimates [75]. In general, models with too few parameters are not able to fit to the data and lead to bad fits and thus biased parameter estimates. Conversely, models with too many free parameters yield estimates with low precision [82].

However, it is not clear beforehand which model should be chosen for a particular curve. The choice of the model is complicated by the fact that the choice of the most appropriate model is not only affected by measurement parameters such as temporal resolution, total acquisition time or CNR that are easily assessable, but also by the hemodynamic properties of the tissue itself.

Fig. 18 and Table 1 illustrate the problem of model selection. The curve shown in the figure was measured in a white matter lesion in a patient with Multiple Sclerosis. The 2CX and 2CU

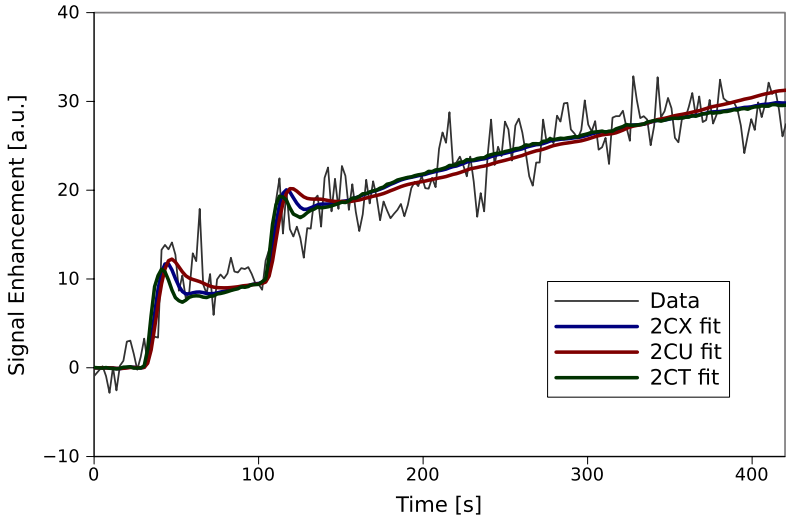

Figure 18: Fits of the 2CX, 2CU and 2CT models to the same data as in Figs. 13 and 14. The resulting parameter estimates, χ^2-values and Akaike weights of each model are shown in Table 1.

Table 1: Parameters produced by the models in Fig. 18. F_P and PS are given in ml/100ml/min, v_P and v_E in %

MODEL	F_P	v_P	PS	v_E	χ^2	w_{AIC}
2CX	25.0	2.8	1.17	34.7	0.811	0.35
2CU	24.0	3.0	1.05	–	0.814	0.65
2CT	–	1.91	1.60	12.5	0.981	$0.5 \cdot 10^{-8}$

models yield almost identical model fits and rather similar parameter estimates and χ^2 values, whereas the 2CT model yields an inferior fit, which is also reflected by the higher χ^2 value.

Obviously, the 2CT model can be ruled out as the best model, but to determine whether the 2CX or the 2CU model yields the more reliable estimates is difficult. Based on the χ^2 value alone, the 2CX model seems to be slightly favoured, but this could be a consequence of the fact that it has one more free parameter (v_E) and can thus better adapt to the data. An expert user thus would probably choose the 2CU model as best model, since the marginal improvement in χ^2 and visual inspection of the fits as in [49] probably do not justify the additional free parameter introduced by the 2CX model.

Clearly, a more objective means of model selection would be desirable.

6.1.1 *The Akaike information criterion*

A promising and mathematically rigorous approach to deal with model selection is the *Akaike Information Criterion (AIC)* [82, 83]. Basically, the AIC penalizes the goodness of fit, which in general is higher for models with more parameters, with the number of free parameters of the model.

After a model has been fitted to given data, the AIC is easy to calculate [84]:

$$AIC = N \cdot \ln\left(\frac{SS}{N}\right) + 2(K+1) \tag{6.1}$$

where N is the number of measured data points, SS is the sum of squared residuals as a measure of the goodness of fit and K is the number of free parameters. For small ($N/K \lesssim 40$) sample sizes, the use of the corrected Akaike Information Criterion ($cAIC$) is advocated [84]:

$$cAIC = AIC + \frac{2(K+1)(K+2)}{N-K-2} \tag{6.2}$$

The absolute value of $cAIC$ itself has no meaning, however, among a set of models that has been fit to the same data, the model with the lowest $cAIC$ is considered to be the model that approximates the unknown truth best.

To further simplify the model selection in a set with M models, the *Akaike weights* w_i can be used:

$$w_i = \frac{exp(-\Delta_i/2)}{\sum_{r=1}^{M} exp(-\Delta_i/2)} \tag{6.3}$$

where

$$\Delta_i = cAIC_i - min(cAIC) \tag{6.4}$$

is the difference between each model's $cAIC$ and the minimal $cAIC$ in the set of models.

For each model i, the Akaike weight w_i gives the probability for the model to be model among the set that approximates the unknown truth best.

In the example above, the last column in Table 1 shows that the 2CU model has the highest probability to be the best model and should thus be regarded as the model that yields the most reliable parameter estimates.

6.1.2 *Multimodel inference*

Given an number of similar datasets, the designation of a *best model* using the process described above will often provide unsatisfactory results, as the *best model* will vary from dataset to dataset. Since not every model in a given set of models provides the same parameters, a comparison of parameter estimates is often complicated or even rendered impossible.

A possible solution to this dilemma might be model averaging [82, 85]. Given a set of M models, an estimate of parameter $\hat{X}_j$ is obtained by averaging over all models in which X_j appears:

$$\hat{X}_j = \frac{\sum_{i=1}^{M} w_i I_{i,j} X_{i,j}}{w_+(j)} \tag{6.5}$$

where $I_{i,j}$ is 1 if the parameter X_j appears in model i and zero otherwise and

$$w_+(j) = \sum_{i=1}^{M} w_i I_{i,j} \tag{6.6}$$

is the sum $w_+(j)$ of the Akaike weights over all models, in which parameter X_j appears. On a side note, $w_+(j)$ quantifies the relative importance of the parameter X_j for modeling the given data [82].

In [82] it is stated that model averaging might often reduce bias and increase precision of parameter estimates, compared to parameter estimates from a single (best) model. This hypothesis is obviously of particular interest in the context of perfusion quantification with the set of the three models 2CX, 2CT, 2CU. Moreover, the multimodel approach avoids the *a priori* selection of a particular model for a study, which might be inadequate at least for a subset of the data.

Hence, the multimodel inference approach might be particularly useful for the quantification of perfusion data, since similar data will always yield the same set of perfusion parameters, independent of the most probable model. However, further studies are needed to investigate and validate this quantification approach in the context of cerebral perfusion imaging.

In the remainder of this section, we investigate the applicability of a multimodel approach in perfusion quantification with a simulation study.

6.1.3 *Simulation study*

The potential of model selection to improve accuracy and precision of parameter estimates is difficult to evaluate with exper-

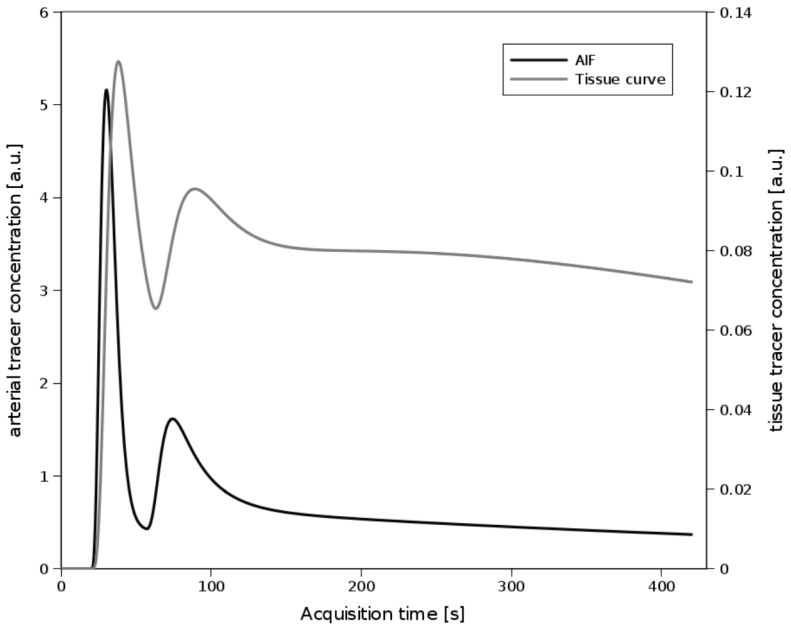

Figure 19: Synthetic arterial input function (dark gray) and 2CX tissue curve (light gray) that were used for the model selection simulations. Note the different scaling of the two curves.

imental, measured data, since no accepted non-invasive gold standard for the measurement of hemodynamic parameters is available. Moreover, it is not easy to verify if the assumptions underlying a given model, like the assumption of small interstitial concentrations or of negligible vascular transit time are satisfied or violated. Hence it is not straightforward to verify with experimental data whether an automatic model selection algorithm, e. g. with the Akaike information criterion, yields reliable results and improves parameter estimates.

This situation is entirely different in a simulation setting. By generating a tissue curve with a particular model, one has exact knowledge about the true hemodynamic parameters as well as about the true model. With a suitable simulation of the measurement process, a simulation study is thus an appropriate means to validate a range of hypotheses about automatic model selection.

A hypothesis that we investigated in a simulation study in [80] is that the 2CU model is the appropriate model if the interstitial concentration remains small. In this situation, the 2CU model should therefore be favoured over the 2CX model by the AIC. In a tissue that is described with the general 2CX model, the interstitial concentration is small if the total acquisition time is short, therefore, the AIC should favour the 2CU model for short acquisition times and suggest a transition to the true 2CX model for sufficiently long acquisition times.

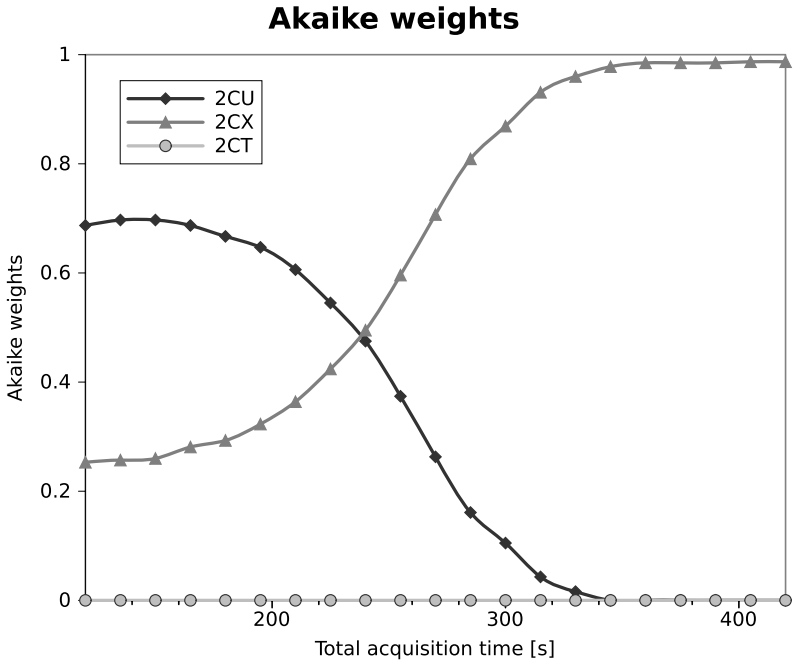

Figure 20: Median value of the Akaike weights for the 2CX, 2CU and 2CT models, in dependence of the total acquisition time; the AIC clearly suggests a transition from the 2CX to the 2CU model for acquisition times shorter than approximately 240 s (for these specific SNR and hemodynamic values)

6.1.3.1 *Methods*

DATA GENERATION To investigate this hypothesis, a synthetic arterial input function (AIF) was constructed by superposing gamma variate functions to simulate the first and second pass of the contrast agent. Using this AIF, we simulated a tissue curve with the 2CX model with parameters typical for brain tumors (F_P : 21.9 ml/100ml/min, v_P : 4.8 %, PS : 2.9 ml/100ml/min, v_E : 11.9 %), these values were taken from a subset of the data in chapter 7. To minimize errors by insufficient temporal sampling, data were generated with a high temporal resolution of 0.1 s, the simulated total acquisition time was 420 s.

SIMULATION OF MEASUREMENT To simulate the measurement process, the generated AIF and tissue curves were sampled with a fixed temporal resolution (TR) of 1.0 s and variable total acquisition times in the range from 120 s to 420 s, to avoid artificial oscillations, the start of each measurement was chosen randomly between $t = 0$ and $t = TR$. Normally distributed noise with a standard deviation of $\max(tissuecurve)/4$ was added to the tissue curve to produce a contrast to noise ratio $CNR = 4$, where CNR is defined as the ratio of maximal tissue concentration to standard deviation of noise.

QUANTIFICATION The 2CX, 2CU and 2CT models were fitted to the previously simulated tissue curve, AIC and the Akaike weights for each fit were calculated, and the parameter estimates of each model as well as the best model, according to the AIC, were recorded. To estimate the precision of parameter estimates of each approach, the process of simulated measurement and subsequent quantification was repeated 10.000 times for each acquisition time; median values and the 17th and 83rd percentiles of the estimates of each model as well as the best model as suggested by the AIC were calculated as measures of accuracy and precision.

6.1.3.2 *Results*

Figure 19 shows the synthetic arterial input function and the tissue curve that were used as input data. The median values of the Akaike weights, giving the probability of each model to be the *best* model, are shown in Fig. 20. For long acquisition times, the AIC clearly favours the 2CX model, for shorter acquisition times, the Akaike weight of the 2CU model increases, suggesting a transition to the 2CU model for acquisition times shorter than approximately 280 s. The 2CT model is rejected by the AIC over the whole range of acquisition times.

Estimates of plasma volume v_P and permeability surface area product PS of each model in dependence of the acquisition time are shown in Fig. 21. Both for v_P and for PS the 2CT model yields estimates with a large deviation of the true values. The 2CU model yields estimates with low variance for all acquisition times, producing, however, estimates with a large bias for long acquisition times. The 2CX model, on the other hand, produces estimates with low bias over the entire range of acquisition times; for short acquisition times, the variance of parameter estimates is large.

6.1.3.3 *Discussion*

In this simulation study, we have investigated the feasibility of model selection with the AIC. The results confirm our initial experience, that the 2CU model may be the model of choice if the interstitial contrast agent concentrations remains small due to short acquisition times. Moreover, our study shows that model selection correctly reflects this fact by suggesting a transition to the simpler 2CU model for short acquisition times. This result appears plausible, since data that were acquired during a shorter time span obviously contain less information, so that a reliable estimation of all underlying model parameters may not be possible.

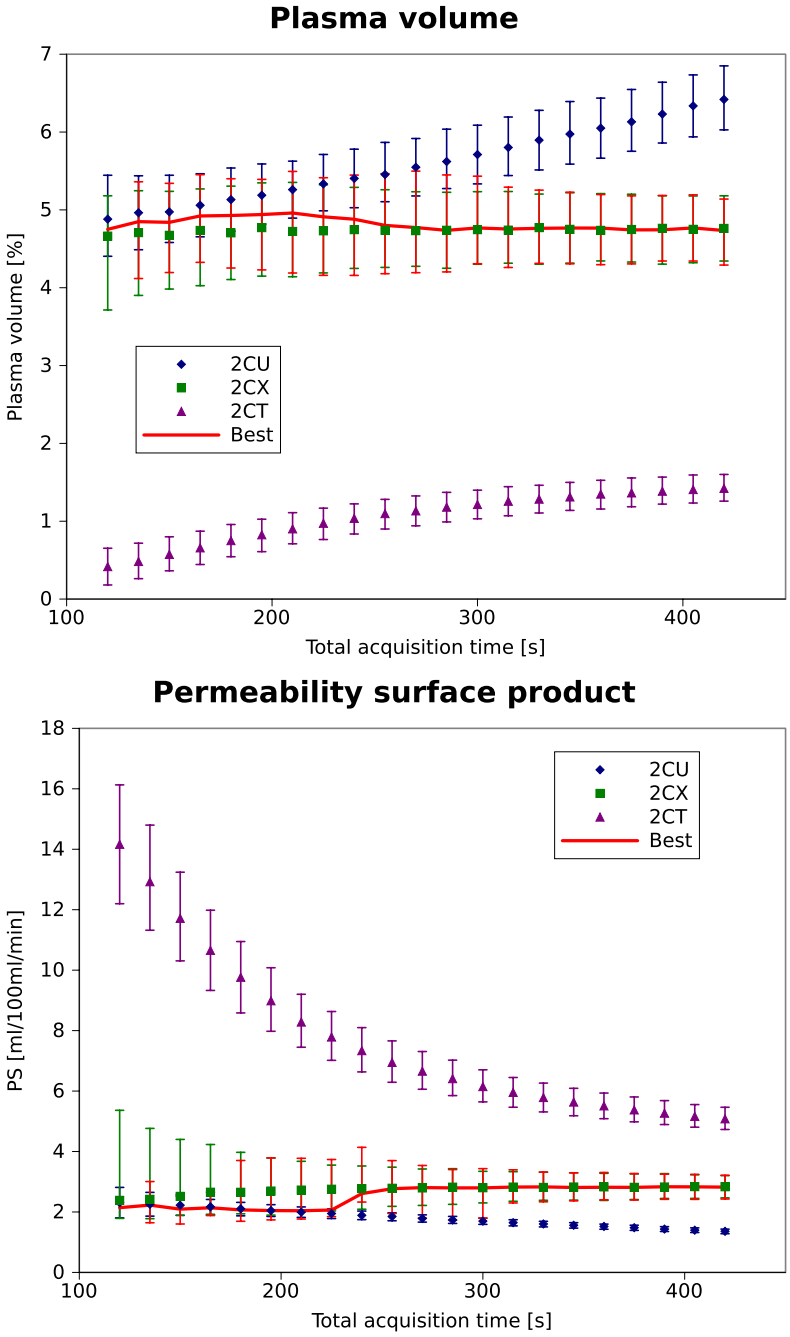

Figure 21: Estimates of plasma volume v_P (top) and permeability surface area product PS (bottom) of all models. True values were $v_P = 4.8\,\mathrm{ml/100ml}$ and $PS = 2.9\,\mathrm{ml/100ml/min}$

Moreover, the AIC rejects the 2CT model over the whole range of acquisition times. This rejection is fully justified, since the basic assumption of large plasma flow or, correspondingly, negligible plasma transit time, underlying this model is not met and thus further confirms the use of the AIC as a criterion for automatic model selection.

In this study, we have deliberately induced a situation with small interstitial contrast agent concentrations by subsequent shortening of the acquisition time. In reality, the total acquisition time is not the only parameter that influences the interstitial concentrations - if this were the case, one could simply measure long enough and thus obviate the need for model selection. Instead, the choice of the most appropriate model is not only influenced by measurement parameters that can be controlled in a wide range, such as the acquisition time, the temporal resolution or the signal-to-noise ratio, but also by physiological parameters such as the plasma flow, the plasma volume, the permeability surface area product and the interstitial volume that are not known *a priori* and beyond the control of the experiment. Consequently, this simulation study is by no means exhaustive, but elucidated only a small aspect of model selection.

Further studies may address the influence of physiological parameters on model selection; for instance, one could investigate, whether model selection reflects the observation in [81] that the 2CT model is the appropriate limit of the 2CX model for weakly vascularized and highly perfused tissue.

6.2 MODEL FITTING AND IMPLEMENTATION

To estimate model parameters from concentrations $c_a(t), c_t(t)$ measured in arterial blood and tissue, several approaches are feasible. The differential equations (5.3), (5.10) defining the model can be solved directly e. g. with a Kutta-Merson algorithm as in [85], or they can be solved analytically. A widely used approach for the estimation of model parameters from measured concentrations $c_a(t), c_t(t)$ is non-linear least squares fitting [86, 87]. Here, a set of initial parameters and the arterial concentration are used to calculate the right-hand side of equation (5.1). Subsequently, the outcome of this calculation is compared to the measured tissue concentration using an appropriate estimator, usually the sum of squared residuals. In subsequent steps, the initial parameters are adapted iteratively, until the difference between the calculated and measured tissue concentrations is minimized or satisfies another appropriate stopping criterion.

6.2.1 *Discrete convolution*

Calculating the tissue concentrations using a model with a mono- or biexponential residue function frequently requires the numerical calculation of the convolution of an exponential with a discrete function. An iterative formulation of this time-consuming operation is described below.

The convolution of two functions $f(t), g(t)$ which are defined for positive values of t, is defined as

$$(f \otimes g)(t) = \int_0^\infty f(t-\tau)g(\tau)d\tau \tag{6.7}$$

In the context of model fitting, one of these functions is often provided as a discrete function $c_a(t_i)$, measured at time points $t_i, i \in [0, n]$ spaced equidistantly with the distance Δt, while the other function is an exponential $e^{-\lambda t}$. With the abbreviations

$$\Delta t = t_{i+1} - t_i \tag{6.8}$$

$$m = \frac{c_a(t_{i+1}) - c_a(t_i)}{\Delta t} \tag{6.9}$$

the linear interpolation of $c_a(\tau)$ becomes

$$c_a(\tau) = c_a(t_i) + m \cdot (\tau - t_i) \tag{6.10}$$

and the convolution then has the form

$$Y(t_i) = \int_{t_0}^{t_i} d\tau c_a(\tau) e^{-\lambda(t_i - \tau)} \tag{6.11}$$

If $Y(t_i)$ is given, $Y(t_{i+1})$ can be calculated as:

$$\begin{aligned} Y(t_{i+1}) &= \int_{t_0}^{t_i+1} d\tau c_a(\tau) e^{-(t_{i+1}-\tau)\lambda} \\ &= \int_{t_0}^{t_i} d\tau c_a(\tau) e^{-(\dots)} + \int_{t_i}^{t_{i+1}} d\tau c_a(\tau) e^{-(\dots)} \\ &= \int_{t_0}^{t_i} d\tau c_a(\tau) e^{\lambda\tau} e^{-(t_i - t_i + t_{i+1})\lambda} + \int_{t_i}^{t_{i+1}} d\tau c_a(\tau) e^{-(\dots)} \\ &= \int_{t_0}^{t_i} d\tau c_a(\tau) e^{-(t_i-\tau)\lambda} e^{-(t_{i+1}-t_i)\lambda} + \int_{t_i}^{t_{i+1}} d\tau c_a(\tau) e^{-(\dots)} \\ &= e^{-(t_{i+1}-t_i)\lambda} \cdot Y(t_i) + \int_{t_i}^{t_{i+1}} d\tau c_a(\tau) e^{-(t_{i+1}-\tau)\lambda} \end{aligned} \tag{6.12}$$

With this iterative formula, the discrete convolution (6.11) can be calculated from the starting point $Y(t_0) = 0$ if the last integral, further denoted by I, in eq. (6.12) can be determined. With Eqs. (6.8) and (6.10), I can be calculated easily as

$$\begin{aligned} I &= e^{-t_{i+1}\lambda} \left\{ \int_{t_i}^{t_{i+1}} d\tau (c_a(t_i) - m t_i) e^{\tau\lambda} + \int_{t_i}^{t_{i+1}} d\tau m \tau e^{\tau\lambda} \right\} \\ &= \frac{c_a(t_i) - m t_i}{\lambda} (1 - e^{-\lambda\Delta t}) + \frac{m}{\lambda^2} \left[(\lambda t_{i+1} - 1) - e^{-\lambda\Delta t} (\lambda t_i - 1) \right] \end{aligned} \tag{6.13}$$

Thus, to calculate the convolution of an exponential with a discretely sampled function $c_a(t_i)$, we can use the following iterative formula:

$$Y(t_0) = 0 \tag{6.14}$$

$$\begin{aligned} Y(t_{i+1}) &= e^{-\lambda\Delta t} Y(t_i) \\ &\quad + \frac{c_a(t_i) - m t_i}{\lambda} (1 - e^{-\lambda\Delta t}) \\ &\quad + \frac{m}{\lambda^2} \left[(\lambda t_{i+1} - 1) - e^{-\lambda\Delta t} (\lambda t_i - 1) \right] \end{aligned} \tag{6.15}$$

A basic implementation of this algorithm in the popular open source language Python might look like this:

```
def convolution_w_exp(time, aif, tau):
    """
    returns the convolution of aif with an exponential
    with time constant lam=1/tau.
```

```
        """
        lam=1./tau
        y=zeros_like(aif)

        t=time
        x=aif
        for i in range(1,len(y)):
            dt=t[i]-t[i-1]
            edt=exp(-lam*dt)
            m=(x[i]-x[i-1])/dt
            y[i]=edt*y[i-1]
            +(x[i-1]-m*t[i-1])/lam*(1-edt)
            +m/lam/lam*((lam*t[i]-1)-edt*(lam*t[i-1]-1))
        return y
```

This code obviously is not optimized for speed and relies on proper calling from the fit algorithm, since it does not perform any input checking. If the code is used in this form, it is imperative that the fit algorithm is constrained to use only non-zero values of τ – if it is called with $\tau = 0$, it will instantly crash.

6.2.2 *The multimodel interface in PMI*

In the course of this work, automatic model selection has been used both in studies with measured and with simulated data. The analysis of measured data has been performed with our own, in-house written software PMI 0.3 and 0.4 [88], written in IDL. To facilitate straightforward evaluation of multiple models and the selection of the most appropriate model in PMI with measured data, a plugin for PMI was developed that allows the fitting of a range of models to given data. Fig. 22 shows a screenshot of this multimodel interface, with data from a contrast-enhancing MS lesion.

Model fitting with this interface requires that the data has been imported into PMI and an arterial as well as a tissue region have been defined. For partial volume correction of the AIF (see 6.3), a venous region is required as well. Once this is accomplished, the multimodel interface can be started. The first step in quantification is the selection of arterial and tissue regions with the corresponding drop-down menues. For the determination of the AIF, the length of the baseline and the hematocrit need to be provided. If the AIF is to be corrected for partial volume effects, the apparent plasma volume in a large vein can be provided.

In the next step, the method for the approximation of contrast agent concentration needs to be selected, various fit options (delay between arterial and tissue curve, parameter constraints) can be checked as well.

After these preprocessing steps, the model that is to be fitted can be chosen; the model menue includes 2CX, 2CU, 2CT and

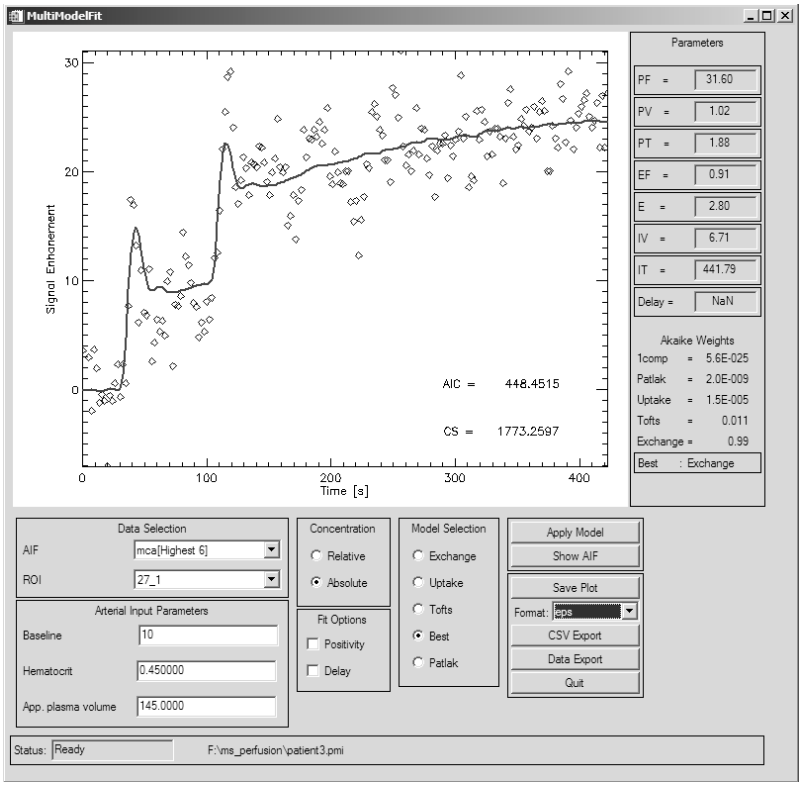

Figure 22: Screenshot of the multimodel interface in PMI

simpler models (see Fig. 22), as well as an option *best model*. If *best model* is selected, all models are fitted to the data, and the Akaike weights are determined.

After a successful fit, the tissue concentration curve is displayed along with the model fit, on the right hand side of the window, the parameter estimates are shown. The parameter estimates as well as the data (i. e. time axis, arterial input function, tissue curve and model fit) can be exported as a .csv file, allowing further processing e. g. in spreadsheet software.

6.3 MEASUREMENT OF THE ARTERIAL INPUT FUNCTION

A quantitative measurement of perfusion requires not only the concentration-time course in tissue, but also the concentration-time course in an artery supplying the tissue, commonly called the *arterial input function* (AIF) (see Ch. 5). Although the determination of the AIF is generally much simpler in DCE MRI than in DSC MRI, care must be taken to avoid errors that would directly enter into the quantification.

INFLOW EFFECTS A common problem with the measurement of the AIF is that flowing spins, carried to the imaging slice or slab by arterial blood, have not yet reached a steady state when

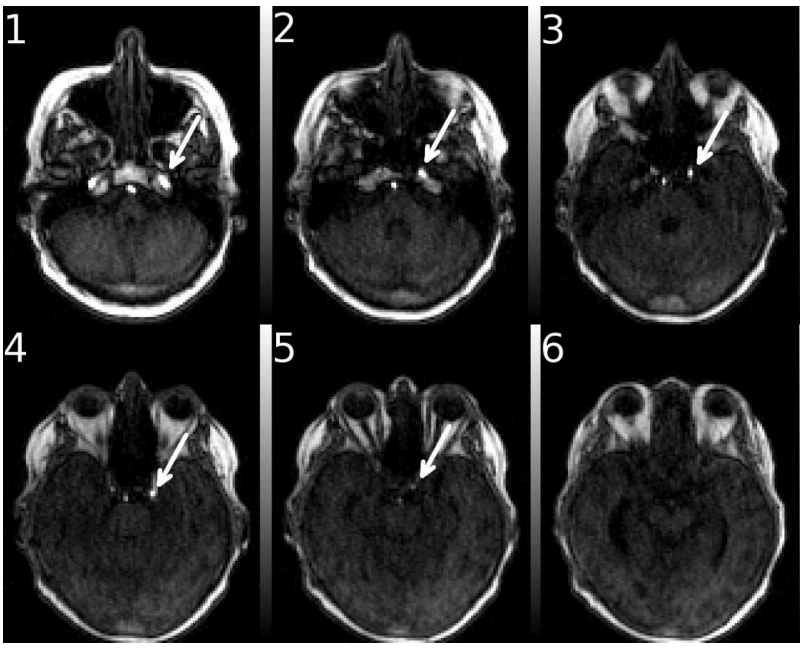

Figure 23: Axial slices from caudal (1) to cranial (6), taken from a 3D perfusion measurement before the arrival of contrast agent. Note the gradually decreasing signal intensity in the internal carotid arteries (arrows) that can be attributed to the inflow effect, which completely vanishes in the most cranial slice

they arrive at the site where the AIF is measured. This results in a large signal enhancement of the arterial lumen; larger vessels that suffer from inflow effects appear bright in T_1-weighted images even if no contrast agent is present. This is demonstrated in Fig. 23.

The amount of inflow effects depends on the number of excitation pulses that the spins experienced (and thus the speed with which the flow into the imaging slice or slab occurs) as well as on sequence parameters like the flip angle and repetition time ([29], Ch. 24). The increased signal that arises due to flowing blood mimics the effects of higher relaxation rate R_{10}, hence, the measurement of the arterial contrast agent concentration is severely compromised in the presence of inflow effects.

The inflow effect is smaller when smaller flip angles are employed, this, in combination with non-selective inversion or saturation pulses is the common strategy to minimize inflow effects with 2D acquisitions [43].

When a 3D acquisition is used, the imaging slab usually can be positioned in such a way, that inflowing spins in a major artery travel a sufficient distance in the slab so that they have reached a steady state when they arrive at the site where the AIF is measured. This is illustrated in Fig. 23, here, the AIF was

measured not in the carotid arteries, but in the middle cerebral artery.

PARTIAL VOLUME EFFECTS Another problem can arise when only arteries with a diameter of the order of the spatial resolution of the measurement are available for an AIF measurement. In this case, the arterial signal is most likely underestimated through the contributions of the vessel wall or surrounding tissue. With the assumption that the amount of tracer in the tissue causing the partial volume effect is negligible compared to the amount of tracer in the arterial lumen, the measured arterial input function $c_a^m(t)$ is then simply $p \cdot c_a(t)$, with $0 < p \leq 1$.

Since quantification of hemodynamics relies on the basic equation of tracer kinetics (5.1), the underestimation of the AIF due to partial volume effects would lead to overestimation of the hemodynamic parameters and hence needs to be corrected for.

The value of p can be determined with a reference measurement in a large vessel [49], where a voxel can be found that is completely embedded in the vessel and thus contains only blood and does not suffer from partial volume effects. In the brain, candidate vessels for this purpose are the large veins like the sinus sagittalis. The assumption underlying the partial volume correction is that the venous concentration-time course $c_v(t)$ can be written as the convolution of the measured arterial concentration with a probability density function $H(t)$ [89]:

$$c_v(t) = H(t) \otimes c_a(t) = p \cdot H(t) \otimes c_a^m(t) \tag{6.16}$$

If $c_a^m(t)$ and $c_v(t)$ have been measured, the impulse response function $IRF = p \cdot H(t)$ can be determined without additional assumptions by numerically deconvolving $c_v(t)$ with $c_a^m(t)$ with an appropriate regularization algorithm like generalized cross-validation [73]. Since $H(t)$ is a probability distribution, the time integral of $H(t)$ equals 1, so that p can easily be obtained from the time integral of $p \cdot H(t)$[1]:

$$\int IRF dt = \int p \cdot H(t) dt = p \int H(t) dt = p \tag{6.17}$$

This approach for partial volume correction is demonstrated in Fig. 24 for a patient from the study presented in Chapter 7.

Both studies presented in the following two chapters used this method for partial volume correction, yielding values of p in the

1 This is mathematically equivalent to the determination of the blood volume in the vein by deconvolution. Since the arterial concentration is underestimated, the apparent venous blood volume $v_{b,v}^{app}$ will be estimated higher than 100 ml/100ml. Since the blood volume in the venous voxel is assumed to be $v_{b,v} = 100$ ml/100ml, the partial volume correction factor can be determined as $p = v_{b,v}^{app} / v_{b,v}$.

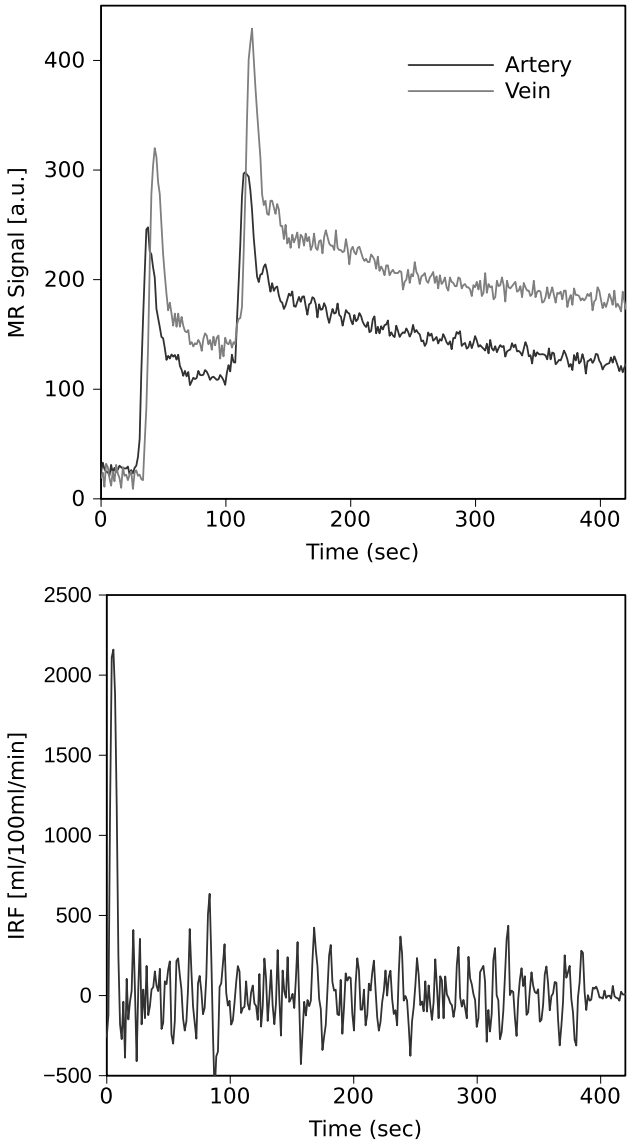

Figure 24: Top: arterial and venous contrast agent concentrations, measured in a patient from the study presented in Ch. 7. Bottom: Corresponding impulse response function, determined by deconvolution of the venous with the arterial concentration. In this case, the apparent venous blood volume was determined as $v_{b,v}^{app} = 205\,\mathrm{ml}/100\mathrm{ml}$; the partial volume correction factor was thus $p = 100/205$.

range of 0.40 to 1.0 with a mean value of 0.69 (Chapter 7) and 0.31 to 0.58 with a mean value of 0.43 in the study presented in Chapter 8. Since the in-plane resolutions in both studies were comparable, this difference can be explained by the location in which the arterial input functions were measured: in the tumor study, the AIF was measured in the comparably large carotid arteries, whereas the AIF in the MS study was measured in the middle cerebral artery which has a much smaller diameter.

It should also be mentioned that in the case of very long total acquisition times TA the effects of delay and dispersion between arterial and venous contrast agent concentrations play a much smaller role. The areas under the two curves are then dominated by the steady-state concentrations in the two regions, and the contribution of the first-pass peaks of contrast agent to the area under the curves becomes much smaller. If this is the case, the value of p can be approximated simply by [90]

$$p = \frac{\int_0^{TA} c_a^m(t)dt}{\int_0^{TA} c_v(t)dt} \tag{6.18}$$

with the advantage that no numerically involved deconvolution algorithm is required.

The assumption underlying this approach for partial volume correction is that the signal enhancement in the arterial voxel is dominated by the intravascular compartment and that no tracer accumulates in the perivascular interstitial space during the time of the measurement. Although we did not observe this in our study, care must be taken that this assumption is not violated.

7

QUANTIFICATION OF CEREBRAL PERFUSION AND PERMEABILITY WITH 2D DCE MRI: HEMODYNAMICS IN BRAIN TUMORS

This chapter presents a feasibility study, which combined a DCE-MRI acquisition for the measurement of tracer concentrations with a two-compartment modeling approach for the quantification of intravascular and interstitial hemodynamic parameters in brain tissue as well as in primary and secondary brain tumors.

For the quantification of cerebral perfusion with bolus tracking MRI, dynamic susceptibility (DSC) MRI has long been the method of choice. DSC MRI employs the strong decrease in signal intensity that arises if the contrast agent remains intravascular, so that the signal changes in healthy brain tissue during bolus passage are large despite the low blood volume in white and gray matter. DSC MRI, however, suffers from two major limitations if absolute quantification of cerebral blood flow (CBF) and cerebral blood volume (CBV) is to be achieved. The first difficulty arises in the measurement of the arterial input function (AIF), since the contrast agent relaxivity differs between blood and tissue; the ratio of the relaxivities is reflected directly as a scaling error in quantitative parameter estimates. The second difficulty is imposed if the contrast agent does not remain intravascular, but is able to extravasate into the extracellular, extravascular volume. This does usually not happen in healthy brain parenchyma, since the blood-brain barrier effectively confines the contrast agent molecules to the intravascular volume; if however the integrity of the BBB is disturbed, which is the case in inflammation or in tumor blood vessels, the contrast agent may extravasate and thereby reduce the susceptibility contrast, as well as amplify the T_1 effects. If these effects are not corrected for, e. g. with data truncation, gamma variate fitting or modeling approaches, the tracer concentration may be underestimated or even appear negative, leading to large errors in quantification.

These two difficulties do not arise when dynamic contrast-enhanced MRI is used for the dynamic measurement of contrast agent concentration. The T_1 relaxivities of contrast agent are essentially equal in arterial blood and in tissue so that the measurement of the arterial input function is less problematic. Moreover, extravasation of the contrast agent has no detrimental effect on the contrast mechanism. On the other hand, the T_1 relaxivity is smaller by an order of magnitude than the T2 relaxivities, together with the small cerebral blood volume in brain parenchyma, this

leads to small signal changes during the passage of the contrast agent bolus. Since a fast measurement is essential for sufficient sampling of the bolus passage, the contrast-to-noise ratio in cerebral DCE MRI is low, impeding the determination of quantitative parameters. However, for the purpose of absolute quantification, DCE MRI may be a more appropriate approach than DSC MRI.

The objective of this study was therefore to evaluate the feasibility of quantification of cerebral blood flow (CBF), cerebral blood volume (CBV) and the permeability surface product (PS) as a measure of BBB leakage by combining dynamic contrast-enhanced MRI (see Ch. 4) with a robust two-compartment modeling approach (see Ch. 5), that is applicable both for tissue with intact as well as with leaking BBB.

The work presented in this chapter has been published previously in [49].

7.1 MATERIALS AND METHODS

PATIENTS The objective of this study was to investigate the feasibility of cerebral perfusion quantification with a T_1-weighted dynamic measurement. Therefore, a heterogeneous patient collective was included in the study in order to evaluate our approach in a wide range of physiologic variations. The study was approved by the institutional review board, informed consent was obtained from all patients. In the study, 15 patients either with primary tumors of the brain ($n = 4$) or cerebral metastases ($n = 11$) were examined with DCE MRI. The metastases were produced by melanomas ($n = 2$), bronchial carcinomas ($n = 4$), lung carcinomas ($n = 3$), breast carcinoma ($n = 1$) and colon carcinoma ($n = 1$). Likewise, the treatment history was heterogeneous – four patients were untreated, all others had either received radiation therapy, surgery, chemotherapy or a combination thereof.

DATA ACQUISITION The measurements were performed on a 3T system (Magnetom Tim Trio, Siemens Healthcare, Erlangen) with a standard head coil. Precontrast measurements included a T_2-weighted FLAIR sequence that was used to determine the slice positions of the precontrast T_1 mapping sequence and the dynamic measurement.

For precontrast T_1 mapping as well as for the dynamic acquisition, a 2D saturation recovery spoiled gradient echo (TurboFLASH) sequence was used to acquire 6 slices, one of which was placed through the base of the skull to measure the arterial input function, the other five slices were cranial of the first to achieve optimal coverage of the lesion (or, if present, multiple lesions), as well as contralateral white and grey matter. The sequence parameters for both sequences are shown in Table 2; both

Table 2: Parameters used for the dynamic acquisition and precontrast T_1 mapping.

Sequence parameters	
matrix size	128×128
FOV	$240 \times 240\,\mathrm{mm}^2$
in-plane resolution	$1.875 \times 1.875\,\mathrm{mm}^2$
slice thickness	3.5 mm
phase encoding steps	96
TE/TR	1.34/2.6 ms
bandwidth	735 Hz/px
flip angle	15°

sequences were accelerated using GRAPPA with an acceleration factor of 2 and 24 reference lines. For precontrast T_1 mapping, 17 saturation recovery times in the range of 70 ms to five seconds were used, the number of averages was increased for the short saturation recovery times, the total acquisition time for the T_1 measurement was 3 minutes. For the dynamic acquisition a fixed saturation recovery time of 120 ms was used, so that six slices could be acquired every 1.34 s.

For the administration of contrast agent we used a dual bolus protocol, injecting two half (0.05 mmol/kg body weight) doses of Gd-DTPA (Magnevist, Bayer Schering) intravenously at a rate of 3 ml/s, separated by 60 seconds in order to reduce the peak concentration during the first pass of contrast agent without sacrificing the effect of a full dose of contrast agent at late phases.

POST-PROCESSING All image data were processed using our in-house written software PMI 0.3. After import of the dynamic data, a map of the precontrast signal S_0 was calculated as the mean of the first 15-20 (depending on the arrival time of contrast agent) frames. The background was segmented out using a manually defined threshold on S_0, for all further processing the background was excluded to speed up the calculations. In the next step, the signal enhancement $S(t_i) - S_0$ was calculated for each pixel and each time point t_i; from the signal enhancement curves, the area under the curve (AUC) was calculated on the pixel level using trapezoidal integration. The resulting AUC map was used to identify and define the following regions of interest:

- The six pixels with the highest AUC values in the internal carotid arteries (ICA), for the measurement of the arterial input function. The ICAs were delineated by circular regions drawn in the most caudal slice; to assess the reproducibility of this approach, this step was performed twice by two

independent observers (Steven Sourbron and Michael Ingrisch).

- A venous voxel, identified as the voxel with the highest AUC value in the sinus sagittalis.

A map of the precontrast relaxation rate R_{10} was calculated pixel-wise by fitting a monoexponential describing the signal as a function of the saturation recovery time T_S and R_{10} (see Eq. (4.12)) to the data acquired with variable saturation recovery times T_S.

The arterial input function was corrected for partial volume effects as described in Ch. 6.3. To derive the concentration in blood plasma, the AIF was rescaled with $1/(1-hct)$; a fixed value $hct = 0.45$ was assumed for the hematocrit, since individual values were not available.

To facilitate a more reproducible definition of regions of interest in lesions, maps of plasma flow F_P, plasma volume v_P and the permeability surface area product PS were calculated by pixel-wise fitting of the uptake model (see 5.2.2) to the signal enhancement curves. Subsequently, a region of interest covering the lesion was drawn manually on the PS map; to exclude areas of necrosis and large blood vessels, the region was superposed on the F_P map and, if necessary, modified.

In the contralateral hemisphere, circular white matter (WM) and grey matter (GM) regions were drawn on the baseline (S_0) map; again the regions were superposed on the F_P map and, if necessary for the exclusion of large vessels, modified.

Once all regions in the dataset were defined, signal enhancement curves for each region were calculated by averaging the values of all pixels contained in the region. Quantitative values of the hemodynamic parameters in each region were determined by fitting both the two-compartment uptake (sec. 5.2.2) and the two-compartment exchange model (sec. 5.2.1) to the signal enhancement curve; the Akaike Information criterion (sec. 6.1.1) was used to determine which of the two models was most appropriate for the data; model selection was verified by visual inspection of the fit. Model fitting was performed using an implementation of a nonlinear least-squares Levenberg-Marquardt algorithm (MPFIT [87]) with default values for the number of iterations and convergence thresholds, no constraints or limits were imposed on the parameters. The initial values for the fit were kept fixed at $F_P = 120\,\text{ml}/100\text{ml}/\text{min}$, $PS = 12\,\text{ml}/100\text{ml}/\text{min}$, $v_P = 10\,\%$ and $v_E = 20\,\%$.

SIMULATIONS To investigate the effect of the temporal resolution and CNR on estimates of the hemodynamic parameters, a simulation study was set up. An arterial input function (AIF) was generated as a sum of gamma variate functions and a mo-

noexponential recirculation. To create a double-bolus AIF, the single-bolus AIF was copied, shifted by 60 seconds and added to the original AIF. All parameters were adjusted so that the AIF resembled a typical measured arterial input function. With this AIF, synthetic grey and white matter tissue curves were calculated with a one-compartment model, characterized by a mono-exponential residue function; for CBF and CBV in both tissue types, the mean values measured in the patient population were used (WM/GM: CBF 82/23 ml/100ml/min, CBV 2.6/1.3 ml/100ml). All synthetic data were generated with a temporal resolution of 0.01 s.

To estimate CNR in a representative measured dataset, the 2CU model was fit to the WM and GM curves and the fit was subtracted from the data to obtain the approximate distribution of noise. From the standard deviation of the noise and the maximal signal of the WM and GM curves, the CNR was estimated at 4.1 for white matter and 6.1 for grey matter; the CNR of the AIF was estimated from the same dataset at a very high value of 130.

To simulate the measurement process, the synthetic AIF and tissue curves were sampled with a time resolution of $dt = 1.34\,\mathrm{s}$; to suppress artificial oscillations, the starting point t_0 was chosen randomly in the interval $[0, dt]$. Normally distributed noise with the corresponding standard deviation (see above) was added to the curves.

The 2CU model was fitted to the simulated WM and GM curve, producing estimates of CBF, CBV and PS. These steps of "measurement" and data fitting were repeated 10^5 times; subsequently, histograms as well as mean, standard deviation and main percentiles of each parameter were calculated. These simulations were repeated with a fivefold increase in CNR to investigate the effects of sequence optimization; moreover, the effect of temporal resolution and CNR on parameter estimates was investigated by repeating the simulations with variable temporal resolutions between 0.2 s and 10 s and variable CNR between 1 and 20.

7.2 RESULTS

MEASUREMENTS All measurements could be performed without complications; in two patients, no white and grey matter lesions were defined, since the lesions and therefore the slices were located in the cerebellum. The AIF definition approach proved to be reproducible, both observers selected exactly the same arterial pixels in all datasets.

Fig. 25 shows maps of AUC in the slices where the arterial and venous regions were defined. The internal carotid arteries as well as the sinus sagittalis could always be easily identified on maps of AUC. The partial volume correction is demonstrated for the

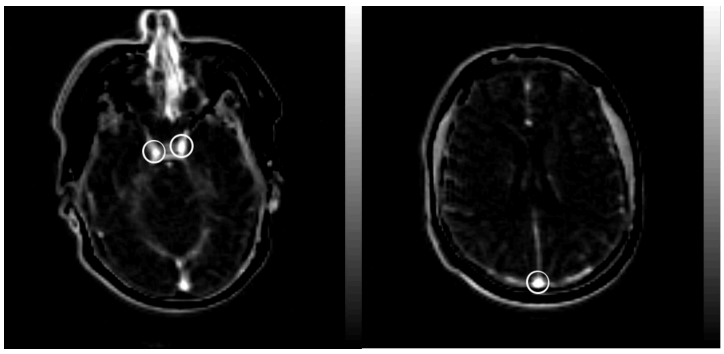

Figure 25: This figure illustrates the definition of arterial and venous regions on maps of AUC. Arteries and veins can easily be identified as regions with high values of AUC.

Table 3: Average T_1 estimates from all patients in our study, all values are given in ms

REGION	MEAN(STD. DEV.)	RANGE
Blood	2070(196)	1789 – 2535
White matter	957(68)	884 – 1067
Grey matter	1414(241)	1080 – 1850
Tumor	1733(411)	1020 – 2882

same dataset in Fig. 24; partial volume correction factors were in a wide range between 0.40 to 1.0, with mean 0.69 and standard deviation 0.20.

Figure 26 shows a typical result of the precontrast R_{10} measurement. In the T_1 map, white and grey matter appear well differentiated; no outliers can be observed. On the region of interest level, all tissue regions with the exception of the arterial region are well described by the monoexponential model.

T_1 estimates for venous blood, white matter, grey matter and tumor tissue are shown in Table 3; the T_1 values measured in the sinus, in white matter and in gray matter are close to literature values [91, 92].

Figure 27 shows a representative result of the pixel-wise analysis in a patient with a metastasis of a melanoma, obtained by fitting the two-compartment uptake model to each single pixel curve. PS is close to zero in all regions with healthy brain tissue, and distinctly demarcates contrast-enhancing lesions. CBV values in white and grey matter are in the appropriate range, whereas CBF appears to be higher in brain parenchyma than in the lesion. In general, lesions could be most readily identified on the PS maps and were also visible on CBV and CBF maps.

A quantitative analysis is shown in Fig. 28. The arterial input function (not shown) is similar to the arterial input function in

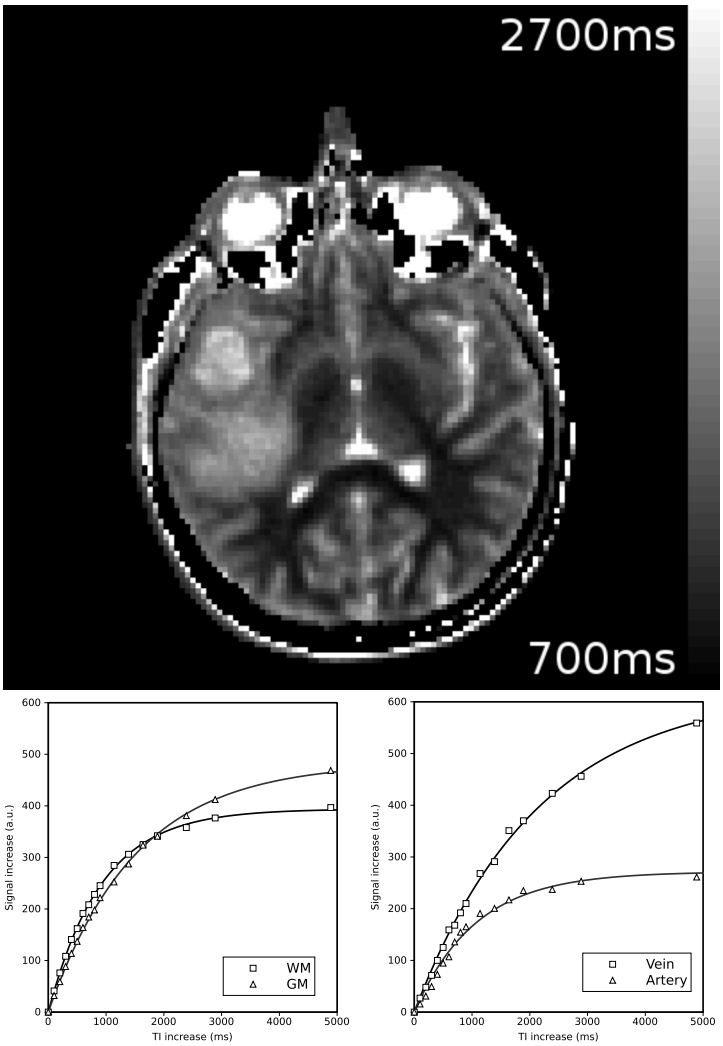

Figure 26: Representative T_1 measurement. Top: T_1 map showing a large tumor in the right hemisphere, bottom left: quantitative T_1 estimations on the ROI level in WM (923ms)and GM (1506ms), bottom right: T_1 estimations in the sinus sagittalis (2134ms) and in the artery (1126ms).

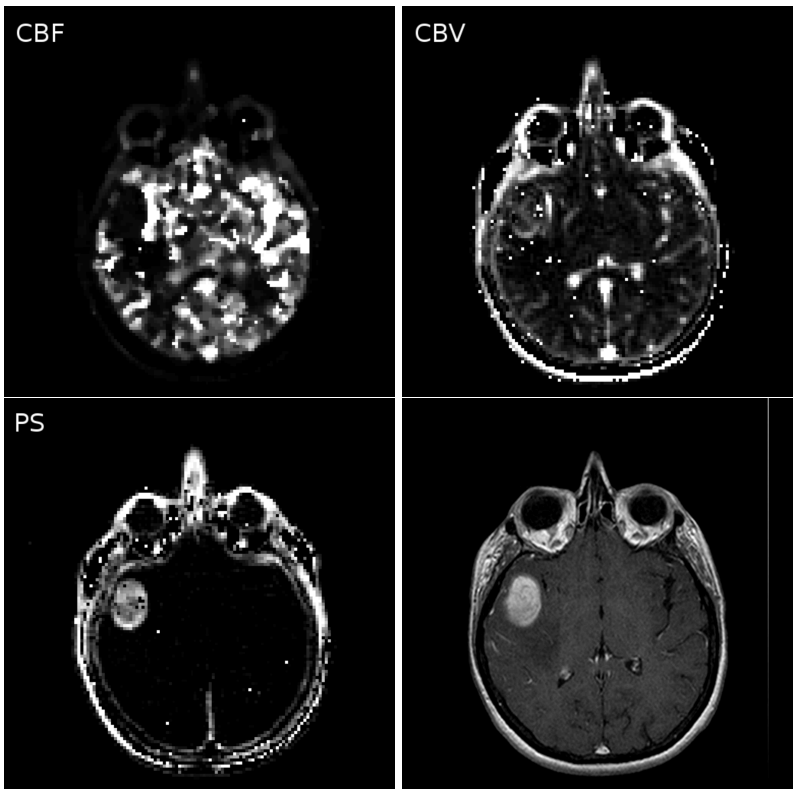

Figure 27: Parameter maps of CBF (median-filtered), CBV and PS in the same slice as Fig. 26, calculated with the two-compartment uptake model. Bottom right: high resolution contrast-enhanced T_1-weighted image at approximately the same slice position. The lesion, a metastasis of a melanoma, is easy to identify on the PS map and shows increased CBV. Singular outliers are visible on CBV and PS maps, the CBF map suffers from strong artifacts.

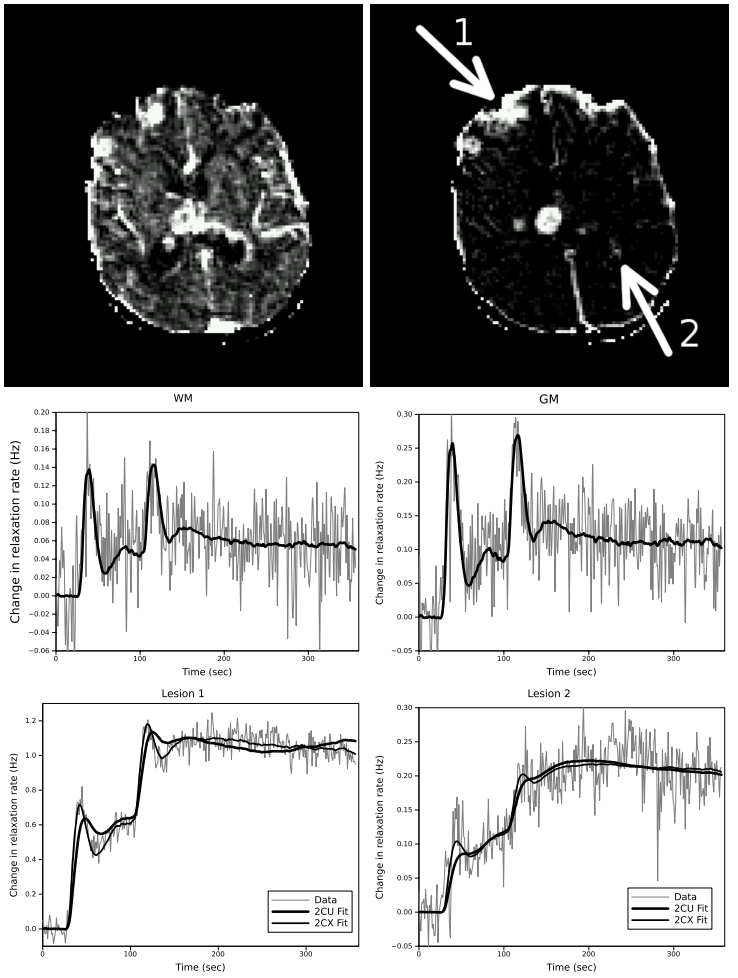

	WM	GM	Lesion 1	Lesion 2
CBF [ml/100ml/min]	14	20	92	14
CBV [ml/100ml]	0.9	2.9	8.6	1.6
PS [ml/100ml/min]	-0.03	0.04	8.5	2.0
v_E [ml/100ml]	n/a	n/a	12	2.4

Figure 28: Quantitative analysis on the region level in a patient with multiple metastases of a small cell lung carcinoma. Top: Maps of blood volume and permeability surface area product. Second row: fits of the 2CU model to white matter (left) and grey matter (right). Third row: fits of the 2CU and 2CX models to two lesion curves, the position of the lesions is indicated on the PS map. Bottom row: parameter estimates for all four curves, the estimates of the lesion curves were obtained with the 2CX model

Table 4: Mean values and standard deviations of all parameters measured in tissue and tumor regions.

Parameter	Lesion	White matter	Grey matter
CBF [ml/100ml/min]	42(40)	23(14)	82(21)
CBV [ml/100ml]	8.9(11)	1.3(0.4)	2.6(0.8)
T_P [s]	12(12)	4.4(2.2)	2.1(1.1)
PS [ml/100ml/min]	2.3(2.2)	−0.03(0.08)	−0.009(0.05)
v_E [ml/100ml]	8.2(4.3)	n/a	n/a

Fig. 24 and clearly shows the two half-dose injections, each first pass peak is followed by the second pass of the contrast agent. The same form of the curve with substantially more noise can be observed in the white and grey matter regions; the 2CU model provided a good fit to the data obtained in all regions in normal appearing brain tissue, yielding a value of PS close to zero. In tumor regions, the two injections typically resulted in a "two step" form of the curve. The two steep increases were contributed by the vascular phase, followed by a slow increase corresponding to the uptake phase and, in some cases, by a washout phase with decreasing signal intensity. The 2CU model provided a close, but not perfect fit to the data, in most cases, the 2CU model showed a tendency to "oversmooth" the steep increases during the vascular phase. This tendency could not be observed when the 2CX model was used; generally, the 2CX model provided a better fit to the data. One exception was a region in a periventricular cerebral lymphoma; here, no washout was observed and the 2CX model did not improve the fit. Correspondingly, the AIC selected the 2CU model as the best model for this region.

An overview about the three parameters that could be measured with both models in all regions is presented in Fig. 29; the mean values and standard deviations of these parameters in all regions is shown in Table 4 .

SIMULATIONS Histograms of the parameter estimates for white and grey matter from the simulations are shown in figure 30. Open symbols display results for dt and CNR as in the patient data, closed symbols represent results from the simulations with a fivefold increase in CNR. A strong overlap of CBF estimates between WM and GM can be observed for the low CNR; increasing CNR by a factor of 5 leads to complete separation between both tissue types.

The effects of variation in CNR and dt are illustrated in figure 31. Changes in CNR and dt appear to have little effect on the bias of the results, but both reduction of CNR and increase of dt

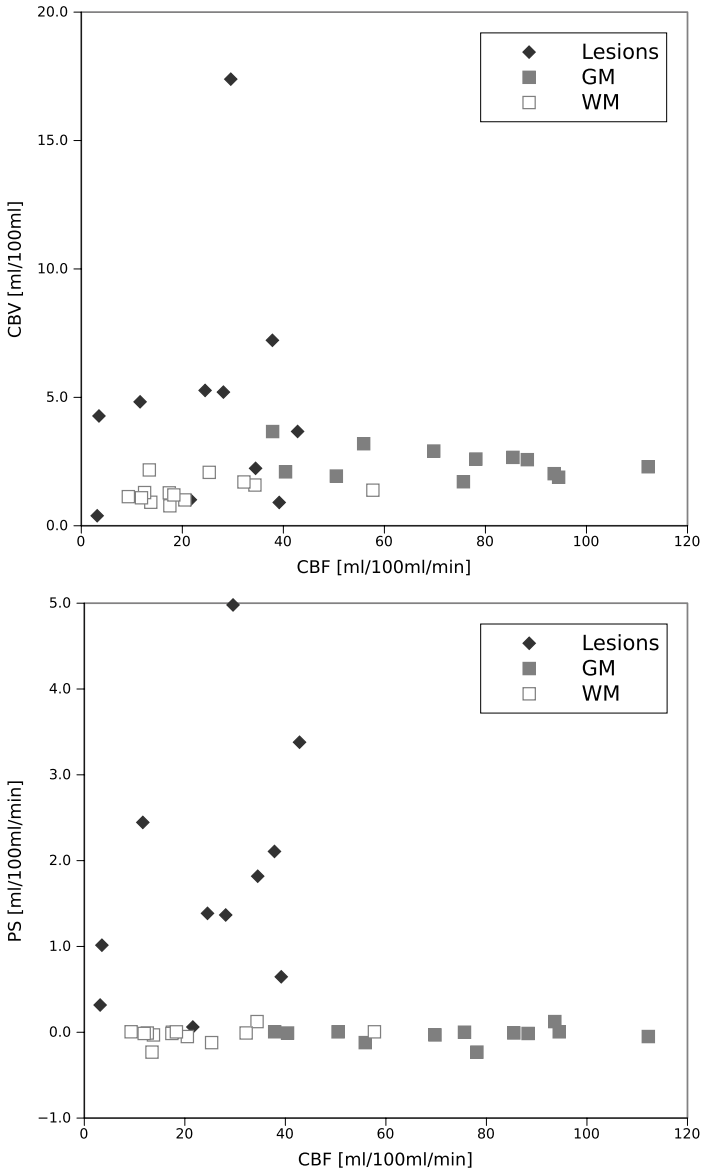

Figure 29: Scatter plots of parameter estimates in tumors (black diamonds), white matter (white squares) and gray matter (gray squares). Top: Plot of the vascular parameters CBV and CBF, bottom: permeability surface area product plotted against CBF, demonstrating the clear separation of tumors from healthy parenchyma by PS.

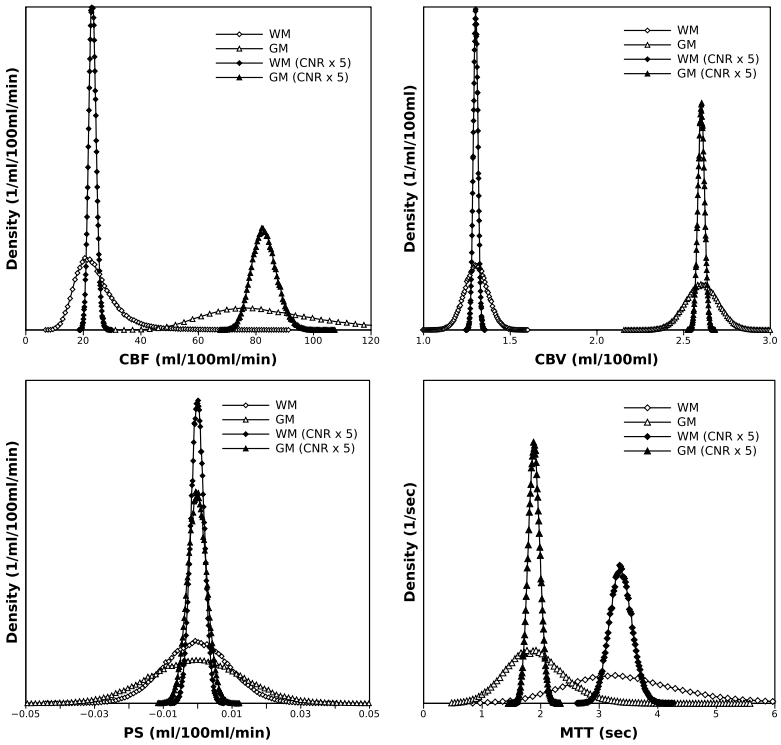

Figure 30: Simulation results - Histograms of CBF, CBV and PS estimates for white and grey matter showing the distribution of parameter estimates for two different CNRs. The overlap between WM and GM that can be observed for the low CNR vanishes completely if CNR is increased by a factor of five.

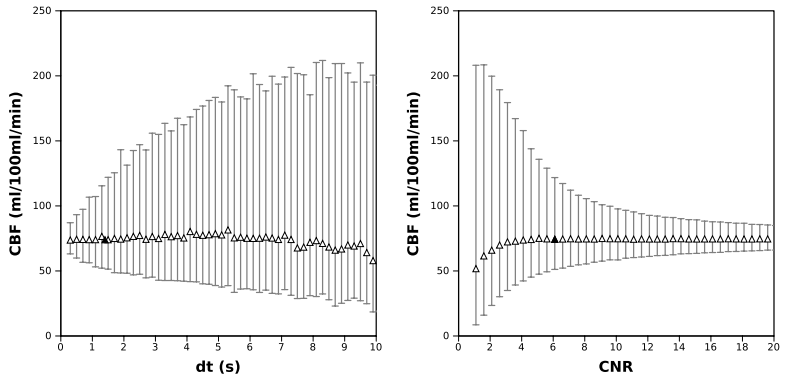

Figure 31: Simulation results demonstrating the effects of varying CNR and dt on the distribution of CBF. The filled triangle represents values of CNR and dt that are similar to the measured GM data. Decreasing dt or CNR severely reduce precision; on the other hand precision can be increased effectively by increasing CNR.

lead to a severe loss of precision. Moreover, figure 31 illustrates that the precision of the measurement can be improved more effectively by increasing CNR than by further reducing dt. A fivefold increase of CNR reduces the standard deviation of CBF from 21 ml/100ml/min to 3.9 ml/100ml/min, whereas a fivefold reduction of dt leads only to a reduction of the standard deviation to 8.5 ml/100ml/min.[1]

7.3 DISCUSSION

TRACER KINETIC MODELING The 2CU model was able to accurately describe all curves that were measured in normal brain tissue and yielded a vanishing permeability surface area product. This indicates that the assumption that the vascular space can be described by a compartment (i. e. is well mixed) is valid and appropriate for brain tissue. It may be argued that a one-compartment model may suffice for the description of health brain tissue and should be included in the set of models, since the 2CU model yields values of PS close to zero (see Table 4) and thus effectively reduces to a one-compartment model. However, the inclusion of the "uptake" compartment and the resulting additional parameter PS does not lead to numerical instability, so that neglecting the one-compartment appears justified. This is also indicated by the high precision of PS in the simulation results (Fig. 30).

1 In MRI, a fivefold increase in CNR can in general not be achieved by a fivefold reduction of dt. The exact dependence of CNR on dt depends to a large extent on the pulse sequence and acceleration schemes, but generally speaking, a fivefold increase of CNR would require approximately a twenty-fivefold reduction of dt.

In tumor regions, where a leaking blood-brain barrier can be assumed, the 2CX model was superior to the uptake model for most curves. This indicates that the assumption of small interstitial concentration and negligible backflow which defines the 2CU model does not hold for the long measurement times that were used in our study – instead, in late phases of the measurement, the interstitial concentration has increased to a degree where this assumption no longer holds, thereby rendering the 2CU model invalid. Dropping this assumption leads to the more general 2CX model, which describes the observed curves better and yields an additional parameter, the volume of the interstitial space v_E. The results indicate the validity of our modeling approach, in particular the restriction to two compartments and the assumption of well-mixedness in each compartment.

The two-compartment models form a promising alternative to the deconvolution approach that was used in [47]. A deconvolution analysis yields only two independent parameters, e.g. CBF and the volume of distribution. The volume of distribution is equal to the plasma volume if the blood-brain barrier is intact, but, if blood-brain barrier is ruptured and contrast agent can extravasate into the interstitial space, the volume of distribution equals the entire extracellular space. Hence, the interpretation of a deconvolution analysis requires additional knowledge of the status of the blood-brain barrier. This additional information is not necessary when a two-compartment model such as the 2CU or 2CX model can be employed, since both models characterize perfusion and permeability separately – a one-compartment analysis, on the other hand, gives rise to the same interpretation difficulties as a deconvolution approach.

In conditions with low CNR, model-free deconvolution without constraints on the residue function produces parameter estimates with low accuracy [71]. In [47], this problem has been addressed by imposing additional constraints on the form of the residue function, however, the number of degrees of freedom in a deconvolution approach is by far greater than in a modeling approach – the solutions of the 2CX and 2CU model have only four and three degrees of freedom, respectively. It can be assumed that this reduction of the degrees of freedom increases the numerical stability; this issue may be investigated in further simulation studies.

ACCURACY AND PRECISION The mean values of grey matter CBF measured in our study appear reasonable; PET studies have reported lower [36] as well as higher [93] values for CBF in normal volunteers. This variability may be explained by variations in the exact placement of the regions of interest. Our estimates for CBV appear reasonable and are in the range of $2 - 5\%$ that has been

reported for ex-vivo studies in [94], but PET values have been reported higher [36]. This observation may be due to the fact that our data were not measured in healthy volunteers; on the other hand, it is not unlikely that cerebral blood vessels in the PET scans have contributed to increased CBV through partial volume effects. In our data, the high in-plane resolution and careful ROI definition might have aided to reduce partial volume effects of blood vessels, thereby reducing the overall GM CBV.

Overall, our CBF and CBV estimates in white and grey matter are in the right order of magnitude. Although systematic errors can not be ruled out completely, our results warrant further studies.

Simulations as well as patient data show that CBF is the parameter with the highest variation, to the point that CBF does not reliably differentiate between white and grey matter (see Fig. 29). The simulation results also indicate that an increase of CNR markedly increases the precision of the CBF estimates, providing complete separation of white and grey matter for a fivefold increase of CNR.

We also observed a higher standard deviation of CBV in the patient data than in the simulations (0.8 vs. 0.1 for GM and 0.4 vs. 0.07 for WM). This can be attributed to two facts: firstly, a certain deviation in the placement of the regions of interest cannot be avoided; secondly, the observed high variability in CBV estimates probably reflects the heterogeneity in our patient population; since most of the patients underwent some form of therapy, brain tissue perfusion is likely to vary in a wider range than in a collective of healthy volunteers.

All perfusion and permeability metrics in tumors cover a wide range (see table 4), this is likely a consequence of the heterogeneity of our patient collective, both with respect to tumor type and to therapy. The range of extracellular, extravascular volume measurements is in good agreement with estimates $(4 - 12\%)$for typical tissue types [94]. The overall mean CBV value in tumors is higher than in white and grey matter, so that one might expect increased robustness of perfusion quantification due to the higher tissue concentrations. Interestingly, not all lesions are highly vascularized: in some lesions, we observed CBV estimates that are comparable to white matter CBV (see Fig. 29); this indicates that high accuracy is necessary e. g. to reliably differentiate tumor recurrence from pure radiation effects.

PROTOCOL OPTIMIZATION For any given spatial coverage, protocol optimization is a matter of balancing the spatial resolution against the temporal resolution (dt) and CNR. For the method presented in this work, an upper limit on the spatial resolution is imposed by the necessity to measure the venous

concentration, the spatial resolution needs to be chosen so that a pixel that is completely embedded into a vein can always be found.

It is generally appreciated that the choice of the temporal resolution is a major issue in perfusion quantification. The predominant assumption is that the temporal resolution should be faster than the mean transit time in the tissue; in [38], a temporal resolution faster than 1.5s in the brain is recommended. However, accurate CBF values for dt values longer than typical transit times have also been reported [52]. Fig. 31 illustrates this issue – firstly, the figure shows that an increase of dt does not increase the bias of CBF, but only the variance, so that accurate CBF estimates are still feasible with high values of dt. Moreover, the figure shows that no clear transition in the precision of parameter estimates occurs around the mean transit time of the tissue (1.9 seconds in this example).

The conclusion that can be drawn from this simulation is that the mean transit time does not provide a fundamental limit for the temporal resolution, instead, dt should be minimized as far as possible. Since in MRI a higher temporal resolution dt leads generally to a decrease of CNR, a reasonable trade-off of this two measures should be found. Our results indicate, that it may be advantageous to sacrifice temporal resolution for an increase of CNR; the simulation results presented in Fig. 30 show that an increase of CNR has a strong effect on the precision of parameter estimates.

The six slice 2D acquisition is a major limitation of our study. It is not possible to cover the whole brain, and, since only five slices are available to position over lesions, large gaps are the inevitable result. This imposes strong limitations if the objective of the measurement is either the evaluation of multiple lesions such as metastases or multiple sclerosis plaques, or if the location of the lesions cannot be determined on precontrast images. Furthermore, a reproducible slice positioning, which is a prerequisite for longitudinal studies, is difficult to achieve, in particular if the morphology of the lesions of interest changes between consecutive investigations. A viable alternative to multi-slice 2D acquisitions may be to employ a 3D sequence for the acquisition. With the arrival of sophisticated acceleration schemes like parallel imaging and view sharing in clinical routine, sufficient temporal resolutions for perfusion quantification have become feasible. 3D sequences provide intrinsically higher CNR and have the additional advantage that no preparation pulse is necessary for the measurement.

CONCLUSION In this study, we have investigated the feasibility of a T_1-weighted perfusion measurement for the assessment of

cerebral hemodynamics. For the quantification of hemodynamics, we have presented a compartment modeling approach that i) allows for clear separation of perfusion and permeability metrics and ii) is valid both for tissues with intact and with leaking blood-brain barrier. On the pixel level, the precision of parameter estimates, in particular of CBF, was low and insufficient for accurate quantification; our simulations indicate that this problem can be addressed with an increase of CNR. On the region-of-interest level, however, we found that our parameter estimates are in good agreement with reference values. In conclusion, DCE MRI may be a suitable alternative to the established DSC measurements, in particular, since the measurement of an arterial input function is straightforward and blood-brain barrier leakage does not impose a fundamental constraint on the quantification.

8

QUANTIFICATION OF CEREBRAL HEMODYNAMICS IN MULTIPLE SCLEROSIS: DCE MRI IN 3D AT 3T

In our initial study (Ch. 7), we were able to demonstrate the feasibility of the quantification of cerebral hemodynamics with T_1-weighted DCE MRI with a 2D acquisition. The restriction to only few slices and the ensuing incomplete coverage of the brain was identified to be a main limitation of the measurement approach, hindering the characterization of multiple lesions as well as the assessment of lesion evolution by longitudinal measurements. For these purposes, a 3D acquisition with full coverage of the brain would be desirable.

The quantification of cerebral hemodynamics requires a dynamic acquisition with sufficiently high spatial and temporal resolution and contrast-to-noise ratio. To satisfy these demands with a 3D measurement providing large spatial coverage, the use of modern imaging techniques such as parallel imaging and view sharing is mandatory.

MULTIPLE SCLEROSIS In this study, a collective of patients with multiple sclerosis (MS) was investigated. MS is a chronic, inflammatory, demyelinating disease of the central nervous system that is characterized by the presence of multiple lesions, mostly located in normal-appearing white matter (NAWM). These lesions are typically in variable states of inflammatory activity, ranging from chronic lesions without inflammation to active lesions with high inflammatory activity. An active lesion is characterized by acute inflammation and consequently exhibits increased CBV and a breakdown of the blood-brain barrier (BBB). This lesional inflammation is usually assessed as focal enhancement in T_1-weighted imaging after administration of contrast agent[25, 95]. This approach, however, yields only binary information about the state of inflammation, at most, lesional activity can be graded e. g. as "weak enhancement" or "strong enhancement". Additionally, the degree of enhancement in a lesion does not only depend on physiological parameters such increased vascularity or BBB leakage, but also on a range of experimental parameters such as the type and dosage of contrast agent, the delay between contrast agent administration and imaging and various MRI acquisition parameters [96, 97]. The assessment of quantitative and physiologic hemodynamic parameters such as CBF, CBV and PS may allow for a more fine-grained assessment of inflammatory activity.

Changes in perfusion are known to precede the development of BBB leakage in an active lesion by several weeks [98] and are thus assumed to form an early step in the development of a new lesion. Moreover, several studies [41, 99–102] have reported reduced perfusion in NAWM in patients with MS.

For the assessment of lesional hemodynamics, both a high spatial resolution and a large spatial coverage of the DCE MRI measurement are required – in particular, if the characterization of contrast-enhancing (CE) lesions is desired, since it cannot be decided on pre-contrast images, whether a lesion will show contrast enhancement or not. To fulfill these demands on the DCE MRI acquisition, a 3D acquisition can be employed. Sufficient temporal resolution of the measurement can be achieved with advanced acceleration schemes such as parallel imaging or view sharing. On the post-processing level, the issue of low CNR can be addressed with quantification algorithms that reduce the number of free parameters, either by introducing additional constraints on the residue function [47, 48], or by modeling approaches such as in Chapters 5 and 7.

The purpose of the study presented in this chapter was therefore to evaluate the feasibility of a 3D DCE MRI measurement with coverage of the entire brain for the quantification of cerebral hemodynamics in patients with MS. At the time of writing this thesis, the work presented in this chapter has been accepted for publication in *Investigative Radiology*.

8.1 MATERIALS AND METHODS

PATIENTS 19 consecutive patients (12 female, 7 male) with clinically definite MS of both who were scheduled for regular MRI were included in the study. No further exclusion criteria were defined, since this study was defined as a feasibility study. In particular, all subtypes of MS (relapsing-remitting (RR), primary-progressive (PP) and singular-progressive (SP)) were included. An overview about the clinical data of the patients is given in Table 5. With one exception (patient #15, who received interferon therapy), no patients received therapy at the time of the study. The median age of the patients was 35 (range 18 to 61 years). The institutional review board approved of the study, and informed consent was obtained from each patient.

MR IMAGING The imaging protocol included pre-contrast T_1-weighted and fluid-attenuated inversion recovery (FLAIR) imaging as well as post-contrast T_1-weighted imaging. All measurements were performed on a clinical 3T scanner (Magnetom Verio, Siemens Healthcare, Erlangen, Germany). The number of CE lesions was determined on conventional T_1-weighted contrast-

Table 5: Clinical data of the patients included in the study

ID	AGE	DISEASE TYPE	DURATION OF DISEASE IN MONTHS	RELAPSE AT TIME OF STUDY	EDSS	NUMBER OF CE LESIONS	NUMBER OF FLAIR-LESIONS
1	20	RR	2	y	1	1	20
2	47	RR	48	n	2	0	57
3	28	RR	6	n	2	20	129
4	35	RR	204	n	2	2	117
5	27	RR	4	n	0	0	7
6	18	RR	4	n	0	2	28
7	61	SP	132	n	4	0	73
8	38	RR	17	n	2.5	0	62
9	39	RR	5	n	2	0	48
10	33	RR	132	y	3.5	6	107
11	47	RR	11	n	3.5	0	3
12	24	RR	96	n	1	2	101
13	22	RR	6	n	1	2	57
14	57	RR	48	n	2	0	39
15	38	RR	24	n	1	0	65
16	35	RR	4	n	1	0	2
17	44	SP	336	y	4	1	75
18	23	RR	13	n	1.5	0	36
19	28	RR	156	y	4	15	101

Table 6: Sequence parameters of the 3D DCE MRI acquisition

Sequence parameters	
matrix size	$128 \times 104 \times 44$
field of view	$220 \times 178\,\mathrm{mm}^2$
in-plane resolution	$1.7 \times 1.7\,\mathrm{mm}^2$
slice thickness	3.0 mm
TE/TR	0.86/2.29 ms
flip angle	19°
bandwidth	1220 Hz/px
TWIST acceleration	$pA = 0.25, pB = 0.22$

enhanced images, the T_2 lesion load was assessed as the number of hyperintense lesions on FLAIR images.

DCE MRI ACQUISITION For the dynamic acquisition, a time-resolved 3D spoiled gradient echo sequence providing coverage of the entire brain was optimized to achieve sufficient spatial and temporal resolution for bolus-tracking MRI. For this purpose, the sequence was accelerated using parallel imaging with an acceleration factor of 2, 24 reference lines were acquired. Further acceleration was achieved through TWIST view-sharing (see 4.3.1) with $pA = 0.25$ and $pB = 0.22$. Sequence parameters are summarized in table 6. With this sequence, a volume consisting of 44 slices with an in-plane resolution of $1.7 \times 1.7\,\mathrm{mm}^2$ and a slice thickness of 3 mm covering the whole brain could be acquired every 2.1 s. In total, 200 volumes were acquired, resulting in a total measurement time of seven minutes.

The sequence was started 10 s prior to injection of a standard dose (0.1 mmol/kg body weight) of gadobutrol (Gadovist, Bayer Schering). To minimize the risk of signal saturation in the arteries during the first pass of the contrast agent and to reduce sampling errors in the arterial input function[61], the same double-bolus administration scheme as in chapter 7 was used. The contrast agent was administered in two half dose injections with a flow of 3 ml/s separated by 60 s, each injection was followed by a 30 ml flush of saline with the same flow.

After completion of the dynamic measurement, standard diagnostic T_1-weighted contrast-enhanced images were acquired.

POST PROCESSING The data were transferred to a separate workstation and analyzed with in-house written software (PMI 0.4 [88]). A map of the baseline signal S_0 was calculated by averaging over all time points before the arrival of contrast agent in the arteries. This map was used to define regions of interest

in periventricular normal appearing white matter (NAWM) and, in 13 patients, in non-enhancing (NE) white matter lesions after visual co-registration with the FLAIR images.

In contrast to the previous study, the arterial input function was not measured in the internal carotid arteries, but in the middle cerebral artery (MCA) to minimize the influence of the inflow effect. A region was manually defined that covered large parts of the MCA; in this region, the six pixels with the largest area under the curve (AUC) were automatically selected. After averaging the signal intensities in these pixels for each time point, the arterial plasma concentration was approximated using the absolute signal enhancement as

$$c_a(t) = (S(t) - S_0)/(1 - hct) \tag{8.1}$$

where hct is the hematocrit value, $S(t)$ the averaged signal intensity in the six MCA pixels at time t and S_0 the averaged baseline signal intensity. Since individual values of the hematocrit value were not available, a fixed value of $hct = 0.45$ was used throughout the study. The AIF was corrected for partial volume effects with a reference measurement in the sagittal sinus using the same method as in the previous study (see also section 6.3).

To simplify the definition of regions of interest in CE lesions, maps of the permeability surface area product (PS) were calculated by fitting the 2CU model to each pixel curve. To speed up the calculations, the background was excluded from this analysis by masking out all pixels below a threshold value on the baseline map. Fitting the 2CU model to each pixel curve produced maps of CBF, CBV and PS; the resulting PS-map was used to manually define regions in CE lesions in areas with non-zero PS.

For the quantitative analysis on the region of interest level, the time-resolved concentration in each of the previously defined regions was approximated using the signal enhancement $S(t) - S_0$ (see section 4.2.1). The relative signal enhancement could not be used, since a T_1-mapping sequence was not available for all patients. The 2CX, 2CU and 2CT models were fitted to the concentration-time curve of each region using the Levenberg-Marquardt algorithm [87]; the Akaike weights w_{AIC} (section 6.1.1) for each model were calculated and the parameter estimates of the model with the highest w_{AIC} were recorded.

8.2 RESULTS

In all 19 patients, the measurements were completed without complications. In nine patients, a total of 53 contrast-enhancing lesions was detected on post-contrast T_1-weighted images; 35 of these lesions were contributed by just two patients. NE lesions

Figure 32: Display of the slice positioning of the 3D DCE MRI sequence. The entire neurocranium is covered by the slab of 44 slices.

were visible on pre-contrast FLAIR images in all patients; in 13 patients, at least one NE lesion could be identified and defined on the map of the baseline signal.

Fig. 32 illustrates the spatial coverage of the DCE MRI measurement, the entire neurocranium is covered by the 44 slices of the 3D sequence. No visible inflow effects could be observed in the middle cerebral arteries, despite strong, inflow-related signal enhancement in the carotid arteries in caudal slices (see also Fig. 23). Partial volume correction factors for the AIF were in the range from 0.31 to 0.58, with a mean value of 0.43.

Fig. 33a shows precontrast FLAIR and contrast-enhanced T_1-weighted images of a patient with a single periventricular ring-enhancing lesion along with the corresponding slice of the PS-map that was calculated from the DCE MRI acquisition. The lesion can be delineated clearly on the FLAIR image, the ring enhancement is obvious on the T_1-weighted image and corresponds to the region with non-zero PS in the PS map. Fig. 33b shows signal enhancement curves and model fits in a region in periventricular NAWM and in the rim of the lesion. The models with the highest w_{AIC} for lesion and NAWM were the 2CX and the 2CU model, respectively. The lesion curve shows stronger signal enhancement than the NAWM curve and a slow increase in the late phase of the measurement. These observations are also reflected in the parameter estimates – both CBV and PS are higher in the lesion than in the NAWM region. The AIF that was

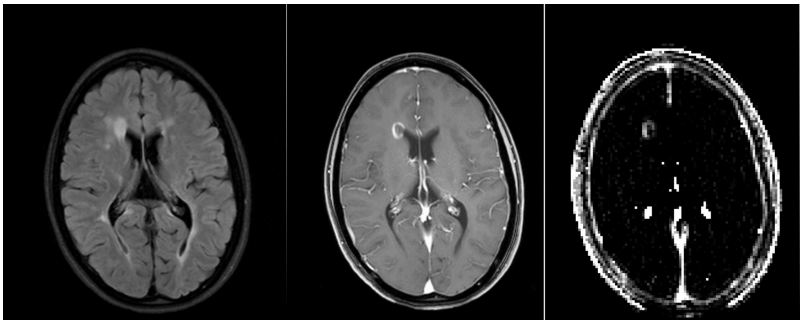

(a) From left to right: FLAIR, T_1, PS

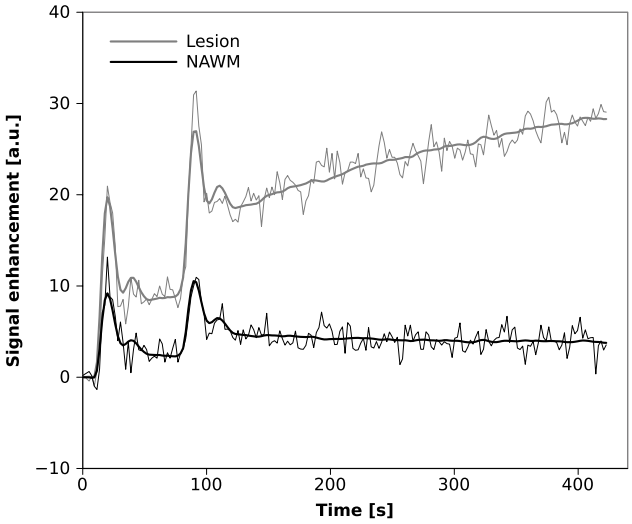

(b) NAWM and CE lesion curves and model fits

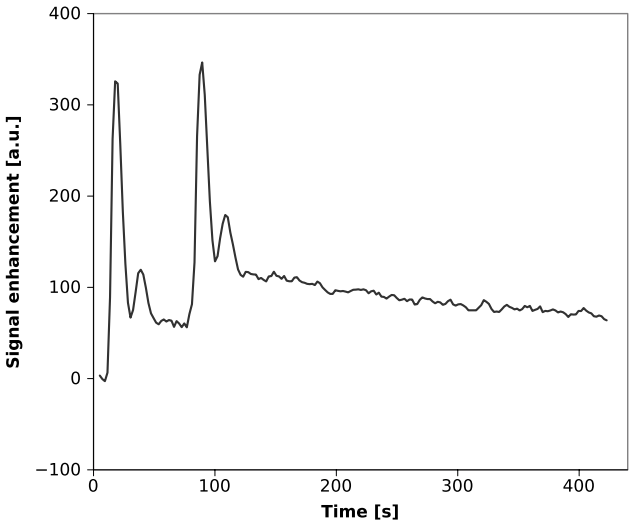

(c) Arterial input function

Figure 33: A patient with a single ring-enhancing periventricular lesion. Quantitative parameter values in lesion/NAWM were CBF: 19.7/9.7 ml/100ml/min, CBV: 1.25/0.65 ml/100ml, PS: 0.75/0.02 ml/100ml/min, v_E in the lesion: 12.5 ml/100ml

measured in the MCA is displayed in Fig. 33c. The two contrast agent injections are clearly separated, each bolus is followed by recirculation.

A different case is presented in Fig. 34; in this patient, seven CE lesions were visible in T_1-weighted contrast-enhanced images, six of which could be assessed in the DCE MRI measurement. Fig. 34a shows contrast-enhanced T_1-weighted images in two slice positions, along with the corresponding PS maps. In both slice positions, several CE lesions can be distinguished. Signal enhancement curves of the two indicated lesions as well as a signal enhancement curve in NAWM, along with model fits, are shown in Fig. 34b. In the late phases of the measurement, the signal enhancement in both lesions is similar, but the estimates of hemodynamic parameters differ notably between lesions: In lesion 1, both vascular parameters are higher than in NAWM, whereas in lesion 2, only CBF is increased and CBV is similar to NAWM. PS is increased in both lesions and is close to zero in NAWM.

Fig. 35 displays representative parameter maps and a high-resolution T_1-weighted contrast-enhanced image of another patient with multiple CE lesions. CBV and PS maps allow for discrimination of anatomical features as well as of CE lesions, isolated pixels in which the fitting algorithm converted to non-physiological values can be observed both in CBV and PS maps. The image quality of the CBF map is poor, compared to CBV and PS maps, even after application of a median filter to remove isolated pixels where the fitting algorithm yielded non-physiological values.

For the 19 white matter regions and the 13 NE lesions, the 2CU model was, according to the AIC, the best model. 51 out of the 53 CE lesions could be identified on the PS maps and were successfully characterized by the 2CT model (9 lesions), the 2CU model (11 lesions) and the 2CX model (31 lesions). Two small CE lesions that were visible on contrast-enhanced T_1-weighted images could not be detected on the PS maps.

Results of quantification on the region-of-interest level are shown in Table 7 and in Figs. 36 and 37. No significant differences in CBF were observed between NAWM and NE lesions, but NE lesions had a weakly significantly increased CBV ($p < 0.05$). In CE lesions, CBF, CBV and PS were significantly ($p < 0.001$) higher than in NAWM; all three parameters had high variability.

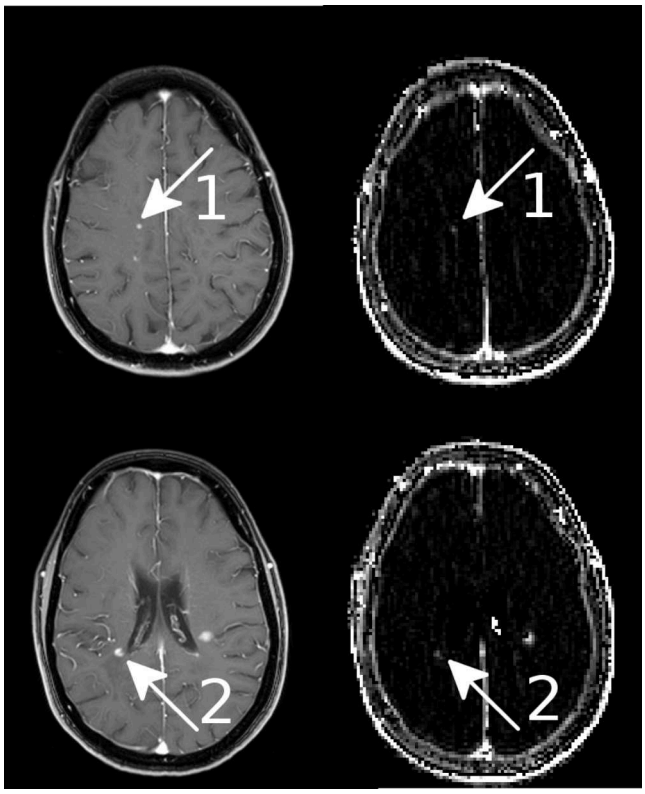

(a) Lesions at two different slice positions. Left column: contrast enhanced T_1-weighted images, right column: PS maps at corresponding slice positions

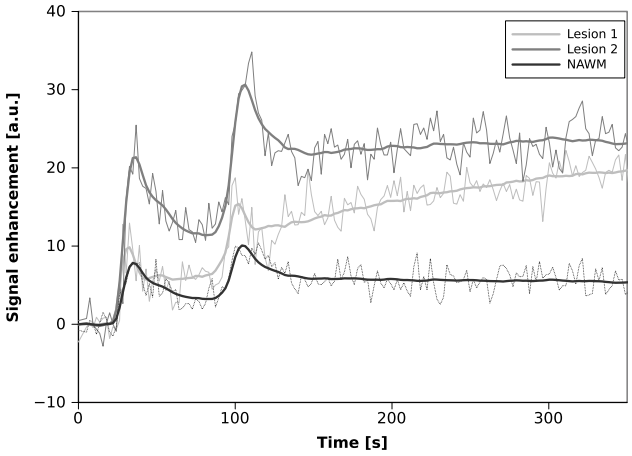

(b) Signal enhancement curves in the two indicated lesions and in periventricular NAWM, along with model fits

Figure 34: A patient with a multiple contrast-enhancing lesions. Parameters for lesion 1 were: CBF=26.0 ml/100ml/min, CBV=3.4 %, PS=0.83 ml/100ml/min, v_E=7.8 %; for lesion 2 CBF=64.0 ml/100ml/min, CBV=1.1 %, PS=0.95 ml/100ml/min, v_E=15.4 % and for NAWM: CBF=10.9 ml/100ml/min, CBV=1.3 % and PS= 0.06 ml/100ml/min

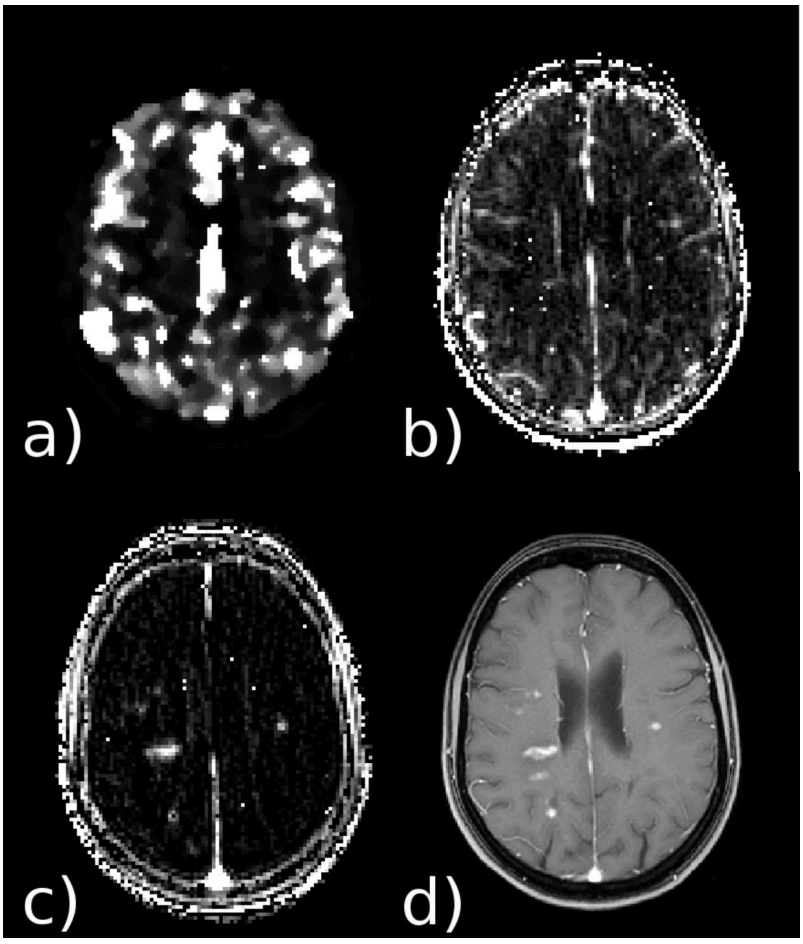

Figure 35: Representative parameter maps of CBF (a), CBV (b) and PS (c), along with a contrast enhanced T_1-weighted image (d).

Table 7: Mean values (standard deviations) of parameters estimates, averaged over all patients, in NAWM, NE and CE lesions. Units of CBF and PS are ml/100ml/min, units of CBV and v_E are ml/100ml. † and ‡ indicate significant ($p < 0.05$ and $p < 0.001$) difference to the corresponding NAWM parameter.

	n	*CBF*	*CBV*	*PS*	v_E
NAWM	19	15.8(6.7)	0.76(0.19)	.04(.03)	n/a
NE Lesions	13	19.1(12.4)	1.00(.35)†	.05(.04)	n/a
CE Lesions	51	28.9(22.7)‡	1.18(.48)‡	.98(.56)‡	10.7(3.46)

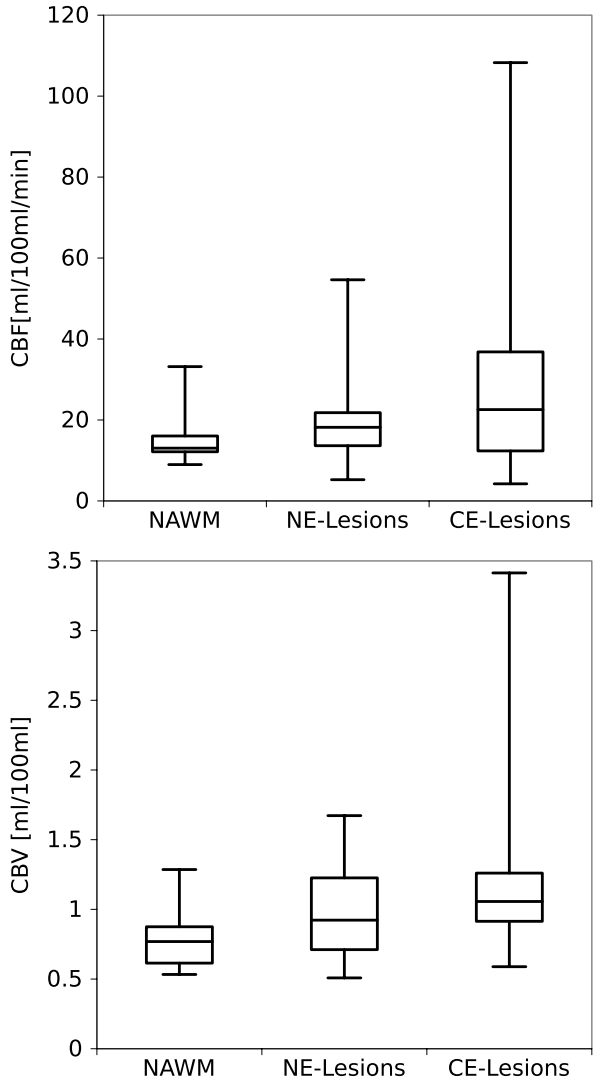

Figure 36: Box plots summarizing the results of perfusion quantification (see also Table 7). Top: distribution of CBF estimates in NAWM, NE and CE lesions, bottom: distribution of CBV estimates in NAWM, NE and CE lesions

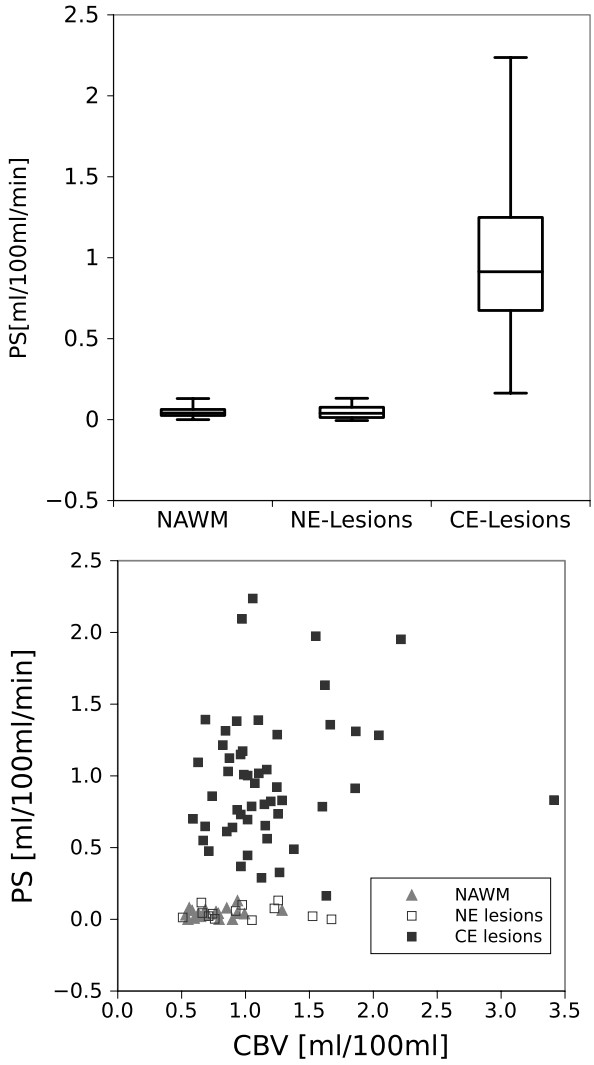

Figure 37: Top: box plot showing the distribution of PS estimates in NAWM, NE and CE lesions, bottom: plot of PS against CBV that shows the separation of CE lesions from NAWM and NE lesions by PS.

8.3 DISCUSSION

8.3.1 *3D DCE MRI*

Our study demonstrated the feasibility of a 3D DCE MRI measurement for the quantification of cerebral perfusion and BBB leakage. In the context of this study of MS lesions, the 3D acquisition enabled the hemodynamic characterization of multiple CE lesions scattered throughout the brain, despite the fact that the localization of CE lesions can in general not be determined prior to the administration of contrast agent.

A benefit of the 3D acquisition is that the AIF can be measured in the center of the excited volume, where inflow effects can be assumed to be minimal. This eliminates the need for non-selective saturation preparation pulses to minimize inflow effects and increases the available signal, since the longitudinal magnetization is not destroyed before each acquisition. Still, an accurate measurement of the AIF poses high demands both on spatial and temporal resolution of the acquisition. The spatial resolution must be high enough that a single voxel can be found that is completely embedded in a blood vessel – preferably in an artery, but if that is not possible due to the small diameter of arteries, a voxel in the sagittal or transverse sinus can be used for partial volume correction of the AIF as in this study.

The temporal resolution, on the other hand, must be high enough to accurately sample the first pass of the contrast agent bolus; in general, a temporal resolution below 2 seconds is recommended [90]. These competing demands of high spatial and temporal resolution on the acquisition can be satisfied with appropriate acceleration techniques, such as, in our case, with a combination of parallel imaging and view sharing. Our results demonstrate that CNR was still sufficient for quantification of hemodynamics on the region level, but the image quality of the parameter maps, resulting from a pixel-wise calculation, would benefit from an increase in CNR. Still, the parameter maps are useful for orientation and for definition of regions of interest, in particular, the PS map allowed for reliable definition of regions with BBB leakage. Further studies, however, should consider to employ a larger voxel size, since an increased voxel volume results in significant signal gain.

A potentially useful aspect of a 3D acquisition for DCE MRI is the possibility for image co-registration, that arises through the gapless coverage of the brain. In cross-sectional studies, co-registered images may allow for a more reliable definition of specific areas in the brain, such as white matter structures. In longitudinal studies, a co-registration of baseline and follow-up examination should be particularly useful for tracking of

lesion evolution, since lesion hemodynamics can still be evaluated even if the slice positioning is not exactly the same between examinations.

8.3.2 *Quantification*

MODEL SELECTION For all white matter regions and non-enhancing lesions, the Akaike information criterion favored the two-compartment uptake model. This confirms our model selection approach – since no contrast agent can leave the vascular bed due to the intact blood-brain barrier, it is not possible to determine the extravascular, extracellular volume, and the 2CT and 2CX models would be underdetermined and overfit the data. On the contrary, in contrast-enhancing lesions, the Akaike information criterion favored the exchange model in most cases. This is partly due to the fact that we used a relatively long total acquisition time, enabling estimation of the extravascular, extracellular volume, in combination with a high temporal resolution, so that CBF could be assessed as well. For some CE-lesions, however, the 2CT model or the 2CU model was chosen by the AIC. This indicates that, despite the long total acquisition time and the high temporal resolution, even data from CE lesions may not always contain enough structural information to justify the fit of all four parameters defining the full 2CX model.

CONTRAST-ENHANCING LESIONS We observed significantly increased CBF and CBV in CE lesions compared to NAWM. This observation may be attributed to vasodilation that occurs during inflammation in the evolution of a lesion. In a DSC-MRI study [41], similar results of significantly increased CBF (21.5(5.1) vs 16.9(3.7) ml/100ml/min, $p < 0.007$) and CBV (1.4(0.3) vs. 1.06(0.3) ml/100ml, $p < 0.001$) in CE lesions, compared to NAWM, were reported. The large variability in both parameters that we observed in CE lesions may be explained with the assumption that lesions were captured in different stages of lesion evolution. In a longitudinal study [98] a strong increase of CBV in early stages of lesion evolution was observed, followed by a decline over the course of 20 weeks. The authors explained the strong increase in CBV by inflammation-mediated vasodilation, and assumed that the subsequent decline might be due to development of a hypometabolic state. The significantly higher permeability surface area product that we observed in CE lesions indicates BBB leakage developing in the course of inflammation, again, the high variability (see Fig. 36) is presumably caused by varying degrees of inflammation during lesion evolution.

Consequently, the estimates of CBF, CBV and PS that can be obtained by the combination of T_1-weighted DCE MRI and com-

partment modeling may allow for an assessment of inflammatory activity in a lesion and may thus be useful for therapy monitoring or prediction of the future evolution of particular lesions.

NON-ENHANCING LESIONS In NE lesions, we observed a weakly significant difference to NAWM only for CBV. The reason for this increased CBV remains to be elucidated; yet, it is consistent with a previous study [41], in which a subset of NE lesions with increased CBV was identified. In this study, the increased CBV in the subset was assumed to be due to renewed inflammatory activity in these lesions; this is also consistent with a longitudinal study [98], which reported an increase in CBV already before the development of BBB leakage. The increased CBV in NE lesions that we observed may thus be attributed to renewed inflammatory activity in at least some of the NE lesions; this heterogeneity would also explain the high variability both of CBF and CBV. However, the quantification of hemodynamics in NE lesions demonstrated in this study should be seen only as proof of principle. For a more thorough investigation which could clarify this observation, a co-registration of FLAIR images as well as T_1-weighted images to the DCE dataset would be highly desirable. Such a co-registration would allow first for more reliable definition of regions in NE lesions, since regions could then be drawn directly on the FLAIR images, and second for a classification of NE lesions into subgroups by the appearance (hypo- or isointense) of these regions on T_1-weighted images. In a further step it could be investigated whether these subgroups differ with respect to their hemodynamics.

NAWM PERFUSION We observed relatively low values of CBF and CBV in NAWM in all examined MS patients, compared to values from other studies performed with T_1-weighted DCE MRI [48, 49]. This finding is consistent with the results of several studies that were performed using DSC MRI [41, 99, 100, 102]; these studies demonstrated significantly reduced CBF in NAWM of patients with MS compared to control groups. The reason for this hypoperfusion is not entirely clear [103]; hypoperfusion might be either primary as a result of a vascular pathology or secondary as a result of regional hypometabolism. In a recent study [101], correlations between reduced perfusion and reduced mean diffusivity were found; the authors attributed this observation to a primary ischemic origin of hypoperfusion.

8.3.3 *Limitations*

There are some limitations of our study that need to be taken into account when interpreting the data. The major limitation of our

study is the lack of a control group. Lacking such a control group, we cannot entirely exclude a systematic error that contributes to our observation of NAWM hypoperfusion in MS, although this finding is in accordance with several other studies. However, the most likely source of error in our analysis, namely the underestimation of the arterial input function due to nonlinear signal intensities, would have the opposing effect of overestimation of CBF and CBV.

Likewise, inflow effects would lead to a similar underestimation of the AIF. However, inflow effects in the middle cerebral artery appeared to be negligible compared to the inflow effects in the carotid arteries. Ultimately, the effects of a potential systematic error can only be assessed with the measurements in a control group of healthy subjects. This was beyond the scope of this first feasibility study, in particular since the risks of administering contrast agent to healthy subjects need to be considered.

Another limitation of our study may be the conversion of signal intensity to tracer concentration using the absolute signal enhancement. This may lead to an erroneous estimation of hemodynamic parameters; in particular, the arterial concentration might be underestimated or even clipped during the first pass of the contrast agent if a nonlinear regime of the signal equation (4.11) is reached. It is difficult to estimate the extent of potential nonlinearities from measured DCE MRI data, but the dual-bolus injection might at least aid in detecting obvious nonlinearities: The AIF in Fig. 33c displays a clear difference in the peak height of the two boli, indicating that at least no saturation regime was reached. However, this was not always the case, in other datasets, the difference between peak heights was smaller or almost vanishing. A more refined method for the measurement of concentrations, e. g. by inversion of the signal equation, might be beneficial for eliminating the issue of potential nonlinearities.

Another error in quantification may arise through inhomogeneities in the coil sensitivity profiles: if the coil sensitivities are different between the locations of artery and the tissue, the ratio directly enters as a scaling error into the quantification. This can be resolved by using the relative instead of the absolute signal enhancement (see also chapter 4.2). For this purpose, however, a pre-contrast T_1 measurement is required, which was not available for all patients at the time of the study.

8.4 CONCLUSION

In this chapter, we have demonstrated the feasibility of a 3D T_1-weighted DCE MRI measurement with gapless coverage of the whole brain for the assessment of cerebral perfusion in a collective of patients with MS. Our findings are in accordance

with previous DSC MRI studies and, in addition, we were able to measure perfusion and permeability in a straightforward manner also in areas with blood-brain barrier leakage.

The heterogeneity of MS lesion perfusion parameters that we found suggests a certain potential for the classification and differentiation of lesions; in order to investigate this potential, more data need to be collected, either in cross-sectional or in longitudinal studies. In the future, quantitative measurements of lesion hemodynamics may contribute to the prediction of future lesion development. A question of particular interest is whether a lesion will eventually, after the acute phase of inflammation, develop into a "black hole", a lesion that appears hypointense on T_1-weighted images.

To validate our observations, to assess stability and reproducibility of our method and to rule out any potential systematic errors, measurements in a control group would be of particular interest.

A limitation that has still not been addressed concerns the fact that reliable quantification is currently only feasible on the region level. The definition of regions is highly user dependent and may lead to a certain bias in the outcome of quantitative parameters. In this study, we have addressed this problem by a hybrid approach: regions were defined on maps of PS that were calculated on the pixel level with the 2CU model; for further quantification, the individual pixel curves in the previously defined region were averaged to increase CNR. To a certain extent, this approach reduces the observer bias, but, depending on the parameter map that is used for region definition, another bias may be introduced. For example, the definition of regions on a parameter map of PS ensures that only regions with non-zero PS are defined. Moreover, potential heterogeneity in the lesion is lost by the averaging process, thereby obscuring potentially important information. To overcome this problem, in particular in longitudinal studies with the purpose of monitoring disease progression or therapy monitoring, a quantitative analysis on the pixel level would be desirable, but this is currently not feasible with the low CNR that can be achieved by DCE MRI in the brain. Even higher field strengths, e. g. 7T, as well as new acceleration schemes such as compressed sensing or kt-BLAST may help to increase CNR and may eventually lead to more accurate and precise pixel-wise quantification of a range of cerebral hemodynamic parameters.

In conclusion, our study shows the feasibility of quantification of cerebral hemodynamics with coverage of the whole brain and sufficient spatial resolution for characterization even of small MS lesions. The acquisition and quantification protocol should be capable for the assessment of hemodynamics in a wide range of cerebral pathologies.

The assessment of therapy response of primary cerebral tumors such as gliomas under anti-angiogenic therapy might be an interesting application of this technique. Fig. 38 demonstrates the evaluation of a DCE MRI dataset, acquired with the same 3D sequence as in the MS study, in a patient with a recurrent high-grade glioma under anti-angiogenic therapy.

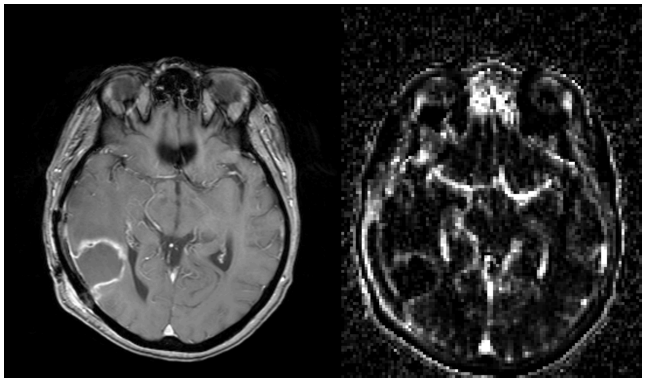

(a) Contrast-enhanced T_1-weighted image (left) and map of area under the curve (right), showing an enhancing tumor rim

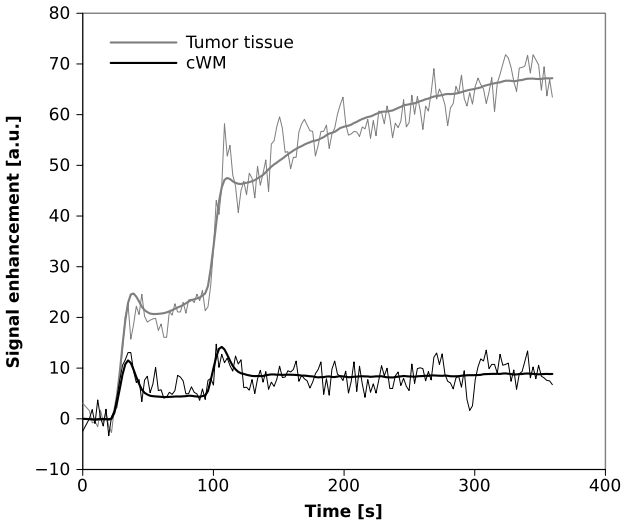

(b) Signal enhancement curves and model fits in the tumor rim and in contralateral white matter (cWM)

	CBF	CBV	PS	v_E
Tumor tissue	29.3	3.5	4.5	18.5
cWM	24.0	2.0	0.2	n/a

(c) Estimates of the hemodynamic parameters in the tumor rim and in cWM

Figure 38: DCE MRI evaluation of a patient with a recurrent grade IV astrocytoma

9

SUMMARY

Hemodynamic parameters such as blood flow, blood volume or the permeability of the vessel walls can be assessed with dynamic magnetic resonance imaging (MRI). In most organs in the body, a dynamic T_1-weighted pulse sequence is used for the dynamic acquisition. Since the presence of contrast agent causes signal enhancement in such an acquisition, this approach is commonly referred to as dynamic contrast-enhanced (DCE) MRI. Due to the special physiology of brain parenchyma, i. e. the small cerebral blood volume in combination with the blood-brain barrier (BBB), the assessment of cerebral hemodynamics with DCE MRI is challenging and therefore, a different method, dynamic susceptibility contrast-enhanced (DSC) MRI, has long been the method of choice for the assessment of cerebral hemodynamics.

However, for the purpose of absolute quantification of hemodynamic parameters such as cerebral blood flow (CBF) or cerebral blood volume (CBV), DSC MRI is less suitable and suffers from several limitations, in particular in areas with blood-brain barrier leakage such as inflammatory lesions or tumors. These problems do not occur if instead a DCE MRI measurement is used for data acquisition. Therefore, this thesis investigates whether DCE MRI is a suitable alternative to DSC MRI for the quantification of cerebral hemodynamics both in healthy parenchyma and in various pathologies.

For the assessment of tissue hemodynamics, a *bolus-tracking* experiment can be used. Here, a bolus of contrast agent is injected intravenously into the circulatory system. Subsequently, the spatially and temporally resolved contrast agent concentrations in tissue and in tissue-supplying vessels are monitored or tracked with a suitable modality, hence the name bolus-tracking. From these concentration-time courses, a variety of hemodynamic parameters such as CBF, CBV, the permeability of vessel walls (permeability surface area product, PS) and others can be derived by means of tracer-kinetic theory. The quantification of hemodynamic parameters from the data produced by such an experiment is essentially a two-step process: In a first step, the time-dependent contrast agent concentrations are derived from the measured signal (see Ch. 4); this step depends strongly on the imaging modality. In the second step, descriptive or physiological hemodynamic parameters are derived from the measured tracer concentrations by means of tracer kinetic theory (Ch. 5).

Tissue hemodynamics can be described mathematically with a compartment modeling approach. A compartment is considered a space in which a contrast agent or tracer is distributed uniformly. Different compartments can exchange tracer by means of flow, and the flow out of a compartment is proportional to the concentration in the compartment. For the description of cerebral hemodynamics with extracellular tracers, two compartments are sufficient: one compartment is formed by the intravascular space, this compartment can exchange tracer with the extravascular, extracellular space, which forms the second compartment. This situation can be described with the general two-compartment exchange model (see Ch. 5.2). However, in the context of DCE MRI, it may happen that this model is underdetermined, e. g. due to measurement constraints, and consequently results in unreliable parameter estimates. If this is the case, simpler models which incorporate additional assumptions need to be applied.

The selection of the most appropriate model is not straightforward: a model with more parameters will always yield a better fit than a model with fewer parameters, but at the cost of reduced precision of the parameter estimates. Therefore, a robust method for automated model selection in the context of DCE MRI was evaluated during the course of this thesis. This method is based on a quantity called Akaike Information Criterion (AIC), which penalizes the goodness of the fit with the number of free parameters. Applying this method requires the fitting of all models under consideration to the data; after a successful fit, the AIC is calculated for each model and allows for an objective and user-independent decision about which model is to be considered the best model. The potential of this method for automated model selection was investigated initially in a simulation study (Ch. 6, [80]). In a further step, the model selection approach was incorporated into existing, in-house written software in the form of an interface that facilitates the rapid evaluation of multiple models and regions e. g. in measured DCE MRI data.

In a first patient study (Ch. 7 and [49]), a saturation-recovery 2D sequence, acquiring a limited number of slices, was used for the dynamic acquisition of bolus-tracking data in 15 patients with various brain tumors and metastases. For the quantification of perfusion and permeability, two different two-compartment models were used; the selection of the most appropriate model for every dataset was performed by an expert user, assisted by the AIC. This study showed that DCE MRI in the brain is, in principle, feasible. However, the acquisition of only few slices proved to be impractical, since the slice positioning is crucial for the outcome of the quantitative analysis: Hemodynamics in the tumor rim are likely to be quite different from hemodynamics

in peritumoral brain tissue or in the tumor center. This study also highlighted the importance of a high contrast-to-noise ratio (CNR) for quantification.

In a second patient study (Ch. 8), a collective of 19 patients with multiple sclerosis (MS) were examined, with the aim to characterize cerebral hemodynamics both in inflammatory lesions, scattered throughout the white matter, and in normal-appearing white matter (NAWM). The limitation of insufficient volume coverage that was identified in the first study was addressed by using a 3D DCE MRI sequence which provided gapless coverage of the entire neurocranium. For quantification, the multi-model approach, combined with automated model selection, that was evaluated in Ch. 6, was used. Values of CBF and CBV in normal-appearing white matter and in non-enhancing lesions found in this study are in accordance with values from previous DSC MRI studies. Moreover, hemodynamics could be quantified also in inflammatory lesions with BBB leakage. This study demonstrated that i) a 3D acquisition for DCE MRI in the brain is feasible, ii) facilitates the quantification of hemodynamics in lesions scattered through the entire brain as well as in NAWM and iii) that the multi-model approach with automated model selection is suitable for tissue with intact BBB as well as for tissue with BBB leakage. The results and findings presented in this chapter have been accepted for publication [104].

The values of CBF and CBV that were determined in both patient studies are in a reasonable range. In order to identify and rule out any potential systematic errors and to validate the proposed approach, further measurements in a collective of healthy volunteers would be beneficial. This issue is addressed in an ongoing study. On the technical level, the introduction of quantitative pre-contrast T_1 mapping into the measurement protocol would be highly desirable; the feasibility of the variable flip angle approach has already been demonstrated in some patients of the MS study.

During the course of this thesis, a methodology has been developed and evaluated that allows the characterization and quantification of cerebral hemodynamics from dynamic contrast-enhanced MRI data both in healthy brain parenchyma and in regions with blood-brain barrier leakage. In two patient studies, the feasibility of the developed methods has been demonstrated and it was shown that, with the proposed methods, DCE MRI forms a suitable and promising alternative to DSC MRI for the quantification of cerebral hemodynamics.

10 ZUSAMMENFASSUNG

Hämodynamische Parameter wie der Blutfluss, das Blutvolumen oder die Permeabilität der Gefäßwände können mit einer dynamischen Magnetresonanztomographie-(MRT-)Messung beurteilt werden. In den meisten Organen im Körper wird für diesen Zweck eine T_1-gewichtete Sequenz verwendet. Bei einer solchen Messung verursacht die Anwesenheit von Kontrastmittel eine Signalerhöhung, man spricht deshalb von dynamischer kontrastverstärkter (*dynamic contrast-enhanced*, DCE) MRT. Im Gehirn wird die Quantifizierung der Hämodynamik mit einer solchen Messung durch zwei physiologische Besonderheiten, nämlich das geringe zerebrale Blutvolumen und das Vorhandensein der Blut-Hirnschranke, erschwert. Durch die Kombination dieser beiden Faktoren können mit einer DCE-MRT-Messung nur geringe Signaländerungen und damit ein schlechtes Kontrast-Rausch-Verhältnis (CNR) erzielt werden. Aus diesem Grund wird die zerebrale Hämodynamik gewöhnlich mit einer anderen Methode, der dynamischen suszeptibilitätsgewichteten (DSC) MRT, beurteilt.

Wenn allerdings eine absolute Quantifizierung von zerebralen hämodynamischen Parametern erwünscht ist, ergeben sich bei Verwendung der DSC MRT einige fundamentale Schwierigkeiten, insbesondere wenn, wie z. B. in Tumoren oder entzündlichen Läsionen, eine Störung der Blut-Hirn-Schranke vorliegt. Da diese Schwierigkeiten bei einer DCE-MRT-Messung nicht auftreten, ist es das Ziel der vorliegenden Arbeit, zu untersuchen, ob die DCE-MRT trotz des schlechten CNRs eine geeignete Alternative zur konventionell verwendeten DSC-MRT darstellt.

Die Hämodynamik in gesundem Hirngewebe wie auch in intrakraniellen Läsionen kann mit einem sogenannten „bolus-tracking"-Experiment charakterisiert werden. Bei einem solchen Experiment wird ein Kontrastmittel als Bolus injiziert und anschließend die Kontrastmittelkonzentration im Gewebe sowie in den versorgenden Gefäßen mit hoher räumlicher und zeitlicher Auflösung gemessen. Aus dem Zeitverlauf der Konzentrationen im Gewebe und in arteriellem Blut können anschließend mit Methoden der Tracerkinetik eine Reihe von hämodynamischen Parametern wie zerebraler Blutfluss (CBF) und zerebrales Blutvolumen (CBV), aber auch die Permeabilität der Gefäßwände (permeability surface area product, PS) bestimmt werden. Die Quantifizierung der Hämodynamik zerfällt damit in zwei Einzelschritte: i) die zeitaufgelöste Messung der Kontrastmittel-

konzentration und ii) die daran anschließende tracerkinetische Analyse.

Zur mathematischen Beschreibung der Hämodynamik können sogenannte „Kompartiment-Modelle“ verwendet werden. Ein Kompartiment ist hier ein Raum, in dem Kontrastmittel gleichmäßig verteilt ist. Verschiedene Kompartiment können Kontrastmittel mittels Flüssen austauschen, der Fluss aus einem Kompartiment ist proportional zur Konzentration im Kompartiment. Für die mathematische Beschreibung der zerebralen Hämodynamik sind zwei Kompartimente ausreichend: ein Kompartiment wird vom intravaskulären Raum gebildet, dieses Kompartiment kann Kontrastmittel mit dem zweiten Kompartiment, dem extravaskulären, extrazellulären Raum austauschen. Beschrieben wird diese Situation durch das allgemeine „two-compartment exchange-“(2CX-)Modell. Nicht immer können alle Parameter dieses Modells zuverlässig bestimmt werden, es kann vorkommen, dass das Modell unterbestimmt ist. In diesem Fall muss auf einfachere Modelle zurückgegriffen werden, die mit zusätzlichen Annahmen als Spezialfall aus dem allgemeinen 2CX-Modell hervorgehen (siehe Kapitel 5.2).

Die Auswahl des jeweils am besten geeigneten Modells ist nicht trivial: Ein Modell mit mehr Parametern wird eine gegebene Kurve immer besser beschreiben können als ein Modell mit weniger Parametern, allerdings auf Kosten der Präzision der Parameter. Im Rahmen dieser Arbeit wurde deshalb eine Methode für die automatische Auswahl des jeweils besten Modells im Kontext der DCE-MRT evaluiert. Diese Methode basiert auf dem *Akaike Information Criterion* (AIC), das die Güte des Fits mit der Anzahl der freien Parameter des Modells verrechnet. Um mit dieser Methode das beste Modell für eine gegebene Kurve zu bestimmen, werden zunächst alle Modelle an die Kurve angefittet und anschließend das AIC berechnet. Auf der Basis des AIC kann damit objektiv und benutzerunabhängig entschieden werden, welches Modell als das beste für diese Kurve zu betrachten ist. In der vorliegenden Arbeit wurde eine Simulationsstudie (Kapitel 6 und [80]) durchgeführt, mit der das Potential dieser automatisierten Modellauswahl im Kontext der DCE-MRT untersucht wurde. Im Anschluss wurde ein Interface für die bestehende Software PMI 0.4 implementiert, das die einfache Anwendung des Modellselektions-Ansatzes auf gemessene Patientendaten erlaubt (siehe Kapitel 6.2).

In einer ersten Patientenstudie (Kapitel 7, [49]) wurden 15 Patienten mit primären Hirntumoren und Metastasen mit einer dynamischen, T_1-gewichteten 2D-Sequenz untersucht. Für die Quantifizierung der hämodynamischen Parameter wurden zwei verschiedene Modelle benutzt; das jeweils beste Modell

wurde vom Auswerter, unterstützt durch das AIC, ausgewählt. Diese Studie konnte zeigen, dass die DCE-MRT zur Quantifizierung von Perfusion und Permeabilität grundsätzlich geeignet ist, konnte aber auch zwei Einschränkungen der verwendeten Messsequenz identifizieren: Zum einen legten die Simulationen nahe, dass die Quantifizierung erheblich von einer Erhöhung des CNR profitieren würde, zum anderen hat sich die Beschränkung auf nur wenige Schichten insbesondere zur Beurteilung von Tumorgewebe als nachteilig herausgestellt, weil die Positionierung der Schichten sehr starken Einfluss auf das Ergebnis der Quantifizierung hat und nur schlecht reproduzierbar ist.

In einer zweiten Patientenstudie (Kapitel 8) wurde ein Kollektiv von 19 Patienten mit multipler Sklerose (MS) untersucht. Ziel dieser Studie war die Charakterisierung der Hämodynamik sowohl in normal erscheinender weißer Hirnsubstanz (NAWM) als auch in akut entzündlichen und in chronischen MS-Plaques, die über die gesamte weiße Hirnsubstanz verteilt sein können. In dieser Studie wurde eine für die dynamische Akquisition optimierte 3D-Sequenz verwendet, um das Problem der Schichtpositionierung zu umgehen. Diese Sequenz erlaubte die lückenlose Abdeckung des gesamten Hirnschädels mit ausreichend hoher zeitlicher Auflösung. Zur Quantifizierung wurde der in Kapitel 6 vorgestellte Multi-Modell-Ansatz verwendet.

Die CBF- und CBV-Werte, die in dieser Studie in NAWM und in chronischen Plaques bestimmt wurden, stimmen mit Literaturwerten gut überein; zusätzlich konnten erstmals CBF, CBV und die Permeabilität der Gefäßwände in akut entzündlichen Läsionen quantifiziert werden. Mit dieser Studie konnte gezeigt werden, dass i) eine Quantifizierung der zerebralen Hämodynamik auch mit einer 3D-Messung möglich ist, ii) damit sowohl NAWM als auch MS-Plaques im gesamten Hirn charakterisiert werden können und iii) dass der vorgeschlagene Multi-Modell-Ansatz zusammen mit automatisierter Modellauswahl eine konsistente Beschreibung von Hirngewebe sowohl mit intakter als auch mit gestörter Blut-Hirn-Schranke ermöglicht. Die Ergebnisse dieser Studie wurden bei *Investigative Radiology* zur Veröffentlichung angenommen [104].

Zusammenfassend wurden in der vorliegenden Arbeit eine Reihe von Techniken und Methoden entwickelt, mit denen die Charakterisierung und Quantifizierung der zerebralen Hämodynamik sowohl in gesundem Gewebe als auch in Gewebe mit einer Störung der Blut-Hirn-Schranke ermöglicht wird. Mit diesen Techniken wurden zwei Patientenstudien durchgeführt, die zeigen konnten, dass die DCE-MRT eine vielversprechende Alternative zur konventionell benutzten DSC-MRT darstellt.

BIBLIOGRAPHY

[1] Rosen BR, Belliveau JW, Vevea JM and Brady TJ. Perfusion imaging with NMR contrast agents. *Magn Reson Med*, 14(2):249–265, May 1990.

[2] Nikolaou K, Schoenberg SO, Brix G, Goldman JP, Attenberger U, Kuehn B, Dietrich O and Reiser MF. Quantification of pulmonary blood flow and volume in healthy volunteers by dynamic contrast-enhanced magnetic resonance imaging using a parallel imaging technique. *Invest Radiol*, 39(9):537–545, Sep 2004.

[3] Fink C, Puderbach M, Bock M, Lodemann KP, Zuna I, Schmähl A, Delorme S and Kauczor HU. Regional lung perfusion: assessment with partially parallel three-dimensional MR imaging. *Radiology*, 231(1):175–184, Apr 2004.

[4] Ingrisch M, Dietrich O, Attenberger UI, Nikolaou K, Sourbron S, Reiser MF and Fink C. Quantitative pulmonary perfusion magnetic resonance imaging: influence of temporal resolution and signal-to-noise ratio. *Invest Radiol*, 45(1):7–14, Jan 2010.

[5] Dujardin M, Sourbron S, Luypaert R, Verbeelen D and Stadnik T. Quantification of renal perfusion and function on a voxel-by-voxel basis: a feasibility study. *Magn Reson Med*, 54(4):841–849, Oct 2005.

[6] Buckley DL, Roberts C, Parker GJM, Logue JP and Hutchinson CE. Prostate cancer: evaluation of vascular characteristics with dynamic contrast-enhanced T1-weighted MR imaging–initial experience. *Radiology*, 233(3):709–715, Dec 2004.

[7] Kershaw LE, Hutchinson CE and Buckley DL. Benign prostatic hyperplasia: evaluation of T1, T2, and microvascular characteristics with T1-weighted dynamic contrast-enhanced MRI. *J Magn Reson Imaging*, 29(3):641–648, Mar 2009.

[8] Scherr MK, Seitz M, Müller-Lisse UG, Ingrisch M, Reiser MF and Müller-Lisse UL. MR-perfusion (MRP) and diffusion-weighted imaging (DWI) in prostate cancer: Quantitative and model-based gadobenate dimeglumine MRP parameters in detection of prostate cancer. *Eur J Radiol*, May 2010.

[9] Köstler H, Ritter C, Lipp M, Beer M, Hahn D and Sandstede J. Prebolus quantitative MR heart perfusion imaging. *Magn Reson Med*, 52(2):296–299, Aug 2004.

[10] Sommer WH, Sourbron S, Huppertz A, Ingrisch M, Reiser MF and Zech CJ. Contrast agents as a biological marker in magnetic resonance imaging of the liver: conventional and new approaches. *Abdom Imaging*, Apr 2011.

[11] Villringer A, Rosen BR, Belliveau JW, Ackerman JL, Lauffer RB, Buxton RB, Chao YS, Wedeen VJ and Brady TJ. Dynamic imaging with lanthanide chelates in normal brain: contrast due to magnetic susceptibility effects. *Magn Reson Med*, 6(2):164–174, Feb 1988.

[12] Kiselev VG. Transverse relaxation effect of MRI contrast agents: a crucial issue for quantitative measurements of cerebral perfusion. *J Magn Reson Imaging*, 22(6):693–696, Dec 2005.

[13] Kjølby BF, Østergaard L and Kiselev VG. Theoretical model of intravascular paramagnetic tracers effect on tissue relaxation. *Magn Reson Med*, 56(1):187–197, Jul 2006.

[14] Boxerman JL, Schmainda KM and Weisskoff RM. Relative cerebral blood volume maps corrected for contrast agent extravasation significantly correlate with glioma tumor grade, whereas uncorrected maps do not. *AJNR Am J Neuroradiol*, 27(4):859–867, Apr 2006.

[15] Vonken EP, van Osch MJ, Bakker CJ and Viergever MA. Simultaneous quantitative cerebral perfusion and Gd-DTPA extravasation measurement with dual-echo dynamic susceptibility contrast MRI. *Magn Reson Med*, 43(6):820–827, Jun 2000.

[16] Haselhorst R, Kappos L, Bilecen D, Scheffler K, Möri D, Radü EW and Seelig J. Dynamic susceptibility contrast MR imaging of plaque development in multiple sclerosis: application of an extended blood-brain barrier leakage correction. *J Magn Reson Imaging*, 11(5):495–505, May 2000.

[17] Quarles CC, Ward BD and Schmainda KM. Improving the reliability of obtaining tumor hemodynamic parameters in the presence of contrast agent extravasation. *Magn Reson Med*, 53(6):1307–1316, Jun 2005.

[18] Knutsson L, Ståhlberg F and Wirestam R. Absolute quantification of perfusion using dynamic susceptibility contrast MRI: pitfalls and possibilities. *MAGMA*, 23(1):1–21, Feb 2010.

[19] Gray H. *Anatomy of the human body*. Philadelphia: Lea & Febiger, 20th edition, 1918.

[20] Schmidt R and Lang F. *Physiologie des Menschen: Mit Pathophysiologie*. Springer-Lehrbuch. Springer, 2007. ISBN 9783540329084.

[21] Compston A and Coles A. Multiple sclerosis. *Lancet*, 372(9648):1502–1517, Oct 2008.

[22] McDonald WI, Compston A, Edan G, Goodkin D, Hartung HP, Lublin FD, McFarland HF, Paty DW, Polman CH, Reingold SC, Sandberg-Wollheim M, Sibley W, Thompson A, van den Noort S, Weinshenker BY and Wolinsky JS. Recommended diagnostic criteria for multiple sclerosis: guidelines from the International Panel on the diagnosis of multiple sclerosis. *Ann Neurol*, 50(1):121–127, Jul 2001.

[23] Polman CH, Reingold SC, Edan G, Filippi M, Hartung HP, Kappos L, Lublin FD, Metz LM, McFarland HF, O'Connor PW, Sandberg-Wollheim M, Thompson AJ, Weinshenker BG and Wolinsky JS. Diagnostic criteria for multiple sclerosis: 2005 revisions to the "McDonald Criteria". *Ann Neurol*, 58(6):840–846, Dec 2005.

[24] Filippi M and Rocca MA. MR imaging of multiple sclerosis. *Radiology*, 259(3):659–681, Jun 2011.

[25] Ge Y. Multiple sclerosis: the role of MR imaging. *AJNR Am J Neuroradiol*, 27(6):1165–1176, 2006.

[26] Bakshi R, Neema M, Healy BC, Liptak Z, Betensky RA, Buckle GJ, Gauthier SA, Stankiewicz J, Meier D, Egorova S, Arora A, Guss ZD, Glanz B, Khoury SJ, Guttmann CRG and Weiner HL. Predicting clinical progression in multiple sclerosis with the magnetic resonance disease severity scale. *Arch Neurol*, 65(11):1449–1453, Nov 2008.

[27] Carmeliet P and Jain RK. Molecular mechanisms and clinical applications of angiogenesis. *Nature*, 473(7347):298–307, May 2011.

[28] Munn LL. Aberrant vascular architecture in tumors and its importance in drug-based therapies. *Drug Discov Today*, 8(9):396–403, May 2003.

[29] Haacke E. *Magnetic resonance imaging: physical principles and sequence design*. J. Wiley & Sons, 1999. ISBN 9780471351283.

[30] Levitt MH. *Spin Dynamics: Basics of Nuclear Magnetic Resonance*. John Wiley & Sons Ltd, 2nd edition, 2008.

[31] Hanson LG. Is quantum mechanics necessary for understanding magnetic resonance? *Concepts in Magnetic Resonance Part A*, 32A(5):329–340, 2008. ISSN 1552-5023.

[32] Kiselev VG, Strecker R, Ziyeh S, Speck O and Hennig J. Vessel size imaging in humans. *Magn Reson Med*, 53(3):553–563, Mar 2005.

[33] Sourbron SP, Michaely HJ, Reiser MF and Schoenberg SO. MRI-measurement of perfusion and glomerular filtration in the human kidney with a separable compartment model. *Invest Radiol*, 43(1):40–48, Jan 2008.

[34] Brix G, Kiessling F, Lucht R, Darai S, Wasser K, Delorme S and Griebel J. Microcirculation and microvasculature in breast tumors: pharmacokinetic analysis of dynamic MR image series. *Magn Reson Med*, 52(2):420–429, Aug 2004.

[35] Notohamiprodjo M, Sourbron S, Staehler M, Michaely HJ, Attenberger UI, Schmidt GP, Boehm H, Horng A, Glaser C, Stief C, Reiser MF and Herrmann KA. Measuring perfusion and permeability in renal cell carcinoma with dynamic contrast-enhanced MRI: a pilot study. *J Magn Reson Imaging*, 31(2):490–501, Feb 2010.

[36] Ito H, Kanno I, Kato C, Sasaki T, Ishii K, Ouchi Y, Iida A, Okazawa H, Hayashida K, Tsuyuguchi N et al. Database of normal human cerebral blood flow, cerebral blood volume, cerebral oxygen extraction fraction and cerebral metabolic rate of oxygen measured by positron emission tomography with 15 O-labelled carbon dioxide or water, carbon monoxide and oxygen: a multicentre study in Japan. *European Journal of Nuclear Medicine and Molecular Imaging*, 31(5):635–643, 2004. ISSN 1619-7070.

[37] Covarrubias DJ, Rosen BR and Lev MH. Dynamic magnetic resonance perfusion imaging of brain tumors. *Oncologist*, 9(5):528–537, 2004.

[38] Østergaard L. Principles of cerebral perfusion imaging by bolus tracking. *J Magn Reson Imaging*, 22(6):710–717, Dec 2005.

[39] Law M, Cha S, Knopp E, Johnson G, Arnett J and Litt A. High-Grade Gliomas and Solitary Metastases: Differentiation by Using Perfusion and Proton Spectroscopic MR Imaging1. *Radiology*, 222(3):715, 2002. ISSN 0033-8419.

[40] Sawlani RN, Raizer J, Horowitz SW, Shin W, Grimm SA, Chandler JP, Levy R, Getch C and Carroll TJ. Glioblastoma: a method for predicting response to antiangiogenic

chemotherapy by using MR perfusion imaging–pilot study. *Radiology*, 255(2):622–628, May 2010.

[41] Ge Y, Law M, Johnson G, Herbert J, Babb JS, Mannon LJ and Grossman RI. Dynamic susceptibility contrast perfusion MR imaging of multiple sclerosis lesions: characterizing hemodynamic impairment and inflammatory activity. *AJNR Am J Neuroradiol*, 26(6):1539–1547, 2005.

[42] Pintaske J, Martirosian P, Graf H, Erb G, Lodemann KP, Claussen CD and Schick F. Relaxivity of Gadopentetate Dimeglumine (Magnevist), Gadobutrol (Gadovist), and Gadobenate Dimeglumine (MultiHance) in human blood plasma at 0.2, 1.5, and 3 Tesla. *Invest Radiol*, 41(3):213–221, Mar 2006.

[43] Sourbron S. Technical aspects of MR perfusion. *Eur J Radiol*, 76(3):304–313, Dec 2010.

[44] Heilmann M, Walczak C, Vautier J, Dimicoli JL, Thomas CD, Lupu M, Mispelter J and Volk A. Simultaneous dynamic T1 and T2* measurement for AIF assessment combined with DCE MRI in a mouse tumor model. *MAGMA*, 20(4):193–203, Oct 2007.

[45] Sourbron S, Heilmann M, Biffar A, Walczak C, Vautier J, Volk A and Peller M. Bolus-tracking MRI with a simultaneous T1- and T2*-measurement. *Magn Reson Med*, 62(3):672–681, Sep 2009.

[46] Sourbron S. Technical aspects of MR perfusion. *Eur J Radiol*, Apr 2010.

[47] Larsson HBW, Hansen AE, Berg HK, Rostrup E and Haraldseth O. Dynamic contrast-enhanced quantitative perfusion measurement of the brain using T1-weighted MRI at 3T. *J Magn Reson Imaging*, 27(4):754–762, Apr 2008.

[48] Larsson HBW, Courivaud F, Rostrup E and Hansen AE. Measurement of brain perfusion, blood volume, and blood-brain barrier permeability, using dynamic contrast-enhanced T(1)-weighted MRI at 3 tesla. *Magn Reson Med*, 62(5):1270–1281, Nov 2009.

[49] Sourbron S, Ingrisch M, Siefert A, Reiser M and Herrmann K. Quantification of cerebral blood flow, cerebral blood volume, and blood-brain-barrier leakage with DCE-MRI. *Magn Reson Med*, 62(1):205–217, Jul 2009.

[50] Roberts HC, Roberts TP, Brasch RC and Dillon WP. Quantitative measurement of microvascular permeability in

human brain tumors achieved using dynamic contrast-enhanced MR imaging: correlation with histologic grade. *AJNR Am J Neuroradiol*, 21(5):891–899, May 2000.

[51] Haroon HA, Buckley DL, Patankar TA, Dow GR, Rutherford SA, Balériaux D and Jackson A. A comparison of Ktrans measurements obtained with conventional and first pass pharmacokinetic models in human gliomas. *J Magn Reson Imaging*, 19(5):527–536, May 2004.

[52] Singh A, Haris M, Rathore D, Purwar A, Sarma M, Bayu G, Husain N, Rathore RKS and Gupta RK. Quantification of physiological and hemodynamic indices using T(1) dynamic contrast-enhanced MRI in intracranial mass lesions. *J Magn Reson Imaging*, 26(4):871–880, Oct 2007.

[53] Pruessmann KP, Weiger M, Scheidegger MB and Boesiger P. SENSE: sensitivity encoding for fast MRI. *Magn Reson Med*, 42(5):952–962, Nov 1999.

[54] Griswold MA, Jakob PM, Heidemann RM, Nittka M, Jellus V, Wang J, Kiefer B and Haase A. Generalized autocalibrating partially parallel acquisitions (GRAPPA). *Magn Reson Med*, 47(6):1202–1210, Jun 2002.

[55] Fink C, Ley S, Kroeker R, Requardt M, Kauczor HU and Bock M. Time-resolved contrast-enhanced three-dimensional magnetic resonance angiography of the chest: combination of parallel imaging with view sharing (TREAT). *Invest Radiol*, 40(1):40–48, Jan 2005.

[56] Song T, Laine AF, Chen Q, Rusinek H, Bokacheva L, Lim RP, Laub G, Kroeker R and Lee VS. Optimal k-space sampling for dynamic contrast-enhanced MRI with an application to MR renography. *Magn Reson Med*, 61(5):1242–1248, May 2009.

[57] Larkman DJ and Nunes RG. Parallel magnetic resonance imaging. *Phys Med Biol*, 52(7):R15–R55, Apr 2007.

[58] Schoenberg S, Dietrich O and Reiser M. *Parallel Imaging in Clinical MR Applications*. Springer-Verlag Berlin Heidelberg, 2007.

[59] Korosec FR, Frayne R, Grist TM and Mistretta CA. Time-resolved contrast-enhanced 3D MR angiography. *Magn Reson Med*, 36(3):345–351, Sep 1996.

[60] Risse F, Semmler W, Kauczor HU and Fink C. Dual-bolus approach to quantitative measurement of pulmonary perfusion by contrast-enhanced MRI. *J Magn Reson Imaging*, 24(6):1284–1290, Dec 2006.

[61] Roberts C, Buckley DL and Parker GJM. Comparison of errors associated with single- and multi-bolus injection protocols in low-temporal-resolution dynamic contrast-enhanced tracer kinetic analysis. *Magn Reson Med*, 56(3):611–619, Sep 2006.

[62] Wang J, Qiu M, Kim H and Constable RT. T1 measurements incorporating flip angle calibration and correction in vivo. *J Magn Reson*, 182(2):283–292, Oct 2006.

[63] Deoni SCL, Peters TM and Rutt BK. High-resolution T1 and T2 mapping of the brain in a clinically acceptable time with DESPOT1 and DESPOT2. *Magn Reson Med*, 53(1):237–241, Jan 2005.

[64] Deoni SCL, Rutt BK and Peters TM. Rapid combined T1 and T2 mapping using gradient recalled acquisition in the steady state. *Magn Reson Med*, 49(3):515–526, Mar 2003.

[65] Donaldson SB, West CML, Davidson SE, Carrington BM, Hutchison G, Jones AP, Sourbron SP and Buckley DL. A comparison of tracer kinetic models for T1-weighted dynamic contrast-enhanced MRI: application in carcinoma of the cervix. *Magn Reson Med*, 63(3):691–700, Mar 2010.

[66] Yarnykh VL. Optimal radiofrequency and gradient spoiling for improved accuracy of T1 and B1 measurements using fast steady-state techniques. *Magn Reson Med*, 63(6):1610–1626, Jun 2010.

[67] Yarnykh VL. Actual flip-angle imaging in the pulsed steady state: a method for rapid three-dimensional mapping of the transmitted radiofrequency field. *Magn Reson Med*, 57(1):192–200, Jan 2007.

[68] Jacquez JA. *Compartmental Analysis in Biology and Medicine*. University of Michigan Press, 1985.

[69] Ostergaard L, Sorensen AG, Kwong KK, Weisskoff RM, Gyldensted C and Rosen BR. High resolution measurement of cerebral blood flow using intravascular tracer bolus passages. Part II: Experimental comparison and preliminary results. *Magn Reson Med*, 36(5):726–736, Nov 1996.

[70] Ostergaard L, Weisskoff RM, Chesler DA, Gyldensted C and Rosen BR. High resolution measurement of cerebral blood flow using intravascular tracer bolus passages. Part I: Mathematical approach and statistical analysis. *Magn Reson Med*, 36(5):715–725, Nov 1996.

[71] Sourbron S, Luypaert R, Schuerbeek PV, Dujardin M and Stadnik T. Choice of the regularization parameter for perfusion quantification with MRI. *Phys Med Biol*, 49(14):3307–3324, Jul 2004.

[72] Sourbron S, Luypaert R, Schuerbeek PV, Dujardin M, Stadnik T and Osteaux M. Deconvolution of dynamic contrast-enhanced MRI data by linear inversion: choice of the regularization parameter. *Magn Reson Med*, 52(1):209–213, Jul 2004.

[73] Sourbron S, Dujardin M, Makkat S and Luypaert R. Pixel-by-pixel deconvolution of bolus-tracking data: optimization and implementation. *Phys Med Biol*, 52(2):429–447, Jan 2007.

[74] de Bazelaire C, Siauve N, Fournier L, Frouin F, Robert P, Clement O, de Kerviler E and Cuenod CA. Comprehensive model for simultaneous MRI determination of perfusion and permeability using a blood-pool agent in rats rhabdomyosarcoma. *Eur Radiol*, 15(12):2497–2505, Dec 2005.

[75] Brix G, Griebel J, Kiessling F and Wenz F. Tracer kinetic modelling of tumour angiogenesis based on dynamic contrast-enhanced CT and MRI measurements. *Eur J Nucl Med Mol Imaging*, 37 Suppl 1:S30–S51, Aug 2010.

[76] Tofts PS, Brix G, Buckley DL, Evelhoch JL, Henderson E, Knopp MV, Larsson HB, Lee TY, Mayr NA, Parker GJ, Port RE, Taylor J and Weisskoff RM. Estimating kinetic parameters from dynamic contrast-enhanced T(1)-weighted MRI of a diffusable tracer: standardized quantities and symbols. *J Magn Reson Imaging*, 10(3):223–232, Sep 1999.

[77] Tofts PS. Modeling tracer kinetics in dynamic Gd-DTPA MR imaging. *J Magn Reson Imaging*, 7(1):91–101, 1997.

[78] Buckley DL. Uncertainty in the analysis of tracer kinetics using dynamic contrast-enhanced T1-weighted MRI. *Magn Reson Med*, 47(3):601–606, Mar 2002.

[79] Luypaert R, Sourbron S and de Mey J. Validity of perfusion parameters obtained using the modified Tofts model: A simulation study. *Magn Reson Med*, Dec 2010.

[80] Ingrisch M, Sourbron S, Reiser MF and Peller M. Model Selection in Dynamic Contrast Enhanced MRI: The Akaike Information Criterion. In R Magjarevic, O Dössel and WC Schlegel, editors, *World Congress on Medical Physics and Biomedical Engineering*, volume 25/4 of *IFMBE Proceedings*, pp. 356–358. Springer Berlin Heidelberg, 2010. ISBN 978-3-642-03882-2.

[81] Sourbron SP and Buckley DL. On the scope and interpretation of the Tofts models for DCE-MRI. *Magn Reson Med*, Mar 2011.

[82] Burnham KP and Anderson DR. *Model selection and multimodel inference: a practical information-theoretic approach*. Springer, 2002.

[83] Akaike H. Information theory and an extension of the maximum likelihood principle. In BN Petrov and F Csaki, editors, *Second International Symposium on Information Theory*, pp. 267–281. Springer-Verlag, 1973.

[84] Glatting G, Kletting P, Reske SN, Hohl K and Ring C. Choosing the optimal fit function: comparison of the Akaike information criterion and the F-test. *Med Phys*, 34(11):4285–4292, Nov 2007.

[85] Brix G, Zwick S, Kiessling F and Griebel J. Pharmacokinetic analysis of tissue microcirculation using nested models: multimodel inference and parameter identifiability. *Med Phys*, 36(7):2923–2933, Jul 2009.

[86] Ahearn TS, Staff RT, Redpath TW and Semple SIK. The use of the Levenberg-Marquardt curve-fitting algorithm in pharmacokinetic modelling of DCE-MRI data. *Phys Med Biol*, 50(9):N85–N92, May 2005.

[87] Markwardt CB. Non-linear Least-squares Fitting in IDL with MPFIT. In D A Bohlender, D Durand, & P Dowler, editor, *Astronomical Society of the Pacific Conference Series*, volume 411 of *Astronomical Society of the Pacific Conference Series*, pp. 251–+. September 2009.

[88] Sourbron S, Biffar A, Ingrisch M, Fierens Y and Luypaert R. PMI0.4: platform for research in medical imaging. In *Proceedings of the ESMRMB*. Antalya, 2009.

[89] Lassen N and Perl W. *Tracer kinetic methods in medical physiology*. Raven Press, 1979. ISBN 9780890041147.

[90] Gillard J, Waldman A and Barker P. *Clinical MR neuroimaging: diffusion, perfusion, and spectroscopy*. Cambridge University Press, 2nd edition, 2010. ISBN 9780521824576.

[91] Stanisz GJ, Odrobina EE, Pun J, Escaravage M, Graham SJ, Bronskill MJ and Henkelman RM. T1, T2 relaxation and magnetization transfer in tissue at 3T. *Magn Reson Med*, 54(3):507–512, Sep 2005.

[92] Ethofer T, Mader I, Seeger U, Helms G, Erb M, Grodd W, Ludolph A and Klose U. Comparison of longitudinal metabolite relaxation times in different regions of the human brain at 1.5 and 3 Tesla. *Magn Reson Med*, 50(6):1296–1301, Dec 2003.

[93] Law I, Iida H, Holm S, Nour S, Rostrup E, Svarer C and Paulson O. Quantitation of Regional Cerebral Blood Flow Corrected for Partial Volume Effect Using O-15 Water and PET: II. Normal Values and Gray Matter Blood Flow Response to Visual Activation. *Journal of Cerebral Blood Flow & Metabolism*, 20(8):1252–1263, 2000. ISSN 0271-678X.

[94] Bassingthwaighte JB. Microcirculatory considerations in NMR flow imaging. *Magn Reson Med*, 14(2):172–178, May 1990.

[95] Neema M, Stankiewicz J, Arora A, Guss ZD and Bakshi R. MRI in multiple sclerosis: what's inside the toolbox? *Neurotherapeutics*, 4(4):602–617, Oct 2007.

[96] Filippi M, Yousry T, Campi A, Kandziora C, Colombo B, Voltz R, Martinelli V, Spuler S, Bressi S, Scotti G and Comi G. Comparison of triple dose versus standard dose gadolinium-DTPA for detection of MRI enhancing lesions in patients with MS. *Neurology*, 46(2):379–384, Feb 1996.

[97] Silver NC, Good CD, Barker GJ, MacManus DG, Thompson AJ, Moseley IF, McDonald WI and Miller DH. Sensitivity of contrast enhanced MRI in multiple sclerosis. Effects of gadolinium dose, magnetization transfer contrast and delayed imaging. *Brain*, 120 (Pt 7):1149–1161, Jul 1997.

[98] Wuerfel J, Bellmann-Strobl J, Brunecker P, Aktas O, McFarland H, Villringer A and Zipp F. Changes in cerebral perfusion precede plaque formation in multiple sclerosis: a longitudinal perfusion MRI study. *Brain*, 127(Pt 1):111–119, Jan 2004.

[99] Inglese M, Adhya S, Johnson G, Babb JS, Miles L, Jaggi H, Herbert J and Grossman RI. Perfusion magnetic resonance imaging correlates of neuropsychological impairment in multiple sclerosis. *J Cereb Blood Flow Metab*, 28(1):164–171, Jan 2008.

[100] Adhya S, Johnson G, Herbert J, Jaggi H, Babb JS, Grossman RI and Inglese M. Pattern of hemodynamic impairment in multiple sclerosis: dynamic susceptibility contrast perfusion MR imaging at 3.0 T. *Neuroimage*, 33(4):1029–1035, Dec 2006.

[101] Saindane AM, Law M, Ge Y, Johnson G, Babb JS and Grossman RI. Correlation of diffusion tensor and dynamic perfusion MR imaging metrics in normal-appearing corpus callosum: support for primary hypoperfusion in multiple sclerosis. *Am J Neuroradiol*, 28(4):767–772, Apr 2007.

[102] Law M, Saindane AM, Ge Y, Babb JS, Johnson G, Mannon LJ, Herbert J and Grossman RI. Microvascular abnormality in relapsing-remitting multiple sclerosis: perfusion MR imaging findings in normal-appearing white matter. *Radiology*, 231(3):645–652, Jun 2004.

[103] Keyser JD, Steen C, Mostert JP and Koch MW. Hypoperfusion of the cerebral white matter in multiple sclerosis: possible mechanisms and pathophysiological significance. *J Cereb Blood Flow Metab*, 28(10):1645–1651, Oct 2008.

[104] Ingrisch M, Sourbron S, Morhard D, Ertl-Wagner B, Kümpfel T, Hohlfeld R, Reiser M and Glaser C. Quantification of Perfusion and Permeability in Multiple Sclerosis: Dynamic Contrast-Enhanced MRI in 3D at 3T. *Invest Radiol*, accepted for publication.

ACKNOWLEDGEMENTS

An dieser Stelle möchte ich mich bei all jenen, zum Gelingen dieser Arbeit beigetragen haben, herzlich bedanken.

Mein Dank gilt Prof. Dr. Dr. Maximilian Reiser für die freundliche Aufnahme im Institut für Klinische Radiologie und die Möglichkeit, hier zu promovieren. Die anregende Atmosphäre und die interdisziplinäre Zusammenarbeit von Physikern und Medizinern haben ganz wesentlich zum Gelingen dieser Arbeit beigetragen.

Besonders bedanken möchte ich mich bei PD Dr. Olaf Dietrich, der diese Arbeit mit viel Geduld betreut hat; von seinem umfassenden Fachwissen nicht nur über MR-Physik habe ich sehr profitiert. Auch darüber hinaus hatte er für alle meine Fragen nicht nur ein offenes Ohr, sondern meistens auch die die richtige Antwort –[1] die schnellste Lösung für ein beliebiges Linux- oder LaTeX-Problem ist im Allgemeinen ein kurzer Besuch bei Olaf .

Diese Arbeit wäre nicht möglich gewesen ohne Dr. Steven Sourbron: Er hat (nicht nur) mich davon überzeugt, dass es sich lohnt, sich mit dem Thema Perfusionsbildgebung und -quantifizierung zu beschäftigen; ein großer Teil meiner Kenntnisse auf diesem Gebiet stammt von ihm. Nicht zuletzt verdanken wir ihm die Software, die die Entstehung einer ganze Reihe von Ideen, Studien und Publikationen katalysiert hat. Für all das und noch einiges mehr: meinen herzlichen Dank, Steven!

Bedanken möchte ich mich auch bei meinem langjährigen Büronachbarn Dr. Michael Peller für all die Fachgespräche über Bildgebung (auch die nichtmedizinische), und dafür, dass ich mich immer auf ihn verlassen konnte, sowie bei allen aktuellen und ehemaligen Mitgliedern unserer Physikgruppe für das gute Arbeitsklima und den Spaß neben und bei der Arbeit: bei meinen ehemaligen Kollegen José und Andi, bei den Freunden des Postillons Linus und Felix und bei Lukas, Max und Moritz.

Stellvertretend für all die Mediziner, mit denen ich in den letzten Jahren eng und erfolgreich zusammengearbeitet habe, möchte ich mich hier ganz herzlich bei Prof. Dr. Birgit Ertl-Wagner bedanken – für die gute und vertrauensvolle Zusammenarbeit, für ihre Unterstützung bei dem MS-Projekt, für die geduldige Erweiterung meines medizinischen Fachwissens und für die stets lehrreichen Arbeitsgruppentreffen und die Bewirtung bei denselben[2].

1 ja, richtig: nicht „-“, sondern „–“

2 und, außerhalb unserer fachlichen Zusammenarbeit, beispielsweise für die viele Babykleidung